POWER STABILIZATION OF DIODE PUMPED SOLID STATE LASERS BY MEANS OF ADAPTIVE CONTROL OF DRIVE CURRENT

A THESIS SUBMITTED TO
THE GRADUATE SCHOOL OF NATURAL AND APPLIED SCIENCES
OF
MIDDLE EAST TECHNICAL UNIVERSITY

BY

TAYFUN ŞENTÜRK

IN PARTIAL FULFILLMENT OF THE REQUIREMENTS
FOR
THE DEGREE OF MASTER OF SCIENCE
IN
ELECTRICAL AND ELECTRONICS ENGINEERING

JULY 2019

Approval of the thesis:

POWER STABILIZATION OF DIODE PUMPED SOLID STATE LASERS BY MEANS OF ADAPTIVE CONTROL OF DRIVE CURRENT

submitted by **TAYFUN ŞENTÜRK** in partial fulfillment of the requirements for the degree of **Master of Science in Electrical and Electronics Engineering Department, Middle East Technical University** by,

Prof. Dr. Halil Kalıpçılar _____
Dean, Graduate School of **Natural and Applied Sciences**

Prof. Dr. İlkay Ulusoy _____
Head of Department, **Electrical and Electronics Engineering**

Prof. Dr. Kemal Leblebicioğlu _____
Supervisor, **Electrical and Electronics Eng. Dept., METU**

Dr. Kuthan Yelen _____
Co-supervisor, **ASELSAN, Inc.**

Examining Committee Members:

Prof. Dr. Gönül Turhan Sayan
Electrical and Electronics Engineering Department, METU _____

Prof. Dr. Kemal Leblebicioğlu
Electrical and Electronics Engineering Department, METU _____

Prof. Dr. Klaus Werner Schmidt
Electrical and Electronics Engineering Department, METU _____

Assist. Prof. Dr. Serdar Kocaman
Electrical and Electronics Engineering Department, METU _____

Assist. Prof. Dr. Yakup Özkazanç
Electrical and Electronics Eng. Dept., Hacettepe University _____

Date: **31/07/2019**

I hereby declare that all information in this document has been obtained and presented in accordance with academic rules and ethical conduct. I also declare that, as required by these rules and conduct, I have fully cited and referenced all material and results that are not original to this work.

Name, Last Name: Tayfun Şentürk

Signature :

ABSTRACT

POWER STABILIZATION OF DIODE PUMPED SOLID STATE LASERS BY MEANS OF ADAPTIVE CONTROL OF DRIVE CURRENT

Şentürk, Tayfun
M.S., Department of Electrical and Electronics Engineering
Supervisor : Prof. Dr. Kemal Leblebicioğlu
Co-Supervisor : Dr. Kuthan Yelen

July 2019, 109 pages

Lasers provide precision and sensitivity for various applications. However, some fundamental properties make lasers very susceptible to external changes. When stability of laser parameters is required the traditional approach is to stabilize the working environment, such as strict temperature and climate control, mechanical isolation as well as damping of any vibration. This traditional approach is very difficult to implement in harsh industrial environments and almost impossible for many military applications.

One frequently used state-of-the-art laser type in industrial and military applications is diode pumped solid state lasers. Fundamentally, temperature of various components, small deviations in optical properties and opto-mechanical alignments over time as well as aging cause output power of such lasers to drift away from the desired level. Tracking of all these critical stimuli is impractical and even when achieved, it

would result in a complex multi-input control algorithm design.

To overcome this difficulty, firstly, a reliable internal laser output energy measurement system is designed, implemented and tested under various operating conditions. The output from this sensor provides the feedback signal for the control algorithm.

A closed-loop control system is expected to be designed and optimized for regulation of output energy of a SISO type laser device by setting the drive current adaptive to the environmental conditions.

The algorithm and implemented system is experimentally tested.

Keywords: Q-Switched Diode Pumped Solid State Laser Modeling, Laser Output Energy Stabilization, Laser Energy Meter

ÖZ

DİYOT POMPALI KATI HAL LAZERLERİNİN SÜRÜCÜ AKIMININ UYARLANIR KONTROLÜ İLE GÜÇ DENGELİLEŞTİRMESİ

Şentürk, Tayfun
Yüksek Lisans, Elektrik ve Elektronik Mühendisliği Bölümü
Tez Yöneticisi : Prof. Dr. Kemal Leblebicioğlu
Ortak Tez Yöneticisi : Dr. Kuthan Yelen

Temmuz 2019 , 109 sayfa

Lazerler, bir çok uygulamaya hassasiyet ve kesinlik sağlar. Fakat lazerlerin bazı temel özellikleri, onları dış etkilere duyarlı kılar. Lazerlerin parametrelerinin kararlılığı gerektiğinde, geleneksel yaklaşım olarak, sıcaklığın ve iklimin kontrol edilmesi, mekanik izolasyon ve aynı zamanda titreşimlerin bastırılması gibi önlemler alınarak lazerlerin çalışma ortamı kararlı hale getirilir. Bu geleneksel yaklaşımı zorlu endüstriyel ortamlarda ve özellikle askeri uygulamada gerçeklemek zor, hatta imkansızdır.

Endüstriyel ve askeri uygulamalarda sıklıkla kullanılan, gelişmiş lazer türlerinden biri de diyot pompalı katı hal lazerleridir. Çeşitli bileşenlerin sıcaklığı, optik malzemelerin özelliklerindeki küçük değişmeler, opto-mekanik hizalama ve yaşlanma bu tip lazerlerin çıkış güçlerinin planlanan seviyeden uzaklaşmasına sebep olan temel etmenlerdir. Bu kritik etmenlerin takibi uygulanabilir değildir; takip edildiğinde bile, karmaşık ve çok girdili kontrol algoritması tasarımı gerektirir.

Bu zorluğu aşmak için, öncelikle, güvenilir bir dahili lazer çıkış gücü ölçme sistemi tasarlanmış, üretilmiş ve çeşitli çalışma koşullarında test edilmiştir. Bu sensörün çıkışı, kontrol algoritmasına girdi sağlayacaktır. Sonrasında, sistem modellemesi, kapalı döngü kontrol sistemi tasarımı, simulasyonu, gerçeklemesi ve testleri yapılmıştır.

Anahtar Kelimeler: Q-Anahtarlı Diyot Pompalı Katı Hal Lazerlerinin Modellenmesi, Lazer Çıkış Enerjisi Stabilizasyonu, Lazer Enerji Metre

To my family

ACKNOWLEDGMENTS

I owe my deepest gratitude to my supervisor, Prof. Kemal Leblebicioğlu, for the patient guidance, encouragement and advice he has provided throughout this thesis. I appreciate his boundless help for making this work possible.

I am deeply grateful to my co-supervisor, Dr. Kuthan Yelen, for his guidance and endless assistance not only for this dissertation but also for my entire career. He always encouraged me wisely to advance towards challenging engineering problems. This thesis would not have been possible without him.

I am indebted to my colleagues Burçin Dağıstan and Onur Arslan for their effort on the design of the measurement system.

I would like to thank to my senior colleagues, especially to Hakan Atbaş and Peren Korkut for their ideas, help and contributions.

I would like particularly to acknowledge the invaluable contribution of my manager Atakan DURA.

I would like to extend my thanks to my family and friends, for their patience and support throughout this study.

Finally, I am very thankful to ASELSAN Inc. MGEO Division for providing the experimental setups, computational facilities and funding.

TABLE OF CONTENTS

LIST OF TABLES

TABLES

LIST OF FIGURES

FIGURES

LIST OF ABBREVIATIONS

YAG	Yttrium Aluminum Garnet
FPGA	Field Programmable Gate Array
CW	Continuous Wave
LIDAR	Light Detection and Ranging
PRF	Pulse Repetition Frequency
nm	Nanometer
UAV	Unmanned Aerial Vehicle
EO	Electro-Optics
LDA	Laser Diode Array
CTE	Coefficient of Thermal Expansion
FWHM	Full Width Half Max
LDDM	Laser Diode Driver Module
OD	Optical Density
QCW	Quasi-Continuous Wave
ESS	Environmental Stress Screening
ASE	Amplified Spontaneous Emission
MCU	Micro-Controller Unit
ADC	Analog to Digital Converter
OD	Optical Density
QS-DPSSL	Q-Switched Diode Pumped Solid State Laser
PID	Proportional-Integral-Derivative Controller
SISO	Single Input Single Output
AR	Auto-Regressive

NOMENCLATURE

Actuator Model

Symbol	Description	Value	Units
μ_i	Center Emission Wavelength of ith LDA	–	nm
C_{s1}	Heat Capacity of LDA Assembly	218.6062	$\mathrm{J/K}$
C_{HS1}	Heat Capacity of Heat Sink of LDA	215.4971	$\mathrm{J/K}$
C_{CASE}	Heat Capacity of 5 X LDA	3.1091	$\mathrm{J/K}$
$R_{conv,1}$	Convective Heat Resistance of LDA Assy.	–	°C/W
R_{HA2}	Heat Resistance of Gain Medium Assy. to Ambient	–	°C/W
R_{HA1}	Heat Resistance of LDA Assy. to Ambient	–	°C/W
$R_{rad,1}$	Radiative Heat Resistance of LDA Assy.	–	°C/W
I	Drive Current	–	A
λ_P	Emission Spectrum of LDA Assembly	–	–
λ_{Pi}	Emission Spectrum of ith LDA	–	–

$m_{HS,1}$	Mass of LDA Heat Sink	236.81	g
m_{LDA}	Mass of single LDA	16.3637	g
P_P	Output Power of LDA Assembly	–	W
P_{Pi}	Output Power of ith LDA	–	W
A_{pump}	Pump Area	–	cm^2
σ_i	Spectral Width of ith LDA	–	nm
$\sigma_{se,i}$	Slope Efficiency of ith LDA	–	$\mathrm{W/A}$
c_{Al}	Specific Heat of Aluminum	0.91	$\mathrm{J/(g\,K)}$
c_{CuW}	Specific Heat of Copper Tungsten	190	$\mathrm{J/(kg\,K)}$
A	Surface Area of Heat Sink of LDA Assy.	330	cm^2
T_d	Temperature of LDA Assembly	–	°C
$I_{th,i}$	Threshold Current of ith LDA	–	A
d_{vert}	Vertical Height of Heat Sink of LDA Assy.	6.7	cm

Plant Model

Symbol	**Description**	**Value**	**Units**
P_{ABS}	Absorbed Power by the Gain Medium	–	W
V_{act}	Active Medium Volume	2.376	cm^3
N_0	Density of Ground Level Ions	1.5256×10^{20}	$1/\mathrm{m}^3$

P_{D2}	Dissipated Power in the Gain Medium	–	W
P_{D1}	Dissipated Power in the LDA Assy.	–	W
$\sigma_{ab,eff}$	Effective Absorption Cross Section	–	m^2
γ	Fractional Thermal Loading Factor	0.4	–
C_{s2}	Total Heat Capacity of the Gain Medium	101.2	J/K
ν_L	Lasing Frequency	2.81×10^{14}	Hz
l	Length of the Gain Medium	–	mm
t	Thickness of the Gain Medium	–	mm
L	Length of the Resonator	–	cm
ϕ	Photon Density	–	$1/\mathrm{m}^3$
h	Planck's Constant	6.626176×10^{-34}	$J \cdots$
n	Population Inversion Density	–	$1/\mathrm{m}^3$
ν_P	Pump Frequency	3.7241×10^{14}	Hz
τ_c	Decay Time of the Photons in the Resonator	230×10^{-6}	s
τ_r	Round Trip Time of the Light inside Resonator	–	ns
ϵ	Loss Coefficient of the Resonator	1.1498	–
σ	Stimulated Emission Cross Section	–	m^2

CHAPTER 1

INTRODUCTION

1.1 Historical Development of Lasers

Laser is a major breakthrough of the 20th century. Its development is linked to crucial technologies such as transistors and computers [13]. They had well understood theory; however, realization of the concept had not been obvious. The lasers were developed gradually as transistors and computers.

As a spark, in 1917, Einstein came up with the proposal of stimulated emission. His theory was used and credited by many scientists. Then, C. Townes built the first device based on Einstein's theory. He utilized two energy levels of ammonia for population inversion at microwave region. Maser is an acronym that stands for **M**icrowave **A**mplification by **S**timulated **E**mission of **R**adiation. Later, the idea of stimulated emission of radiation, was developed for optical frequencies. The very first achievement of this idea was realized by T. Maiman in 1960 [11]. He implemented a pump scheme consisting pink ruby crystal as gain medium, helical flash lamp for pumping and the silvered ends of pink ruby crystal for feedback. He also came up with an analogy to maser, which is the abbreviation of **L**ight **A**mplification by **S**timulated **E**mission of **R**adiation. These results lead to the material research activities for amplification of light. Up to now, solids, liquids, gases, plasmas and semiconductors were demonstrated as active medium. In 1964, the most efficient host crystal, which is yttrium aluminum garnet (YAG), for neodymium (Nd) ion was invented. Nd:YAG has outstanding optical, thermal and mechanical properties over other types of solid state lasers. Since then, it is the most commonly used solid state active material.

In 1961, R.W Hellwarth used an optical shutter to accumulate the output from ruby

laser into a single pulse. This optical shutter is opened immediately after the end of pumping. By doing so, a laser pulse with very high peak powers and narrow widths can be attained. This method is called as Q-switching.

The studies about semiconductor lasers followed the above progression. Initially, intrinsic semiconductors were pumped with electron beam to get laser beam. Then, pulsed laser output was obtained from cooled p-n junctions. With technological improvements in the semiconductor design and manufacturing, continuous operation at room conditions was achieved. Now, the semiconductor lasers are packaged in durable, compact as well as cost effective way. They are preferred in stead of flash lamps for pumping solid state lasers.

Range finding by measuring the time of flight of a laser pulse was the first application. Later, this concept became commercial and mostly used by military purposes. Today, lasers are essential for various applications which will be mentioned in Chapter 2. Since its birth in 1960, the literature grows exponentially and lasers represent a 12.9 billion dollars industry in 2018 [14].

1.2 Laser Fundamentals

Lasers are devices generating coherent radiation at frequencies in the infrared, visible or ultraviolet regions of the electromagnetic spectrum [15]. There are continuously operated (CW) lasers as well as pulsed ones. For lasing action, existence of an atom or ion with lasing property, population inversion, and feedback of amplification are necessary. In this section, these requirements and properties of lasers will be explained briefly.

1.2.1 Interaction of Light with Matter

The atoms or ions possessing the lasing property are located at discrete energy levels. At thermal equilibrium, lower energy levels are highly populated than higher ones. These atoms or ions interfere with photons by emitting or absorbing them and changing energy levels depending on their energy states.

The interference between material and electromagnetic wave occurs in three different ways. Firstly, an atom in excited state may emit photon with finite probability and it decays to ground state. This is called as spontaneous emission. Secondly, an atom in excited state may interact with a photon whose energy is close to difference between excited and ground state. It emits a photon having identical properties with incoming photon. This process is known as stimulated emission. Lastly, an atom in ground state may absorb a photon whose energy is close to difference between excited and ground state. This goes by the name of absorption. All three phenomena takes place in the lasing medium (Figure 1.1).

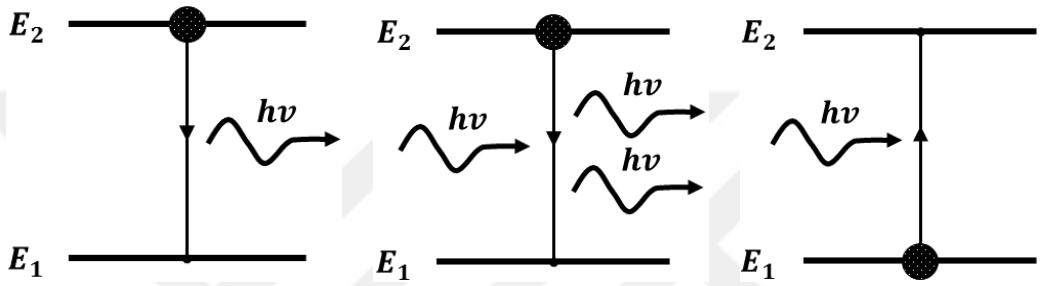

(a) Spontaneous Emission (b) Stimulated Emission (c) Absorption

Figure 1.1: Interaction between Photon and Atom: (a) Spontaneous Emission, (b) Stimulated Emission, (c) Absorption

The above processes have their own properties. Among them, the stimulated emission plays the key role in light amplification. This is because it forms an additional photon with same direction, phase, energy and polarization.

In optically pumped lasers, lasing medium is "pumped" with photons possessing suitable energy for absorption. As these atoms absorb the pump energy they populate in an higher energy level and at some point, the population of upper energy level will be higher than the lower one. This condition is called as population inversion (Figure 1.2).

The population inversion is obligatory for coherent amplification by stimulated emission. The reason is that, if the lower level population is higher than the upper level, probability of absorbing a photon will be more than probability of stimulated emission which destructs accumulation of photons.

The spontaneous emission also takes place in lasing medium. Like in the stimulated

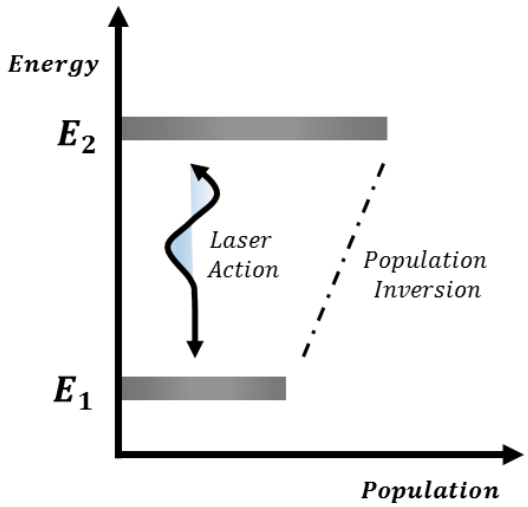

Figure 1.2: Population Inversion

emission case, the probability of spontaneous emission is also increased with pumping. However, resulting photons from spontaneous emission are filtered out by the resonator which is responsible for coherent amplification and filtering of such a photon.

1.2.2 Components of Elementary Laser Device

A basic laser device is consists of:

- Gain Medium (Active Medium),
- Pump Source,
- Resonator.

A block diagram is given in Figure 1.3.

Gain (Active) Medium: It consists of ions which have suitable laser transition property and a host material with high transparency at laser wavelength. Several types are mentioned in Table 1.1.

Pumping: It provides energy for population inversion of active medium. Flash lamps, semiconductor diode lasers and electrical pumping via gas discharge can be given as examples for optically pumped lasers such as Ruby and Nd:YAG. The semiconductor

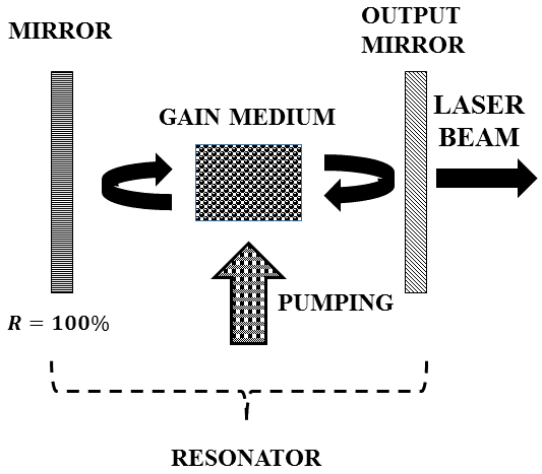

Figure 1.3: Block Diagram of an Elementary Laser Source

Table1.1: A List of Typical Lasers and Corresponding Emission Wavelength

Type	**Laser Material**	**Wavelength (nm)**
Liquid	Dye	300 - 1200
Gas	Carbon Dioxide $[CO_2]$	10600
Gas	Helium Neon $[HeNe]$	632.8
Semiconductor	Gallium Nitride $[GaN]$	360-480
Semiconductor	Indium Gallium Arsenide Phosphide $[InGaAsP]$	1300-1900
Solid State	Ruby	694.3
Solid State	Neodymium Glass $[Nd:Glass]$	1064
Solid State	Neodymium YAG $[Nd:YAG]$	1064, 1319, 532, 266

lasers use directly electrical pumping and the chemical lasers utilize chemical reactions as energy source.

Resonator: It consists of highly and partially reflective mirror that perform the function of a highly selective feedback element by coupling back a portion of the signal emerging from amplifying medium [11].

1.2.3 Properties of Laser Beam

A laser source emits light that has distinctive properties over an ordinary light. These properties are:

- **Monochromaticity:** A laser has specific wavelength while an ordinary light

includes light waves with different wavelengths. We measured the emission spectra of the system under investigation whose active medium is Nd:YAG. The resulting plot is given in Figure 1.4 (a). To emphasize the monochromaticity property of laser, spectrum of sun light is illustrated in Figure 1.4 (b). The solar spectrum starts from 200 nm and lies to 4000 nm approximately. Emission spectrum of the system is very narrow as it is compared to the solar spectrum.

- **Coherence:** Under the favor of stimulated emission, laser waves have the same phase. In contrast, ordinary light waves have different phases.
- **Directional Emissivity:** Laser photons also have the same direction with relatively small divergence in space but ordinary light travels to all directions in space.

1.2.4 Applications

The properties of lasers make them useful for many areas such as:

- **Medical:** Eye Surgery, Dermatology,
- **Material Processing:** Cutting, Welding, Soldering, Marking, Surface Treatment,
- **Scientific Research:** Microscopy, Spectroscopy,
- **Military:** Range Finding, LIDARs, Directed Energy Weapons, Target Designation

Each application takes advantage of different property of lasers. For instance, pulsed lasers can be used for range finding purposes, as well as, high power-continuous wave lasers are useful for material processing.

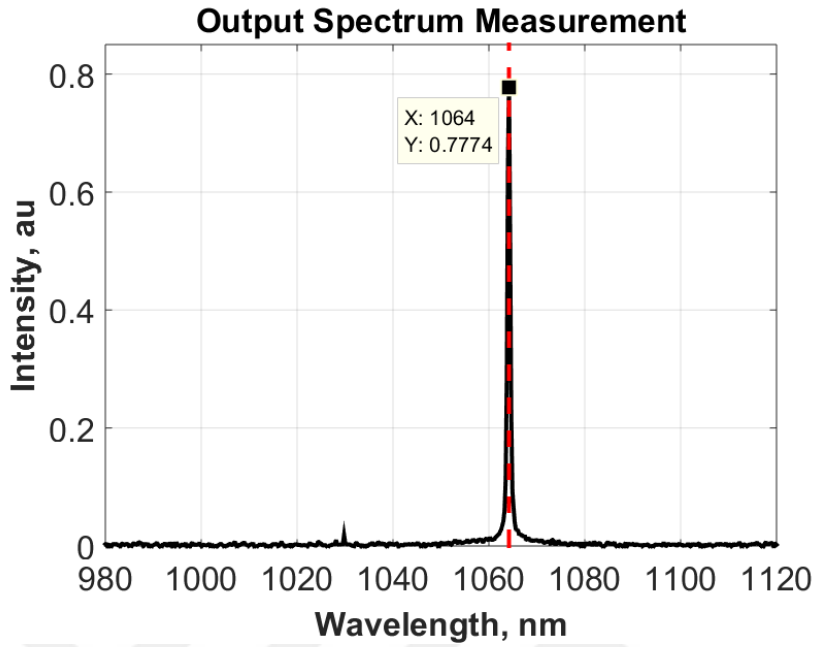

(a) Emission Spectrum of the System, (Measurement Results)

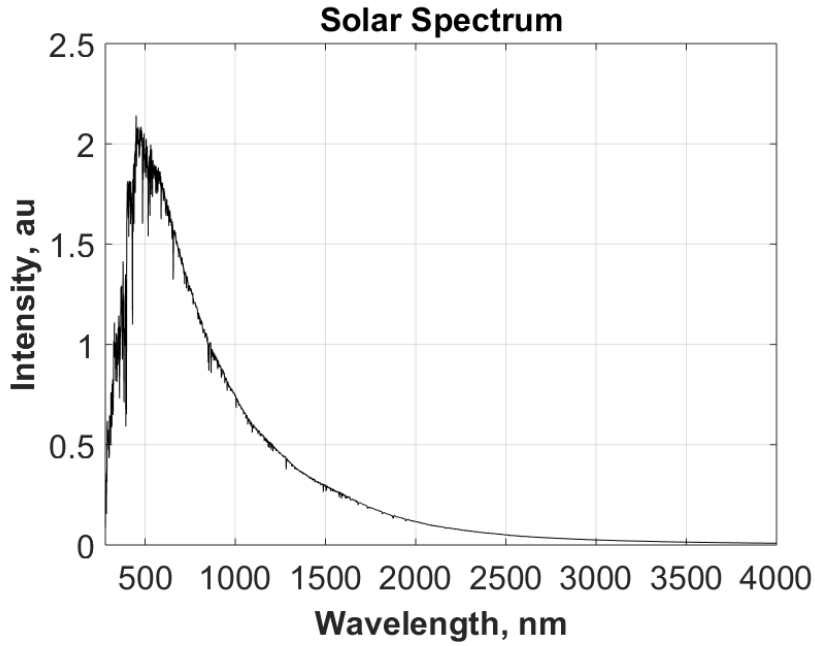

(b) Solar Spectrum, [16]

Figure 1.4: Illustration of Monochromaticity of Lasers: Comparison between Emission Spectrum of the System in this Study and Solar Spectrum

1.3 Motivation and Objective of the Thesis

Laser designers have been accumulating the knowledge since 60s and the application developers challenge complex problems in field utilizing this accumulation. The complexity of these problems is increasing with each passing day because of demanding requirements.

Applications gain several abilities such as increased velocity due to ultra fast nature of light as in communication field or condense energy transfer as in precise material cutting. However, integrating a laser device for an application is not an easy task since the performance parameters of lasers are easily affected by environmental changes such as vibration, humidity and temperature. Generally, designers take precautions for the environmental changes by using climate control, damping of any vibration and mechanical isolation. Implementing these precautions requires cost, size, weight and power.

Unfortunately, some of those preventive measures are impracticable for space and airborne applications. Furthermore, all systems in the industry are getting smaller, lighter and less power demanding. Adding climate control by using heaters and thermoelectric coolers, placing absorbers for different vibration frequencies and mechanical isolation from problematic environment are almost impossible for many applications.

As a result, performance parameters of lasers for a specific application should be monitored and actively controlled to correct harsh ambient effects if efficiency and compactness are mandatory. To achieve this, firstly, designing built-in sensors which collect reliable data of the parameters is required. Then, an algorithm evaluating the sensor data with disturbance (if the disturbance is measurable) and managing the system inputs should be developed, manufactured and verified by experiments simulating these harsh environmental conditions.

One of the most important performance parameter of lasers is output power/energy. For instance, in range finder and target designator applications, the energy should be held in a reasonable level against -20 °C to +50 °C. As a second example, ophthalmic surgery by using lasers demands very stable laser output energy. This is because lasers are utilized for reshaping the cornea or disruption of eye to treat refractive disorders

and cataract. A sudden change in a laser output may cause blindness.

In the present study, output energy of a pulsed diode pumped solid state laser source (Figure 1.5), which is designed for range finding and target designation purposes, is stabilized by manipulating the drive current of diode pump. The output energy deviates from its intended level because of environmental stresses whose impacts on the source will be explained in Chapter 2.

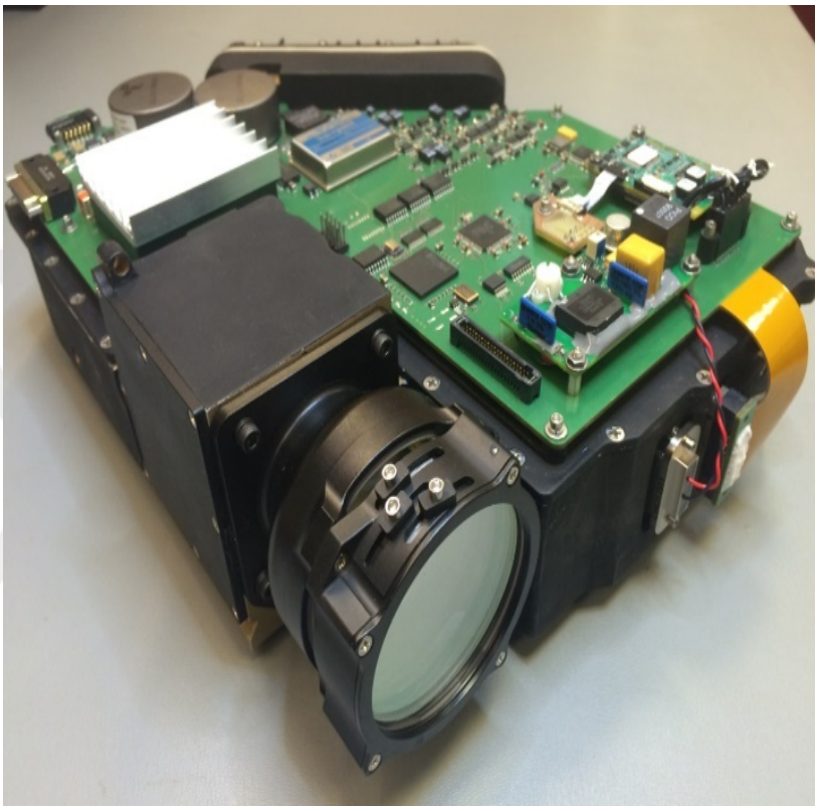

Figure 1.5: Laser Device in the Present Study, Designed for Airborne Applications (UAV, fighter jets)

1.4 Literature Review

There are various studies about stabilization of the laser output power/energy. In [17] continuously diode-pumped, Q-switched laser energy was regulated by measuring fluorescence of the gain medium due to the pumping and then by tuning the drive current of diode pump. In the reference, stabilization of pulse energy was required as pulse repetition frequency changes. The environmental impacts were not considered. A photodiode was used for measurement of fluorescence of the gain medium which

lacks in having proper output samples as the sensor are not placed on the output of laser source and therefore it will not reflect real status of the resonator. In addition, there was used an analog proportional controller like structure for calculating the drive current. In this thesis, measurement system is designed to monitor the output pulse directly as well as environmental stresses are considered and actively suppressed by using compensator.

In [18], a macroscopic rate equation model for simulating dynamical behaviour of continuous wave and pulsed lasers was presented with closed-loop pulse energy controller. This model was extracted from the rate equations and relations were shown in measurable laser parameters. Then, the controller was simulated for pulsed lasers. Then, in [19], this controller was built and tested for fiber-laser-pumped Ho:YLF ring lasers by using FPGA based structure. The laser source in this study has different Q-switching methodology whose cavity loss can not be used as input to the system because laser pulses should be released in a precise timing sequence. Moreover, this study aims suppression of the environmental effects.

In [20], feedback linearization was used to create an algorithm for stabilizing the output energy of an acousto-optic q-switched laser which has different topology. As in [18] and [19], this work also utilized cavity losses introduced by q-switch.

In [21], laser diode pumped solid state Nd:YAG source is stabilized. However, that design used temperature control of pump laser diodes and the laser source is operating continuously. The main goal of this study is stabilization of output power of Q-switched, diode pumped, solid state lasers for a temperature range of -20 °C to + 50 °C without using any temperature control equipment.

As a result, in addition to the given studies in which the output power or energy was stabilized for different types of lasers with various methods, this thesis will be a detailed reference including both design of built-in energy measurement system and output energy controller operating in harsh ambient conditions for diode pumped electro-optical Q-switched solid state lasers.

1.5 Outline of the Present Study

In this study, the output energy of diode pumped solid state laser which changes drastically is measured and actively controlled. The measurement system is designed, manufactured and tested to operate in a temperature range of -20 °C to 50 °C. Then, the overall system is modeled by using physical relations as well as empirical modeling. These models are simulated and their performances are compared to experiments. Lastly, the output energy controller is designed, simulated and experimentally tested for the temperature range of interest.

The steps investigated in this study are as follows:

1. The laser source was manufactured and tested experimentally for the temperature range of interest. The laser source was put inside a climatic cabinet and the output energy was monitored by a calibrated reference energy meter while temperature is altered. The output energy variations were observed.

2. The internal laser energy measurement system was designed. The mid-steps of the energy meter design: Sensors which satisfy operational requirements of the study were analyzed and a suitable sensor was chosen. The processing electronics with software was designed and manufactured. Optical sampling method of the laser pulse was developed. Then the designed and manufactured measurement system was integrated to the laser source and experimentally tested inside the climatic cabinet. The results were compared to a calibrated industrial energy meter.

3. The Q-switched, diode pumped, solid state laser was modeled by using physical relations and system identification:

   Modeling effort by using physical relations started division of the system into parts according to their functionalities. Then, input-output relations of these parts were examined. To model the operation of actuator, experiments which are output power, I-V characteristics and spectrum measurements with respect to temperature were conducted. The laser source were modeled by using rate equations. Parameters were derived and temperature effects on the gain medium

were investigated.

System model was also obtained by using input-output relations. For this purpose, grey box modeling approach was adopted. The basic energy transfer relations from input to output were examined and reduced to its simplest form. Then, for various inputs and operating conditions, experiments were conducted and the output was monitored for parameter investigation. By using Auto-Regressive (AR) time series model, an approach for the parameter investigation for slope efficiency was developed. The results were supported by an experiment and discussed.

4. Noise analysis were conducted for both the laser source and the internal energy measurement system. The distributions of parameters of pumping laser diode arrays were obtained by experimenting 130 laser diode arrays.

   For each stage of measurement system, noise contributors were investigated and calculated. The noise of ADC was experimented. The overall measurement noise budget were derived.

5. For controller design and simulation, all model was constructed in MATLAB/ Simulink environment. Open loop response was compared to the experimental results and its performance was discussed. Proportional-Integral-Derivative (PID) controller in conjunction with feed forward compensator on disturbance were simulated and their parameters were optimized.

6. The closed loop system was also tested by using the climatic test cabinet for the temperature of interest. The results were plotted and discussed.

1.6 Thesis Organization

Chapter2: In this chapter, system in the present study is presented in a detailed manner. Then, statement of the problem and its causes are given.
Chapter3: Mathematical modeling of the laser source based on rate equations and input-output relations are presented.
Chapter4: The internal energy measurement system is described by means of sensor selection, electronic structure and optical sampling strategy.

Chapter5: Noisy components in the whole system are analyzed. Laser diode arrays are put under scope. In addition, sensor and processing electronics are discussed in the sense of noise generation.
Chapter6: Simulation model details and controller design steps are explained.
Chapter7: Test results are demonstrated with the controller performance.
Chapter8: Conclusion and future works are discussed.

1.7 Original Contributions to the Literature

Temperature effects on output energy of actively Q-switched diode pumped solid state laser are investigated and dynamically modeled. Generally, these type of laser sources are designed to satisfy output energy requirement at ambient temperature extremes and in between the output energy is very large compared to the extremes which results in unnecessary power consumption. In this study, the pump drive current is regulated providing power efficient design. In the model, dynamical relations are also added for simulating the time behaviour of the laser source.

With this model, robust closed loop system is designed, optimally tuned, manufactured and verified for wide temperature range. The system includes a PID controller with derivative filter as feedback and a compensator as feed-forward placed on the disturbance which is ambient temperature. Some studies mentioned in Section 1.4 used combinations of PID controller for different laser sources but in this study we included feed-forward compensator for disturbance rejection to regulate the actively Q-switched, diode pumped, solid state laser. Furthermore, all controller parameters are tuned optimally by using steepest descent method while the plant is exposed to aggressive disturbance.

By using Web of Science, "laser", "power", "stabilization", "current" and "control" keywords were searched together in all fields. The search engine found 80 articles. Among them, no related article with this work was observed.

CHAPTER 2

SYSTEM DESCRIPTION AND DEFINITION OF PROBLEM

2.1 System Description

In the present study, diode laser pumped, electro-optical q-switched, solid state laser is examined (Figure 1.5). The block diagram is given in Figure 2.1 :

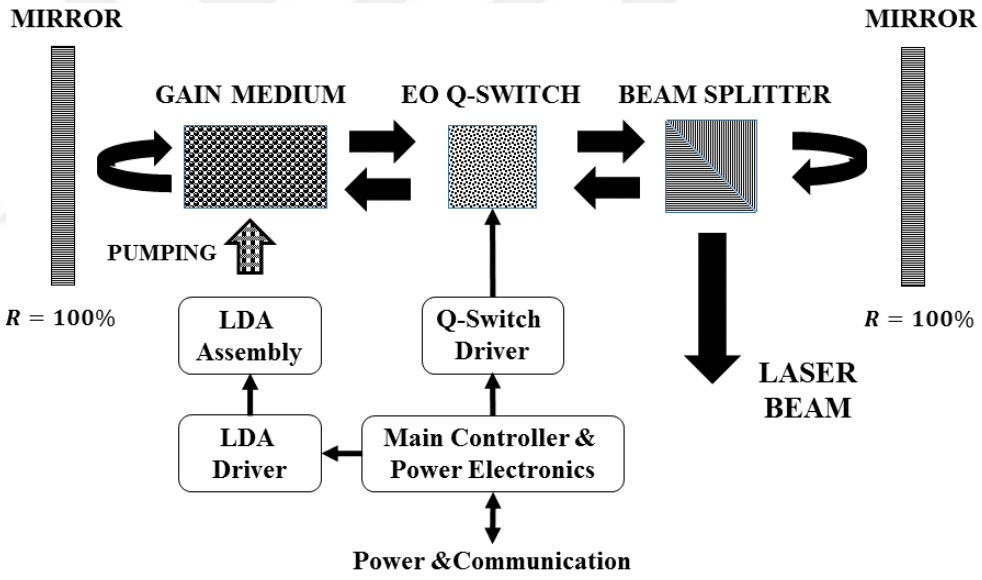

Figure 2.1: System of Present Study: Diode Laser Pumped, Q-Switched, Solid State Laser

2.1.1 Components

Neodymium (Nd^{+3}) doped Yttrium Aluminum Garnet (YAG) crystalline which is one of the typical laser active materials is used as the gain medium due to its excellent thermal, mechanical and optical properties over other materials [22]. The crystalline

is grown to large dimensions (boule) and then went through several fabrication processes such as extraction of a crystal that has specific geometry for the application, polishing and coating. Some Nd:YAG crystals with different geometries and boules are illustrated in Figure 2.2.

Figure 2.2: Different Nd:YAG Crystal Geometries [4]

The resonator also consists two highly reflective mirror for selective feedback. These mirrors have anti-reflection coating at the laser wavelength to decrease resonator losses.

Unlike the basic laser source schematic (Figure 1.3), this system has Q-switch component which is used for storage of the pump energy inside the gain medium and releasing it in a form of very short laser pulse. Before the pump pulse, the switch is opaque which prevents laser and gives rise to the storage. After pump pulse, the switch becomes transparent and the stored energy suddenly released in an extremely short time. For this purpose, an electro-optic Q-switch which is switched by high voltage pulse is used.

With the Nd:YAG gain medium, high reflective mirrors, the electro-optical q-switch and additional optics form the resonator assembly.

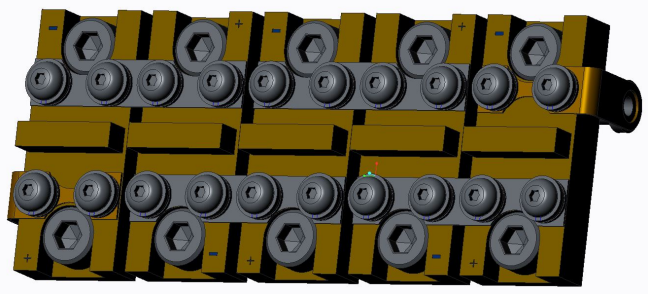

(a) CAD model of LDA Assembly

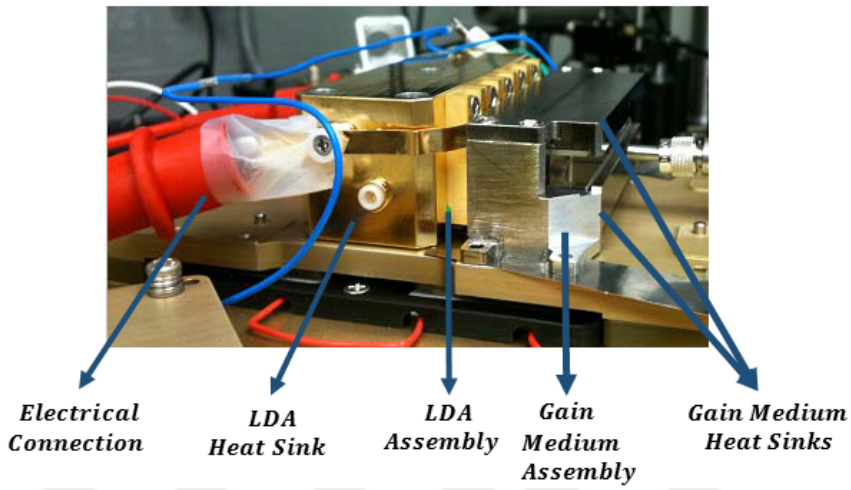

(b) LDA and Gain Medium Assemblies

Figure 2.3: CAD Model of LDA with LDA and Gain Medium Assemblies

Quasi-continuous wave (QCW) operated laser diode arrays (LDA) are utilized as pump source due to being the most efficient method for Nd:YAG pumping (See Figure 2.3 (a)). The advantages of LDA' s are listed as:

- Improved Overall System Efficiency,
- Increased Beam Quality,
- Modular and Compact System Design,
- Increased Reliability and Lifetime.

The LDA' s are manufactured by packaging laser diodes together for having high power densities. There are various packaging and cooling techniques for these multibar arrays. An assembly method developed by Northrop Grumman Cutting Edge Optronics (NGCEO) is given in Figure 2.4. In the method, laser diode bar is mounted on thermal expansion coefficient matched heat sink by using hard solder, AuSn. Then,

mounted bar assemblies are placed between electrical contacts and a common heat sink forming a single LDA.

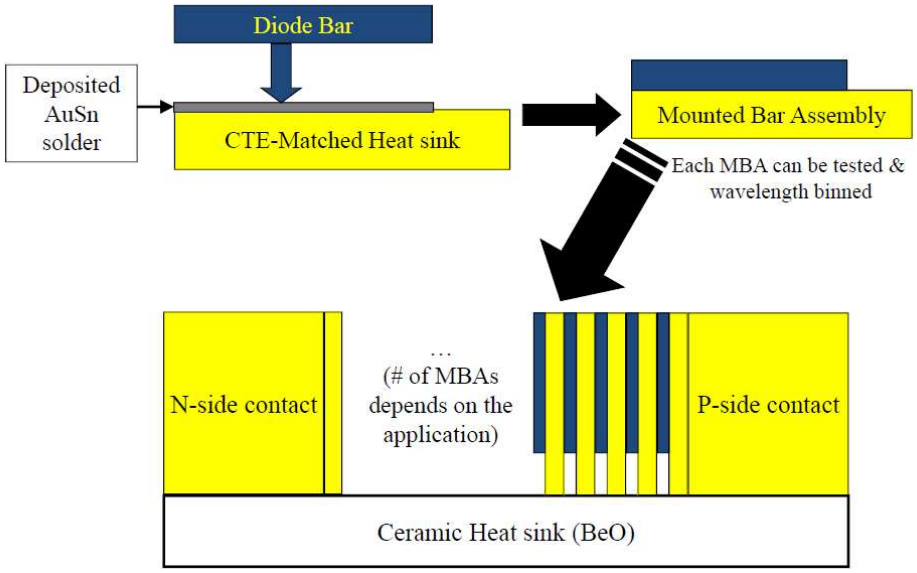

Figure 2.4: An Assembly Method for High-powered Quasi-continuous Wave Arrays [5]

The output power of a QCW operated LDA can be tuned directly by controlling the peak pulse current[23]. The P-I and V-I curves of an LDA used in the system is given in Figure 2.5. Below 27.7 A, there is no stimulated emission in the LDA. Above that threshold, output power increases linearly with current. The slope efficiency is 8.96 W/A.

The slope efficiency and the threshold current of an LDA depends on internal losses such as quantum efficiency and semiconductor resonator loses which are directly related to the temperature. Moreover, spectral characteristics such as center emission wavelength and spectral width also depend on temperature. All these dependencies directly effects the output energy. In this study, impacts of LDA characteristics on the output energy are deeply investigated.

Main system controller, power electronics, diode and Q-switch drivers are the electronic components of the system. The main controller creates the timing signals and make built in tests of the full system. The power electronics circuits generates several voltage levels for the electronic components of the system. The diode driver controls the necessary power transferred to the pumping LDA' s and performs load tests. The

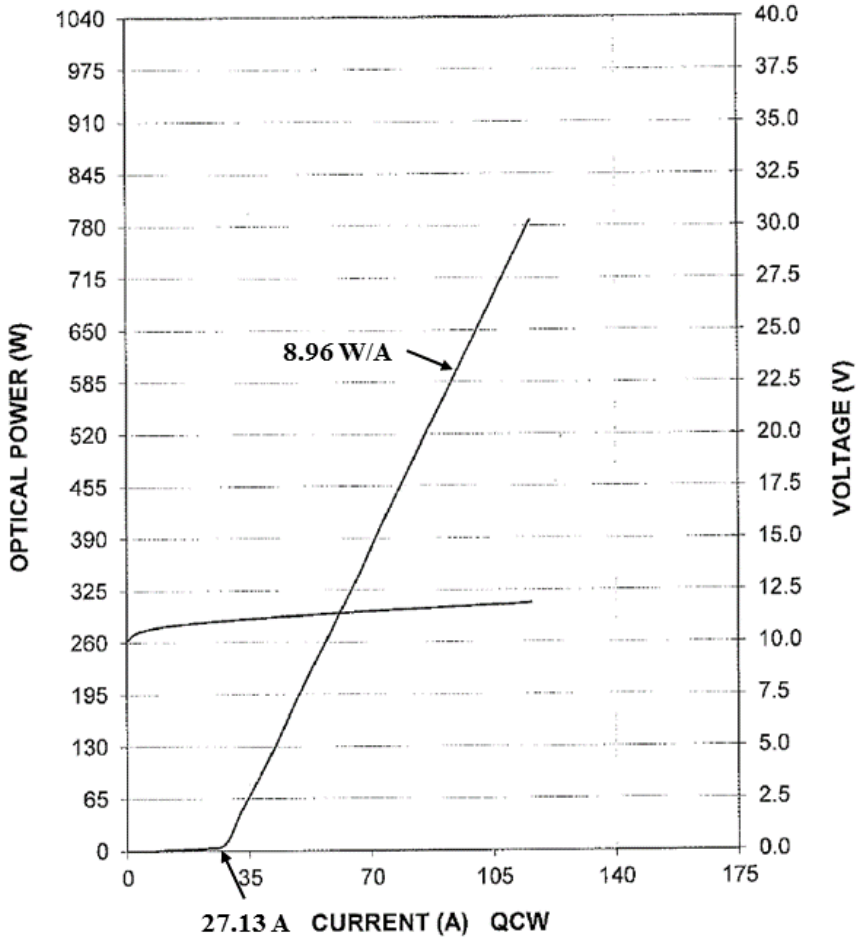

Figure 2.5: Power and Voltage versus Current Plot of a Laser Diode Array

Q-switch driver generates high voltage pulses with very short rise time enabling a powerful laser output.

The electronic components have their own analog feedback regulators. Therefore, temperature effects on the electronics are neglected for this study.

Note that, detailed descriptions of some components are not given here in order not to reveal confidential know-how of ASELSAN about designing such a laser source.

2.1.2 Operation

The system radiates short pulses with user-defined pulse repetition frequency (PRF). The radiation is started and stopped via serial communication. The required duration of operation depends on application.

2.1.3 Performance

The overall performance of laser systems relies on joint performances of the system components. The performance metrics can be listed as:

- pulse width,
- wavelength,
- divergence,
- maximum duration of operation,
- output power/energy.

Pulsed lasers emits optical power in intervals of time. These intervals range from sub-attosecond ($10^{-18}s$) to CW depending on the design of laser source.

Wavelength of a laser source is determined by the gain medium choice that is decided by application and the reflectance spectra of feedback mirrors.

A laser beam enlarges as it propagates. The metric of enlargement is called as divergence. This parameter is also tuned by application requirements.

The laser source should operate until it achieves specific mission. As the source operates, there occurs heat generation due to non-ideal energy transfers between system components. Therefore, the operation may be limited by excessive heating. Laser sources should be analyzed and appropriate heat removal techniques should be considered for accomplishment of the maximum duration of operation.

To perform a process such as signal generation for optical sensor or material processing, the power/energy output from a laser source should ensure specific level required by the process. The output power and energy relation of pulsed laser can be simplified as:

$$E = P_{PEAK} \cdot t_{pulse}, \tag{2.1}$$

where E is the pulse energy, P_{PEAK} is the peak pulse power, and t_{pulse} pulse duration.

2.1.4 Design Constraints

Depending on the utilization, consumers and laser application developers decide the performance parameters with trade off between size, weight, power consumption and price. In addition, there exist standards which regulate these parameters for general or military usage. All these constraints make design of a laser source challenging task which requires multidisciplinary activities such as optics, opto-mechanics, solid state and electronics engineering.

In military applications, laser sources can be used as man-portable equipment or can be integrated to different platforms like UAV and combat aircrafts. Therefore, the design should have smallest size and weight. In addition, it should operate in harsh environmental conditions such as wide temperature range (-20 °C to 50 °C), wild vibration-shock disturbances, variable pressure and humidity levels.

For man-portable systems or UAV payloads, power consumption is also critical. A power efficient system provides smaller batteries and extends flight duration of UAVs.

As a result, designers may not be able to use thermoelectric coolers and heaters for climate control as they introduce extra weight and power consumption to the system. In addition, damping of vibration or shock may not be feasible by the aid of mechanical absorbers due to similar reasons. The isolation from a harsh operating environment is almost impossible for all military applications because battles happen in such adverse weather conditions. Hence, to stabilize the parameters of these systems, robust control algorithms and necessary hardware should be implemented and tested rigorously. In this study, being a key system parameter, output energy will be put under the scope for purpose of improved stabilization over a wide range of environmental disturbances.

2.2 Problem Definition in Depth

For the sake of completeness, this section starts with evaluating the system in terms of the performance parameters given in Section 2.1.3; the system under investigation emits pulses with almost constant pulse duration, the wavelength of emission is also

constant and 1064 nm (invisible to human eye), the divergence can be set to a desired value and remains constant, and the system is guaranteed to achieve the maximum required duration of operation in all working conditions.

The system accomplishes all of the above requirements. Yet, the output energy can vary drastically. In Figure 2.6, measurements of the output energy of the system for over 100,000 pulses are given. Tests are conducted inside a climatic cabinet to illustrate system behavior to temperature alteration (-32 °C to 55 °C). In addition, PRF is swept from 10 to 20 Hz randomly.

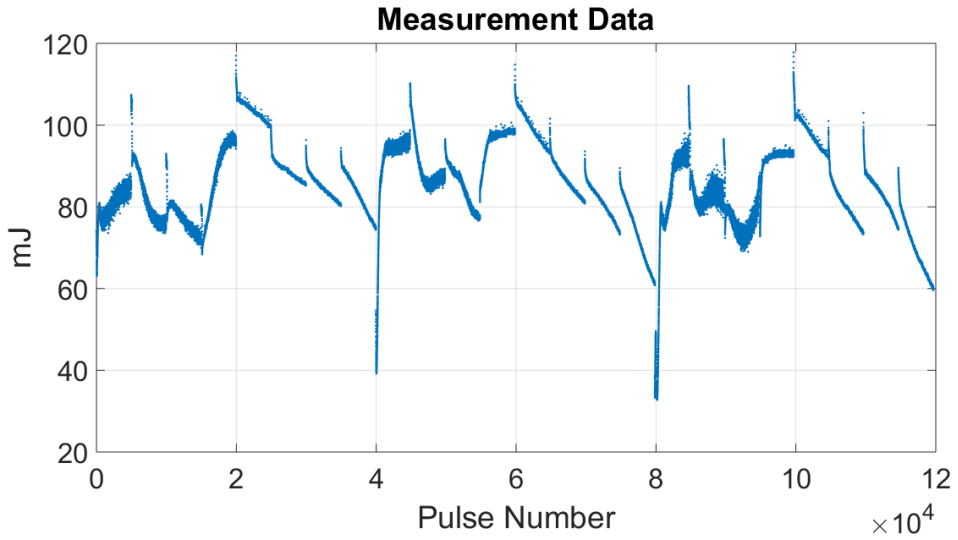

Figure 2.6: Output Energy: Experimental Results; 119658 Pulse, Maximum: 117.8 mJ, Minimum: 32.8 mJ

The reasons causing output energy variations are divided into two main categories as; thermal and aging effects.

2.2.1 Thermal Effects

The most dominant instabilities on output energy are induced by thermal effects:

(i) Emission spectrum and output power of the pump diode lasers changes with temperature.

(ii) Mismatching in coefficient of thermal expansion of opto-mechanical assemblies will cause output energy degradation.

(iii) Active medium is exposed to a phenomenon known as thermal lensing which affects output energy.

(iv) The effective stimulated emission cross section of the gain medium decreases with increasing temperature causing a dreg in the output energy.

2.2.1.1 Effects of Temperature on Pump Diode Characteristics

Temperature of LDA depends on packaging method, ambient and operating conditions. Unless it is actively controlled, the temperature may vary dramatically during operation, causing disturbances on spectral properties of the pump laser.

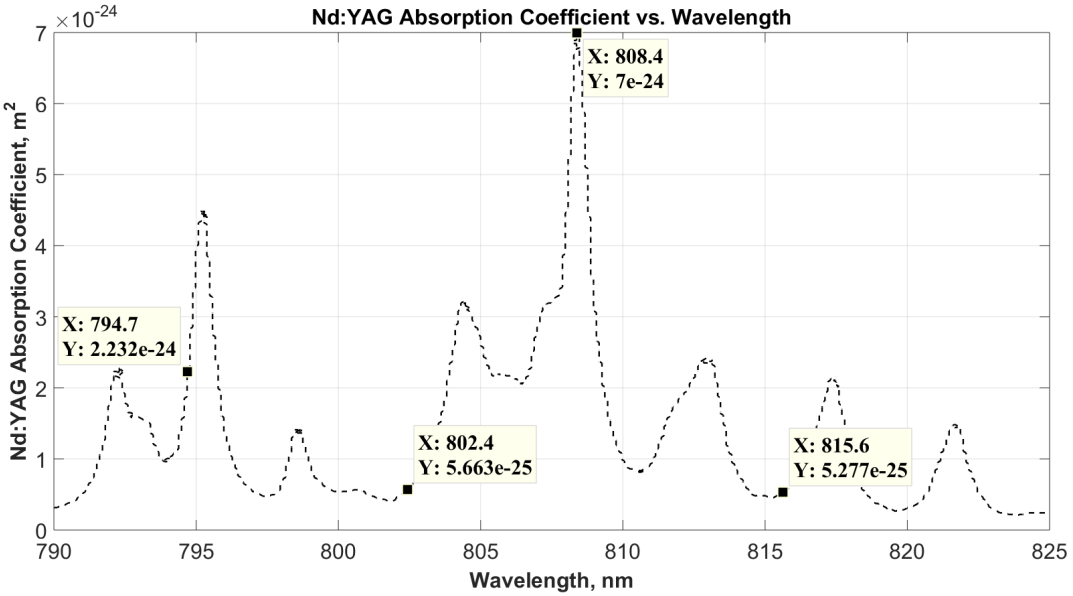

Figure 2.7: Absorption Spectrum and Cross Section of Nd(1%):YAG versus Wavelength [6]

Peak wavelength of the pump emission changes with temperature. A typical value is $\approx$ $0.24\ nm/°C$. For temperature range of -32 °C to 55 °C, there is approximately 22 nm shift from center emission wavelength [24] but the absorption coefficient (absorption length) of laser gain medium critically depends on pump wavelength. There must be a spectral match between the laser diode emission and the Nd absorption [11]. The absorption spectrum of Nd(1%):YAG with illustration of wavelength shift of an LDA whose peak emission wavelength is 808.4 nm at room temperature is given in Figure 2.7. It is obvious that, 22 nm change around 808 nm, the absorption profile varies drastically causing fluctuations on the output energy. Closer look at Figure 2.7,

even 1 nm drift causes absorption cross section drop out 50 % around 808 nm. 1 nm corresponds to $\approx 4°C$ temperature shift only. The absorption cross section values for different temperatures are tabulated in Table 2.1.

Table2.1: Table of Wavelength Shift Caused by Temperature

Temperature, °C	**Wavelength, nm**	**Abs. Cross Sec., m^2**
-32	794.72	2.23×10^{-24}
0	802.4	5.7×10^{-25}
25	808.4	7×10^{-24}
55	815.6	5.3×10^{-25}

In addition, as the drive current supplied to the LDA increases, the junction temperature is also increases causing expansion of the spectral width of the emission. The expansion is depicted in Figure 2.8. The spectral width for 100 A peak drive current is around 3 nm (FWHM) whereas it is roughly 1 nm (FWHM) for 20 A drive current. The spectral width defines the spectral overlap integral between diode and absorption cross section.

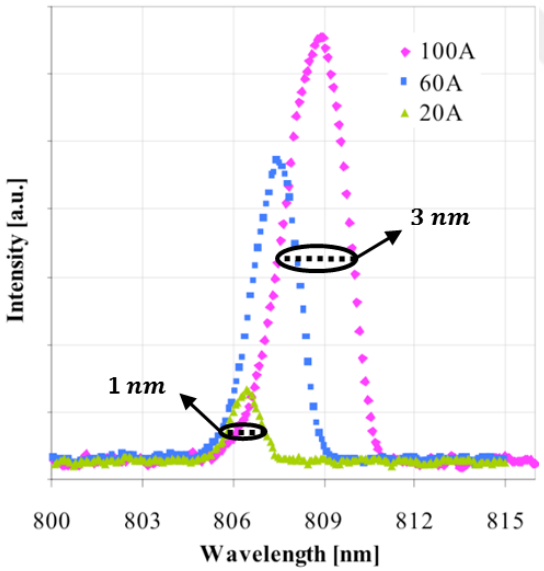

Figure 2.8: Average Spectrum at Three Different Drive Currents of a Conductively Cooled 2-bar Laser Diode Array [7]

Output power of an LDA changes with temperature. Percentage power change versus temperature of laser diode array assembly which is used in this study is measured and given in Figure 3.3. Output power decreases with increasing temperature.

These complex effects of temperature on laser diodes manifest themselves as difficult to model the variation on the output energy. Active temperature control equipments such as thermoelectric coolers can be used to minimize the effects in combination with external air cooling but they are size and weight inefficient [25].

2.2.1.2 Effect of Unmatched Thermal Expansion Coefficients

Figure 2.1 represents an overly simplified view of the actual laser resonator. In reality, it has many optical components which are bonded to their holders and mounted to the main frame of the system. These optical components have different physical properties. Their holders can be made from various materials such as aluminum, stainless steel, titanium which have different coefficients of thermal expansion. Besides, there are various types of adhesives used for bonding processes. They also have different thermal characteristics. Consequently, all these discrepancies may cause misalignment depending on temperature. In Figure 2.9, tilt of a high reflective mirror in a basic laser resonator is simulated. In [8], it is calculated that even ≈ 30 μrad tilt will result in 10 % output energy decrease. Opto-mechanical methods to mitigate this problem are discussed depth in [8]. Nonetheless, over the temperature range of concern some effect still remains.

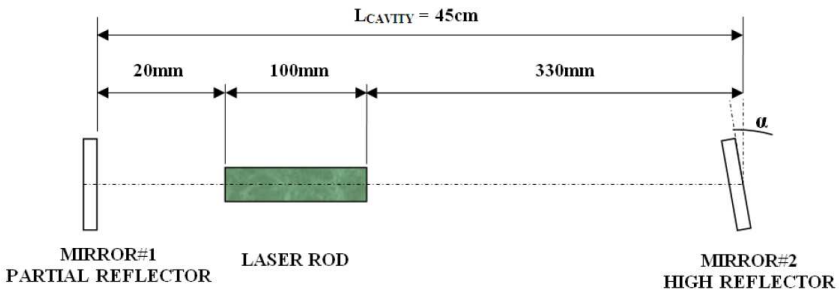

Figure 2.9: Sample Laser Resonator with High Reflector Tilted by an Angle of α, [8]

2.2.1.3 Gain Medium Characteristics

Intrinsic thermo-optical properties of the gain medium is affected by temperature[9]. The emission cross section (σ_e) of the gain medium decreases with temperature as shown in Figure 2.10. At -32 °C and 55 °C, σ_e is $2.4684 \cdot 10^{-19}$ cm^2 and $2.1465 \cdot 10^{-19}$ cm^2, respectively. This resulted in 13% decrease in σ_e for the corresponding temperature range. That is at high temperatures, the gain material is 13% less efficient.

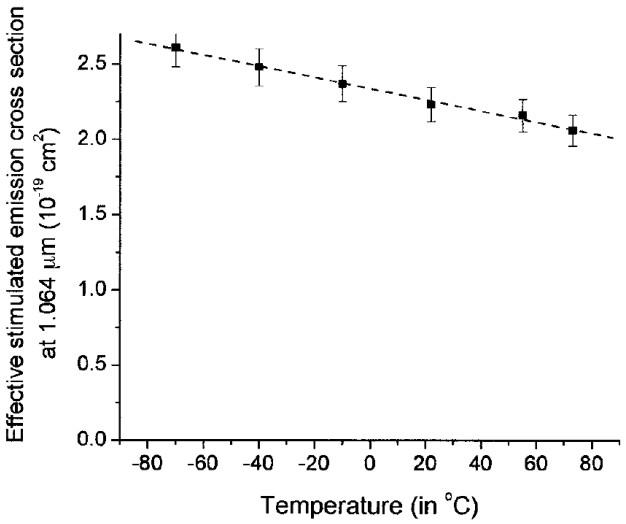

Figure 2.10: Peak Effective Emission Cross Section at 1064μm of 1% Nd:YAG is a Function of Temperature [9]

In addition, because of the optical pumping, heat generation occurs in the gain medium. The generated heat causes temperature gradient across the host crystal. As a result, refractive index inside the gain medium changes and creates lens effect. This phenomenon is called as thermal lensing [26]. The thermal lensing changes the diffraction loss (δ) of the resonator directly effecting the output energy.

2.2.2 Aging Effects

2.2.2.1 Optical Coatings

Optical substrates are coated with thin film layers to perform various functions such as anti-reflection, filtering and high reflection. These coatings should withstand the

military environmental stresses. They are also facing laser pulses with very high peak powers in the range of several megawatts. Hence, the performance of the optical coatings may degrade and cause energy to drop, overtime.

2.2.2.2 LDA Aging

Although being more reliable than the other pump sources, operating conditions may shorten LDA' s lifetime. For example, thermal cycle that the LDA encounters because of repetition rate, drive current and the ambient temperature may cause optical power degradation. In addition, the LDAs may be exposed to shock and vibration which may accelerate aging effects [27], [28]. In Figure 2.11, lifetime tests of 15x4 bar LDA's of NGCEO is given. Around 9 billion shots, total output power decreases 10 %.

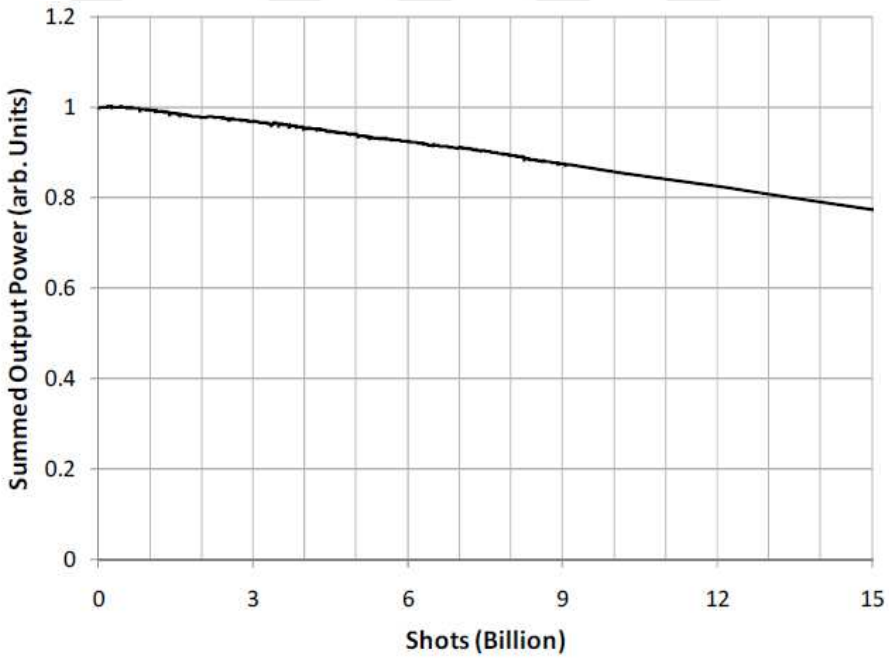

Figure 2.11: 15x4 Bar LDA Total Power versus Shot Graph [10]

CHAPTER 3

SYSTEM MODEL

The system is modeled both using physical relations and basic system identification techniques.

3.1 Model: Physical Relations

The system is divided into two blocks based on their functional behaviour. Block diagram of the overall system is illustrated in Figure 3.1. The first block takes current as an input and produces pump radiation for the resonator. From now on, this part of the system is called as "actuator" to provide consistency with the control engineering literature. The second block is the resonator which takes the pump radiation as an input and forms the laser pulses. This block is named as "plant".

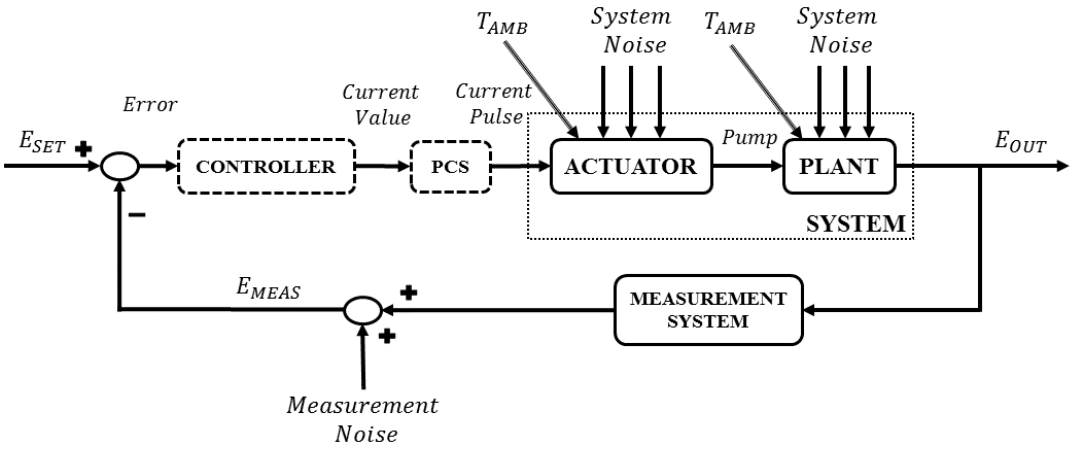

Figure 3.1: Block Diagram of the Feedback Control System in this Study

The controller calculates current pulse amplitude for desired E_{SET} and feed it to the Pulsed Current Source (PCS). The PCS generates current pulses with constant pulse duration and variable amplitude. The actuator creates the pump and then the pump is injected to the plant. The output energy of the plant is sampled by the measurement system.

The ambient temperature, (T_{AMB}), directly affects the actuator and plant as discussed in Section 2.2.1. Hence, its impact is modeled as disturbance to the system. There are also noise sources effecting both the system and measurement. The main source of the system noise is caused by LDA's characteristics and the measurement noise is result of the sensor as well as processing electronics.

3.1.1 Actuator Model

The actuator part of the system is basically the LDA assembly. It consists serially connected 5 LDAs (Figure 2.3).

When the current pulse is supplied to the LDA assembly, it emits pump light which is characterized by its power, $P_P(t)$, and spectrum, $\lambda_P(\lambda)$, (Figure 3.2). In this study, the LDA assembly is driven with current pulses of constant duration and variable amplitude. The reason of having current pulses with constant duration is related to fluorescence lifetime of the Nd^{+3} ions in the gain medium which is constant.

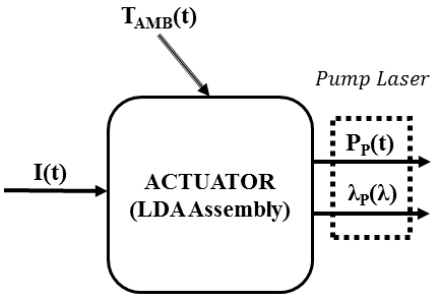

Figure 3.2: Actuator

λ_P and P_P are the sum of each LDA output emission spectra and power:

$$P_P = \sum_{i=1}^{5} P_{P,i}(I, T_d)$$
$$\lambda_P = \sum_{i=1}^{5} \lambda_{P,i}(T_d) \tag{3.1}$$

where $i = 1, 2, ..., 5$ is LDA index, $P_{P,i}$, $\lambda_{P,i}$, T_d and I are the output power, the emission spectrum of the single LDA, LDA assembly temperature and drive current, respectively. The $P_{P,i}$ can be written as:

$$P_{P,i} = \sigma_{se,i}(T_d) \cdot (I - I_{th,i}) \tag{3.2}$$

The $\sigma_{se,i}$ and $I_{th,i}$ in Equation 3.2 are slope efficiencies and threshold currents respectively. Here, $\sigma_{se,i}$ and $\lambda_{P,i}$ depend on the LDA temperature, T_d.

Each LDA shows different characteristics caused by fabrication processes. To identify the operation of an LDA, 130 LDAs were tested and distributions of these parameters were examined in Section 5.1. The distribution of manufacturing dependent parameters are introduced to the model as system noise. In this section, dependences of these parameters on LDA temperature are examined.

(i) **Slope Efficiency, ($\sigma_{se,i}$) and Threshold Current, ($I_{th,i}$):** It is measured that typical value of the slope efficiency and the threshold current at T_d = 50 °C is 8.96 W/A and 27.13 A, respectively (Figure 2.5). As temperature increases, the slope efficiency decreases and the threshold current increases. Hence, the output power decreases. We measured the output power with respect to T_d for 3 different drive currents. Normalized results are given in Figure 3.3. The output power decreases with 0.3 % per °C.

As drive current changes, trend of the output power with respect to T_d shows similar characteristics. Small differences caused by drive current on the trend are neglected.

In the model, the dependence of the output power on T_d is reflected on to the slope efficiency and the threshold current is assumed to be constant because of linearity.

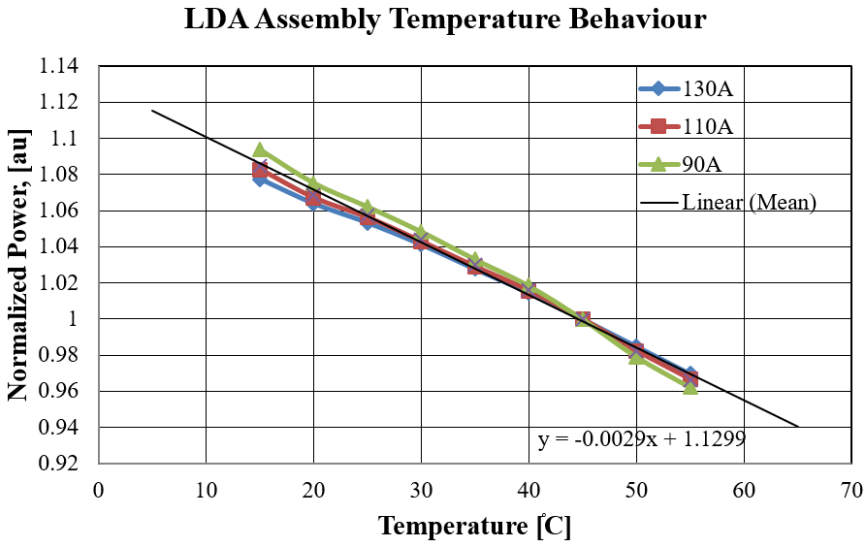

Figure 3.3: Measured Average LDA Temperature Behaviour, Output Power Characterization

The slope efficiency is calculated as:

$$\sigma_{se,i}(T_d) = -0.0274 \cdot T_d + 10.331 \tag{3.3}$$

Note that, as the laser diode arrays age, the slope efficiency will degrade eventually. This can not be modeled because each system will face different operating conditions changing the degradation level.

(ii) **Emission Spectrum, $\lambda_{P,i}$:** Each LDA has an emission spectrum curve similar to the Figure 3.4. This curve is defined by its center wavelength and spectral width in the laser literature. Generally, Gaussian bell curves are used to represent the spectrum and calculate effective absorption of the gain medium inside the plant. To verify this, from the 130 LDAs, 8 of them were chosen arbitrarily and their spectra were measured. Then, they are fitted to single and then sum of two Gaussians for comparison (in a least-squares sense). Results are shown in Figure 3.5. Note that, on the left top of each figure, the sum of squares error resulting from a single Gaussian fit is shown as "Gaussian1 SSE" and sum of two Gaussians is represented by "Gaussian2 SSE".

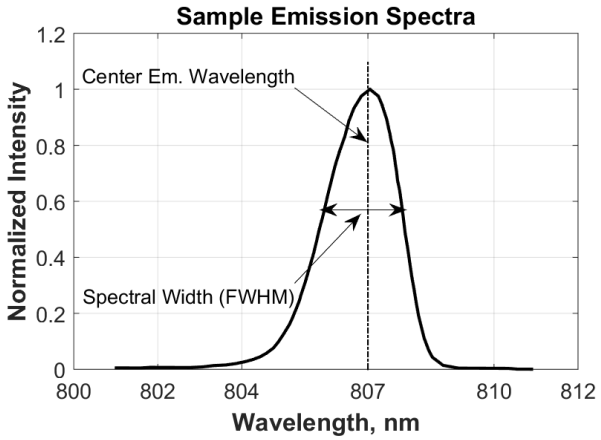

Figure 3.4: Emission Spectrum of an LDA

Merit of fit is calculated as sum of squares due to error:

$$SSE = \sum_{1}^{n} (y_i - \hat{y}_i)^2 \tag{3.4}$$

where y_i is the measurement, $\hat{y}_i$ is the Gaussian fit and n is the data point. These SSE' s are listed for 8 LDAs in Table 3.1.

Table3.1: SSE List for Gaussian Fits

Part Number	**SSE Using 1 Gaussian**	**SSE Using 2 Gaussians**	**Sum Squares of Data Points**
CN23299	0.18652	0.011632	19.4749
CN23300	0.090355	0.073974	17.7825
CN23301	0.31223	0.0074638	21.6864
CN23302	0.13429	0.0048957	21.8574
CN23303	0.081227	0.0028129	24.4423
CN23304	0.14577	0.0073023	17.7189
CN23305	0.137	0.0059286	23.2646
CN23306	0.21289	0.011035	25.1526

In general, sum of two Gaussian distributions fit better than single Gaussian. However, by comparing the SSE of fits with sum squares of the data, using single Gaussian has SSE smaller than 1 % of the sum squares of data. To reduce computational complexity, single Gaussian approximation is used in this study.

As a result, each emission spectrum of an LDA ($\lambda_{P,i}$) is modeled as Gaussian with $\mu_i(T_d)$ center emission wavelength dependent to LDA temperature and σ_i^2 variance:

$$\lambda_{P,i}(\lambda) = \frac{1}{\sqrt{2\pi}\sigma_i} \cdot \exp \frac{-(\lambda - \mu_i(T_d))^2}{2\sigma_i^2} \tag{3.5}$$

The relation between FWHM spectral width and σ_i^2 after single Gaussian function assumption:

$$\sigma_i = \frac{FWHM}{2 \cdot \sqrt{(2 \log 2)}} \tag{3.6}$$

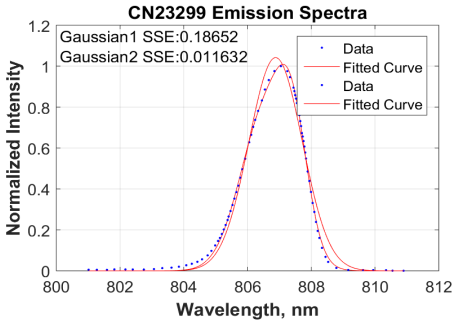

(a) $CN23299$

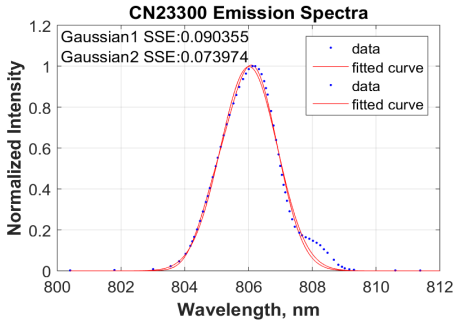

(b) $CN23300$

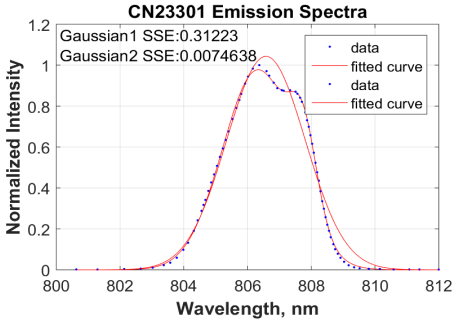

(c) $CN23301$

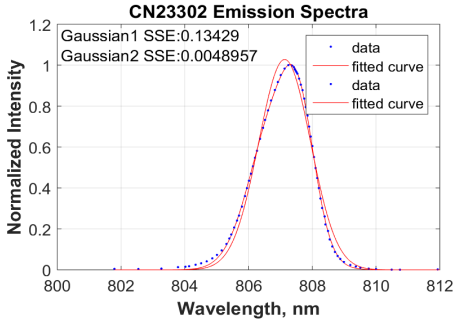

(d) $CN23302$

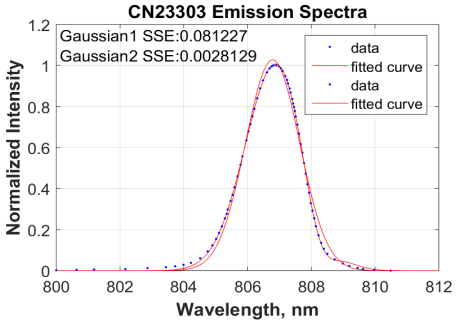

(e) $CN23303$

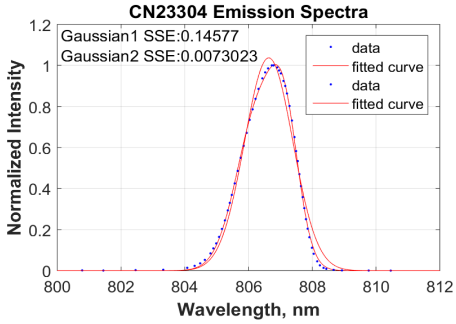

(f) $CN23304$

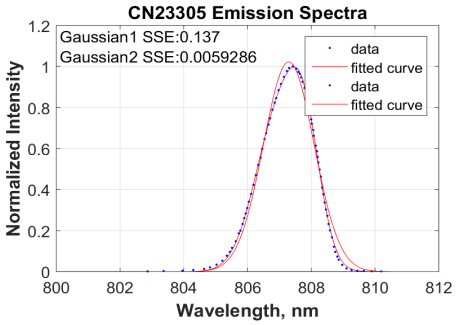

(g) $CN23305$

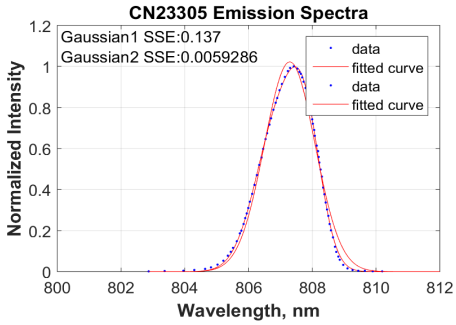

(h) $CN23306$

Figure 3.5: Gaussian Fits for LDA Emission Spectra

(iii) **Center Emission Wavelength, $\mu_i(T_d)$:** Typical value at $T_d = 50°C$ is 807.8 nm. Its temperature dependence is also measured and plotted in Figure 3.6. The linear relation between LDA temperature and center emission wavelength is given by Equation 3.7.

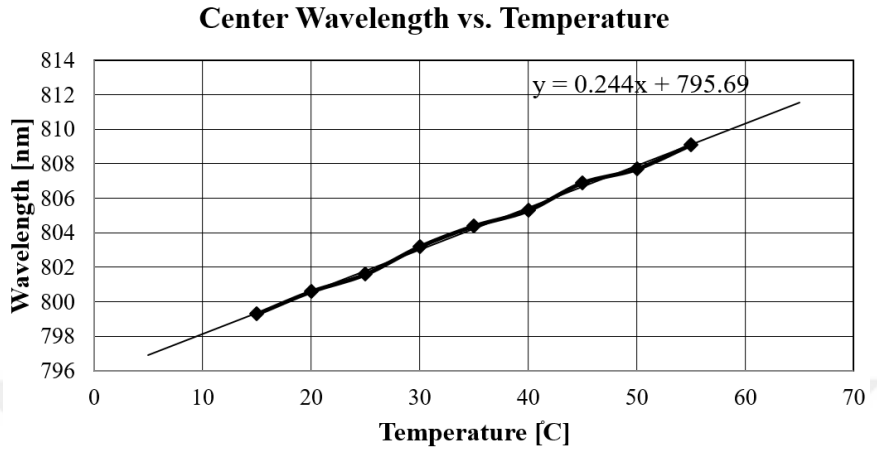

Figure 3.6: LDA Center Emission Wavelength Shift Due to T_d, (S/N:CM26183)

$$\mu_i(T_d) = 0.244 \cdot T_d + 795.69 \tag{3.7}$$

(iv) **Spectral Width, σ, (FWHM):** The typical value is 1.9 nm at 100 A. However, this value increases with current. Its variation was measured for 5 LDAs with respect to the drive current and the measurement is normalized to its value at 100 A drive current. The resulting plot is shown in Figure 3.7 and relation is given in Equation 3.8.

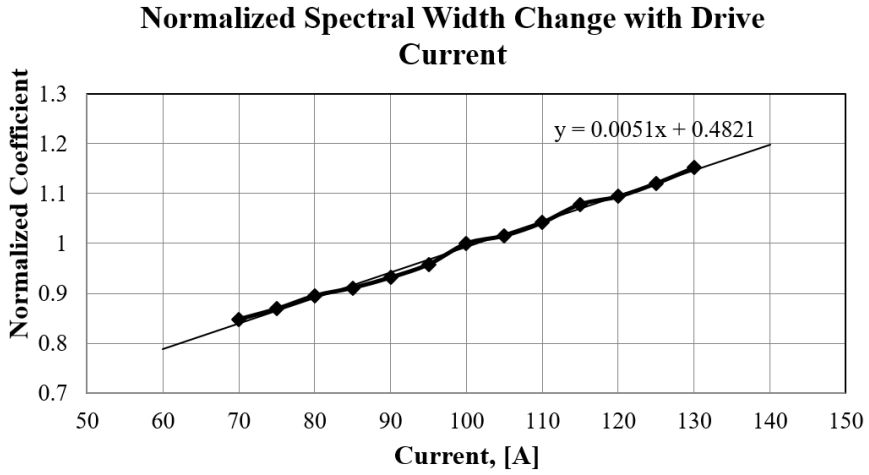

Figure 3.7: Drive Current vs. Normalized Spectral Width Change

$$\sigma_i = 0.0097 \cdot I + 0.9160 \tag{3.8}$$

(v) **LDA Temperature, T_d:** It is one of the most dominant parameter in the system because of affecting both emission spectrum and optical output power of LDA.

The ambient temperature, PRF, LDA characteristics and heat sink parameters determine the LDA temperature. In Figure 3.8, a basic dynamical heat flow model is shown with the assumption of uniform heat generation inside the LDA. In the model, dissipated power as heat, P_D, flows through junction of LDA, LDA casing, heat sink and ambient. Each contact has its own thermal resistance. Here, the thermal resistance of LDA case to heat sink is ignored by assuming perfectly polished contact surfaces of LDA case and heat sink.

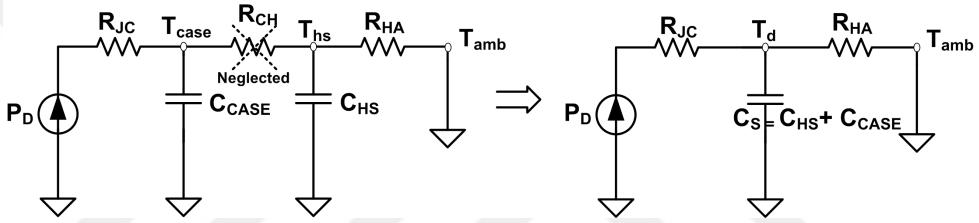

Figure 3.8: LDA Temperature Heat Flow Model Simplification

The LDA temperature and dissipated power are related to:

$$\begin{aligned} P_{D1} &= C_{s1} \cdot \frac{dT_d}{dt} + \frac{T_d - T_{amb}}{R_{HA1}} \\ P_{D1} &= P_{in} - P_P = \sum_{i=1}^{5} I \cdot V_i(I) - \sum_{i=1}^{5} \sigma_{se,i}(T_d) \cdot (I - I_{th,i}) \end{aligned} \tag{3.9}$$

By re-arranging the terms in Equation 3.9:

$$\frac{dT_d}{dt} = \frac{1}{C_{s1}} \frac{T_{amb} - T_d}{R_{HA1}} + \frac{1}{C_{s1}} \cdot \left[\sum_{i=1}^{5} I \cdot V_i(I) - \sum_{i=1}^{5} \sigma_{se,i}(T_d) \cdot (I - I_{th,i}) \right] \tag{3.10}$$

where the heat capacitance C_{s1} can be found by using masses and specific heats of LDA case and heat sink materials which are Copper Tungsten and Aluminum, respectively:

$$
\begin{aligned}
C_{HS1} &= m_{HS1} \cdot c_{Al} \\
C_{CASE} &= 5 \cdot m_{LDA} \cdot c_{CuW} \\
C_{s1} &= C_{HS1} + C_{CASE}
\end{aligned}
\tag{3.11}
$$

The heat sink to ambient thermal resistance, R_{HA1}, consists of two components caused by radiative and convective heat transfer [29]:

$$
R_{HA1} = R_{rad,1} \parallel R_{conv,1} \tag{3.12}
$$

$$
\begin{aligned}
R_{rad,1} &= \frac{T_d - T_{amb}}{5.1 \cdot A \cdot \left[\left(\frac{T_d}{100} \right)^4 - \left(\frac{T_{amb}}{100} \right)^4 \right]} \\
R_{conv,1} &= \frac{1}{1.34 \cdot A} \cdot \left(\frac{d_{vert}}{T_d - T_{amb}} \right)^{\frac{1}{4}}
\end{aligned}
\tag{3.13}
$$

where A and d_{vert} are surface area and vertical height of the heat sink of LDA assembly.

(vi) **LDA Voltage, $V(I)$:** The measured I-V characteristics of a typical LDA is given in Figure 2.5. This curve is almost constant for all 130 units tested. Hence, it is linearized for operating current range:

$$
V_i(I) = 0.0108 \cdot I + 10.698 \tag{3.14}
$$

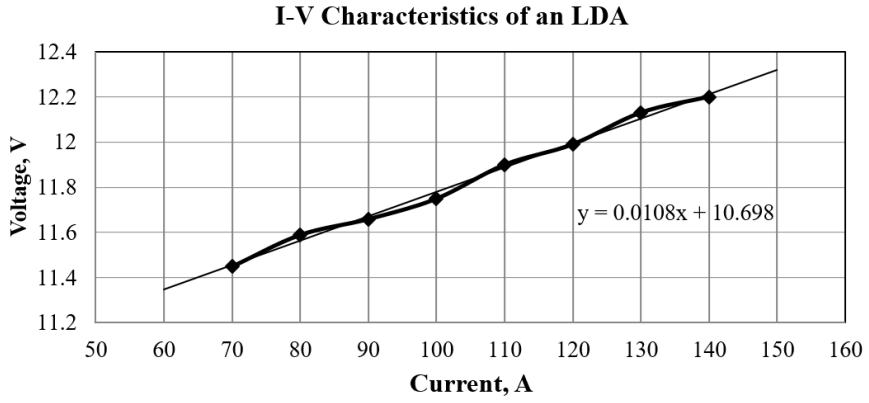

Figure 3.9: Voltage versus Current Plot of a Laser Diode Array

3.1.2 Plant Model

When the plant is excited by the pump radiation, several dynamics step into action sequentially. It starts with the absorption of pump radiation by the gain medium. This process creates population inversion. Existence of the pump radiation with very high resonator losses provides storage of the energy inside the gain medium. After the pump radiation ends, the losses of the resonator is switched to minimum by the electro-optic (EO) Q-switch. This creates a huge laser pulse with very short pulse duration by extracting the stored energy inside the gain medium. The energy flow is illustrated in Figure 3.10.

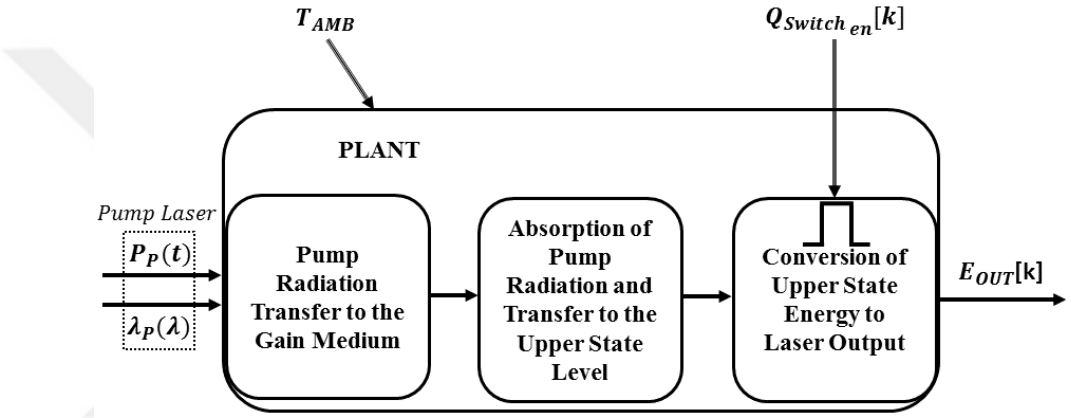

Figure 3.10: Plant Energy Flow Diagram

This dynamic behaviour of lasers are described by coupled rate equations which relate the population inversion and intra-cavity photon densities with pump radiation. The simplified rate equations for four energy level continuous laser systems which are coupled nonlinear ordinary differential equations are given below [11]:

$$\frac{dn}{dt} = -n\sigma\phi c - \frac{n}{\tau_f} + W_p(n_t - n) \tag{3.15}$$

$$\frac{d\phi}{dt} = c\phi\sigma n - \frac{\phi}{\tau_c} \tag{3.16}$$

where n is population inversion density, σ is stimulated emission cross section, c is speed of light, τ_f is fluorescence decay time of the upper laser level, W_p is pump rate, n_t is the total population density, ϕ is intra-cavity photon density, τ_c is decay time of

the photons in the resonator. The simplification is that without loss of precision four energy level system can be represented by considering only the two energy levels which are ground and excited levels [11].

To model the plant dynamics, these equations were modified for Q-switched resonator scheme. There exist two phases of operation namely population inversion phase and Q-switching phase for that scheme.

3.1.2.1 Population Inversion Phase

In the population inversion phase, energy delivered by pump light is stored by the active medium. The rate of change of the laser photon density with respect to time is zero because the resonator does not permit a feedback. Here, Equation 3.15 and Equation 3.16 become:

$$\frac{dn}{dt} = \frac{-1}{\tau_f} \cdot n + \frac{1}{A_{pump} \cdot h\nu_P} \cdot P_P \cdot \sigma_{ab,eff}(\lambda_P) \cdot (n_t - n) \tag{3.17}$$

$$\frac{d\phi}{dt} = 0 \tag{3.18}$$

where A_{pump}, h, ν_P are pump area, Planck's constant and pump frequency respectively. The absorption efficiency, $\sigma_{ab,eff}$, will be discussed in the Section 3.1.2.2.

In Figure 3.11, the calculated dynamics are presented. When 230 μsec 100 A amplitude pulse is supplied to the LDA, the population inversion density accumulates following to the Equation 3.17. Note that, when the pump radiation ends without Q-switching, the population density decays with spontaneous emission only.

3.1.2.2 Effective Absorption Cross Section

The absorption cross section graph of the active medium with respect to pump wavelength which is for monochromatic pump was presented in Figure 2.7. However, emission spectrum of and LDA has finite spectral width. Example of pump emission

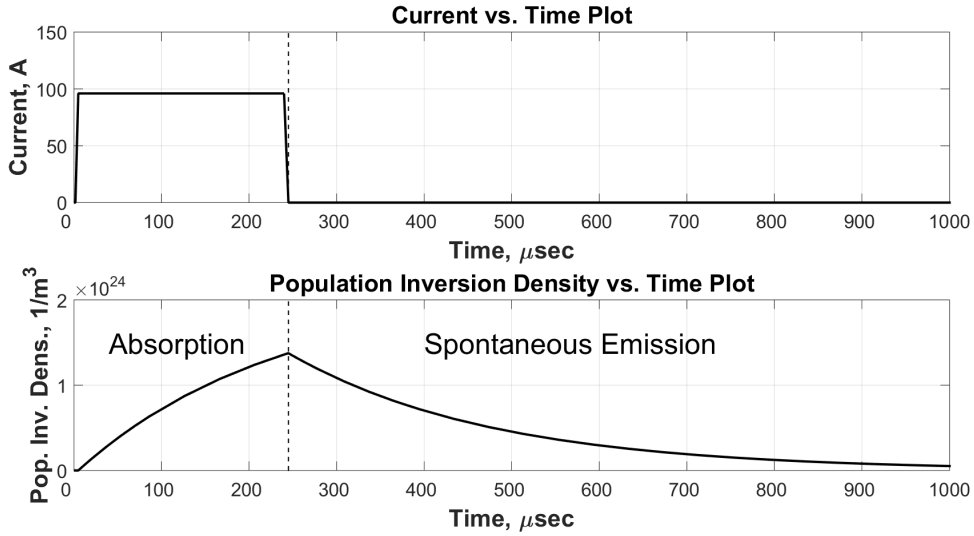

Figure 3.11: Population Inversion Phase

spectrum of 5 LDAs and Nd:YAG absorption coefficient plot with respect to wavelength are superposed in Figure 3.12. To account overlapping in the model, effective absorption cross section is calculated for a pump wavelength band of λ_{min} to λ_{max} as in Equation 3.19.

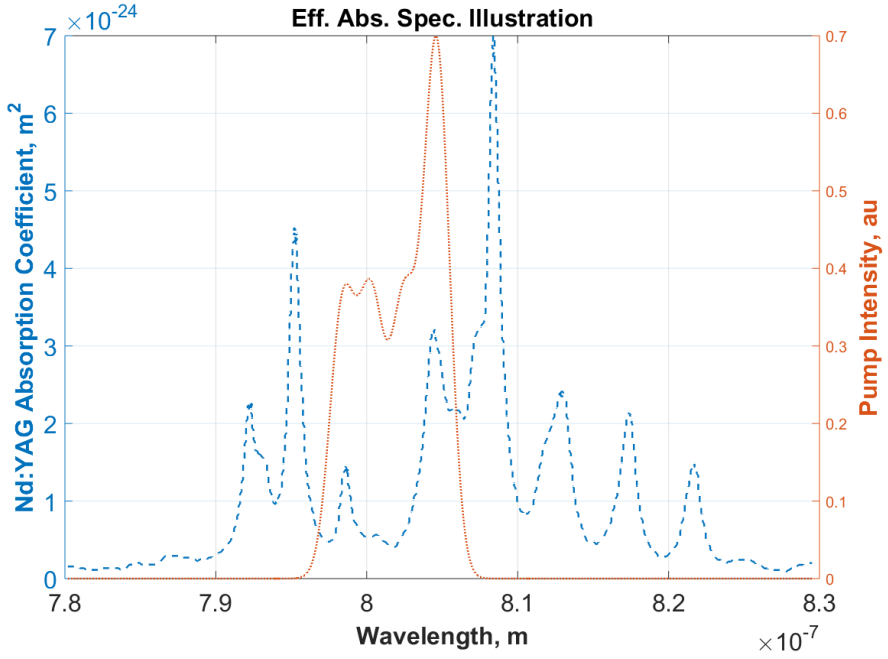

Figure 3.12: Wavelength vs. Absorption Coefficient and Example Pump Spectrum

$$\begin{aligned}
\sigma_{ab,eff} &= \frac{\Sigma_{overlap}}{\Gamma_{pump}} \\
\Gamma_{pump} &= \int_{\lambda_{min}}^{\lambda_{max}} \lambda_P(\lambda) d\lambda \\
\Sigma_{overlap} &= \int_{\lambda_{min}}^{\lambda_{max}} \lambda_P(\lambda) \sigma_{ab}(\lambda) d\lambda
\end{aligned} \tag{3.19}$$

where $\sigma_{ab,eff}$ is effective absorption cross section, $\lambda_P(\lambda)$ is normalized LDA emission spectrum and $\sigma_{ab}(\lambda)$ is Nd:YAG absorption cross section for monochromatic pump wavelength at λ. The $\sigma_{ab,eff}$ is calculated for a single LDA with 807.8 nm center emission wavelength at $T_d = 50°C$ and 2 nm spectral width. The LDA temperature is swept for a range of -20 °C to 50 °C, and the resulting $\sigma_{ab,eff}$ is plotted in Figure 3.13.

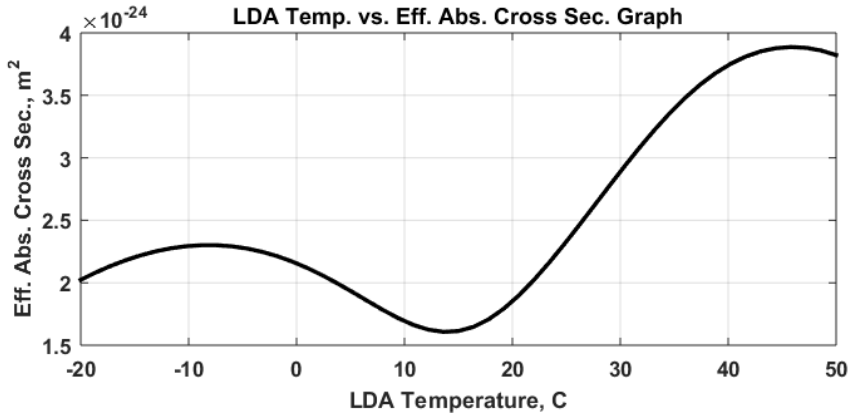

Figure 3.13: Effective Absorption Cross Section Calculation for LDA Temperature

3.1.2.3 Q-Switching Phase

After population inversion phase, the stored energy inside the active medium is extracted by Q-switching technique. With the Q-switch enable signal, the dynamics for this phase are given in Equation 3.20 and 3.21.

$$\frac{dn}{dt} = -c \cdot n \cdot \phi \cdot \sigma(T_{act}) - \frac{1}{\tau_f} \cdot n \tag{3.20}$$

$$\frac{d\phi}{dt} = c \cdot \frac{l}{L} \cdot \phi \cdot n \cdot \sigma(T_{act}) - \frac{\epsilon}{\tau_r} \cdot \phi \tag{3.21}$$

where l, L, ϵ and τ_r are length of the gain medium, length of the resonator, losses in the resonator and round trip time of the light inside the resonator, respectively. The stimulated emission cross section, $\sigma(T_{act})$, which is a function of the gain medium temperature, will be explained in the Section 3.1.2.4.

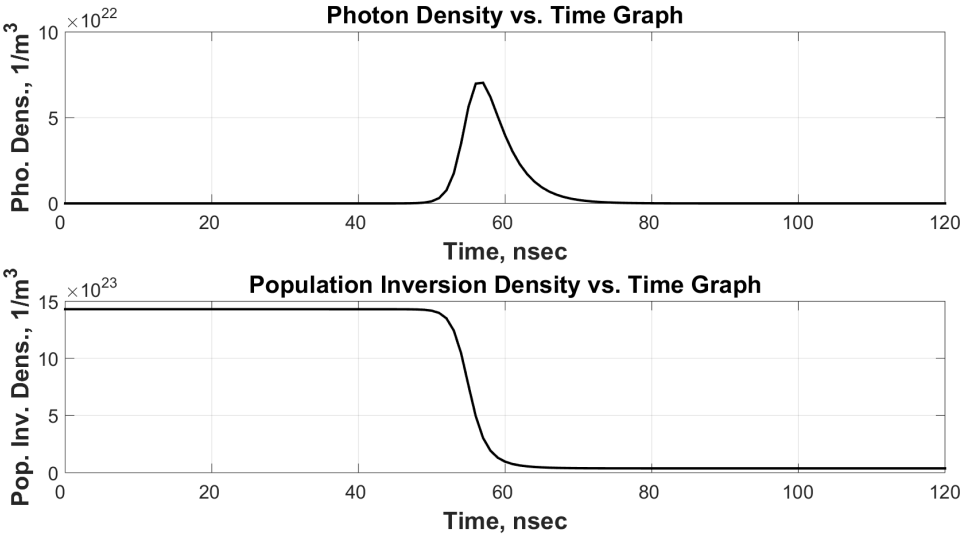

Figure 3.14: Q-Switching Phase

The stored energy inside the gain medium is released in a form of very short pulse with duration approximately 10 nsec by stimulated emission. The calculated waveforms are shown in Figure 3.14.

3.1.2.4 Stimulated Emission Cross Section

From the Figure 2.10, the stimulated emission cross section of the gain medium is:

$$\sigma(T_{act}) = (2.35 - 3.7 \cdot 10^{-3} \cdot T_{act}) \cdot 10^{-19}, \tag{3.22}$$

where σ is stimulated emission cross section in cm^2 and T_{act} is the gain medium temperature in °C.

3.1.2.5 Gain Medium Temperature

Like LDA temperature model, the basic dynamical heat flow model is used also for the gain medium temperature, T_{act}, with the same assumption of perfectly contact between gain medium and heat sink of it. The same flow equation holds for the gain medium (Equation 3.23).

$$P_{D2} = C_{S2} \cdot \frac{dT_{act}}{dt} + \frac{T_{act} - T_{amb}}{R_{HA2}} \tag{3.23}$$

Here, C_{S2}, R_{HA2} and P_{D2} are the total heat capacity of gain medium and its heat sink, heat sink to ambient thermal resistance, dissipated power in the gain medium assembly. These parameters are similar to the LDA temperature model. However, calculation of the dissipated power, P_{D2}, is different. To begin with the dissipated power is a fraction of the absorbed power by the gain medium:

$$P_{D2} = P_{ABS} \cdot \gamma \tag{3.24}$$

where P_{ABS} is the absorbed power by active medium, γ is the fractional thermal loading factor which is measured between 0.37 to 0.43 for Nd:YAG gain medium [30].

To calculate the absorbed power by the gain medium, absorption law of Beer-Lambert will be used. This law describes absorption of light by a sample with thickness t, and absorption coefficient $\alpha(\lambda)$ (Figure 3.15 (a)). It states that for a laser of wavelength λ, output power which is not absorbed by the sample can be found as:

$$P_{OUT} = P_{IN} \cdot \exp(-\alpha(\lambda) \cdot t) \tag{3.25}$$

Here, the absorption coefficient is:

$$\alpha(\lambda) = N_0 \cdot \sigma_{ab}(\lambda) \tag{3.26}$$

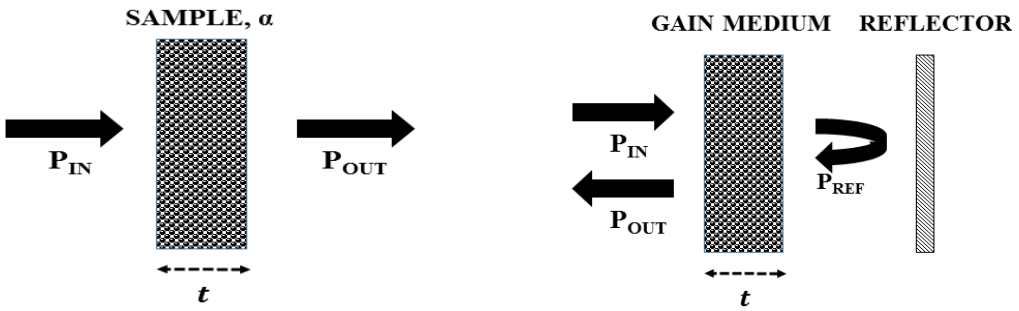

(a) K_i (b) K_d

Figure 3.15: (a) Simple Absorption, (b) Absorption with Reflector

where N_0, σ_{ab} and t are the density of ground level ions, absorption cross section, and the gain medium length, respectively. The absorbed power inside the crystal is calculated as:

$$\begin{aligned} P_{ABS} &= P_{IN} - P_{OUT} \\ \frac{P_{ABS}}{P_{IN}} &= 1 - \exp(-N_0 \cdot \sigma_{ab}(\lambda) \cdot t) \end{aligned} \tag{3.27}$$

In the plant, a mirror behind the gain medium is used for coupling back the unabsorbed portion of the pump power thus increasing the efficiency of absorption. In other words, the light that is not absorbed in the first pass are reflected back and fed to the crystal (Figure 3.15 (b)).

Then, the absorbed pump power in the gain medium by taking into account of effective absorption cross section is:

$$\begin{aligned} P_{REF} &= P_{IN} \cdot \exp(-N_0 \cdot \sigma_{ab,eff}(\lambda) \cdot t) \\ P_{OUT} &= P_{REF} \cdot \exp(-N_0 \cdot \sigma_{ab,eff}(\lambda) \cdot t) \\ P_{ABS} &= P_{IN} - P_{OUT} = P_{IN} \cdot \left[1 - \exp(-2N_0 \cdot \sigma_{ab,eff}(\lambda) \cdot t)\right] \end{aligned} \tag{3.28}$$

The resulting gain medium temperature equation:

$$\frac{dT_{act}}{dt} = \frac{1}{C_{s2}}\frac{T_{amb} - T_{act}}{R_{HA2}} + \frac{1}{C_{s2}} \cdot \gamma \cdot \left[\sum_{i=1}^{5} \sigma_{se,i}(T_d) \cdot (I - I_{th,i})(1 - e^{-2 \cdot \sigma_{ab,eff} \cdot (\lambda_p) \cdot N_0 \cdot t}) \right] \tag{3.29}$$

where C_{S2} and R_{HA2} were calculated by using same approach in Section 3.1.1.

3.1.2.6 Output

The output energy of the released pulse is found as:

$$y[k] = E_{OUT}[k] = h\nu_L V_{act} \cdot \int_{t_{start}}^{t_{end}} \phi \cdot dt \tag{3.30}$$

Here, $h\nu_L$ is the energy of a single laser photon, V_{act} is the volume of the gain medium. Multiplying V_{act} with the integral of the photon density, the number of laser photons is calculated.

Every laser generation sequence starts with the LDA pump and ends with the release of laser pulse. The t_{end} in the output equation is used for just visualization of the integral time limit and k represents index of a laser pulse generation sequence. Timing diagram is drawn in Figure 3.16.

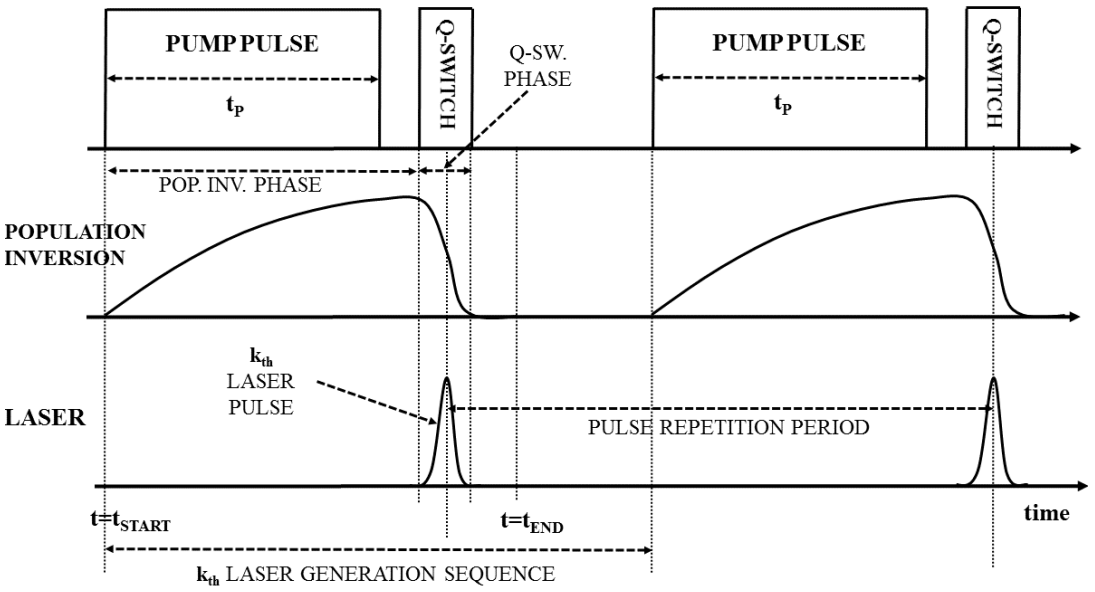

Figure 3.16: Timing Diagram

3.2 Model: System ID

The aim in this section is to find a simpler relation between the drive current and output energy by using measurements which was obtained in various ambient conditions and different drive current values.

Input of the system is electrical current supplied to the LDAs, u[k], and output is the laser pulse energy, y[k], (Figure 3.17).

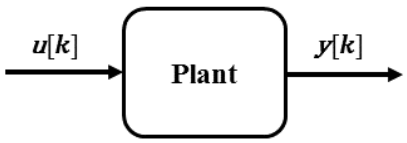

Figure 3.17: The Single Input Single Output (SISO) Plant

Conversion of the electrical input power (P_{in}) delivered to the pumping LDAs; then to the laser output power in a solid state laser source can be characterized by two parameters; the threshold input power P_{TH} and a slope efficiency σ_S (Equation 3.31).

$$P_{OUT} = \sigma_S(P_{in} - P_{TH}) \tag{3.31}$$

Below the threshold, gain is smaller than losses and no laser emission can be extracted from plant. When P_{in} exceeds the threshold, the output power increases linearly up to a saturation point. Our system is designed to operate in the linear regime therefore Equation 3.31 holds.

The input supplied to the plant goes through several processes throughout to the extraction of laser output. As losses of these processes increase, the threshold input power increases and the slope efficiency decreases. In the Figure 3.18, effect of losses on the slope efficiency and the threshold input power is illustrated.

Both σ_S and P_{TH} depend on the efficiencies of these processes. The slope efficiency and threshold input power are given as [11]:

$$\sigma_S \approx \frac{T}{T+\delta}\eta, \tag{3.32}$$

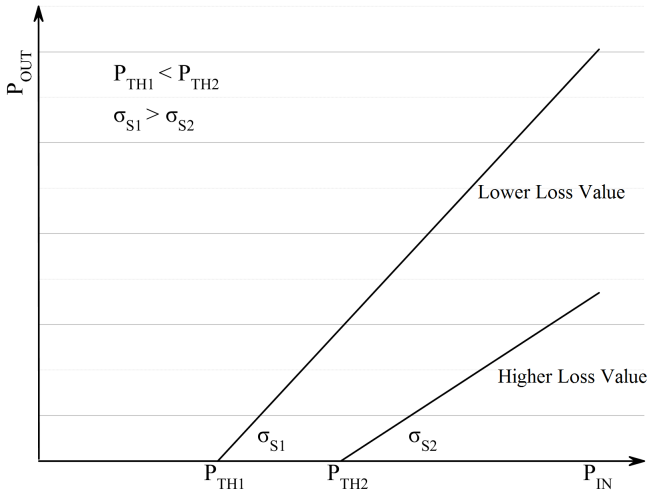

Figure 3.18: Laser Output P_{OUT} versus Input Power P_{IN} in Solid State Lasers: Illustration of Increasing Loss [11]

$$P_{TH} \approx \frac{T+\delta}{2} \frac{A_p\, h\nu_L}{\eta\, \sigma\, \tau_f}, \tag{3.33}$$

where T is mirror transmittance of the resonator, δ is the resonator losses, η is the overall efficiency of the processes, A_p is the cross section of the pumped area, h is the Plank's constant, ν_L is the output laser frequency, σ is the stimulated emission cross section and τ_f is fluorescence time of the gain material.

Next, these processes and the system parameters that are necessary for a numerical model will be investigated.

3.2.1 Conversion Processes of Electrical Power Input to the Optical Laser Output

The conversion processes is rigorously described in Chapter 3 of [11] by four transfer mechanisms. It starts with the transformation of electrical power to the useful pump radiation for gain medium with pump source (LDA) efficiency η_p. Then, the pump radiation is coupled to the gain medium with radiation transfer efficiency η_t. This coupled pump radiation is absorbed by the gain medium and it excites the gain medium to the upper state with absorption efficiency, η_a, and upper state efficiencies

consisting quantum, η_Q, and quantum defect efficiencies,η_S. Lastly, the upper state energy is converted to the laser output with beam overlap and extraction efficiencies, η_B and η_E, respectively. The transfer mechanisms and corresponding efficiencies are illustrated in Figure 3.19.

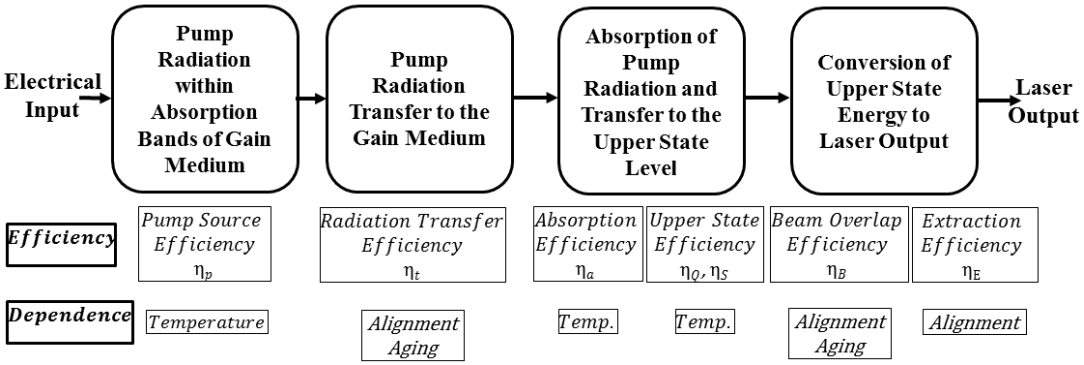

Figure 3.19: Energy Flow in Solid State Lasers [11]

3.2.1.1 Conversion of Electrical Input Supplied to LDAs to Pump Radiation within Absorption Bands of Gain Medium

As the first process, the electrical input is converted to the optical power by the pumping LDAs with pump source efficiency. The pump source efficiency η_p can be expressed as:

$$\eta_p = P_\lambda / P_{in}, \tag{3.34}$$

where P_λ is the pump radiation within absorption bands of gain medium and P_{in} is the electrical input power to the system. This efficiency accounts for power conversion characteristics of the pumping LDAs.

An LDA is a laser source itself. Its efficiency depends on aging and operating temperature as covered in Section 2.2. While aging introduces long term degradation, the operating temperature has influence on the efficiency directly. The efficiency of LDA varies between 40% to 64% over the military temperature range.

Aging effects can not be predetermined for any of the system components because it requires monitoring and recording of operating conditions such as vibration, shock and temperature that may speed up aging. Even the operating conditions are recorded, a component may age faster than another from different production batch. Therefore,

accurate modeling of output power degradation of LDAs due to aging is not viable.

3.2.1.2 Pump Radiation Transfer to the Gain Medium

The pumping laser emitted by LDAs is transferred to the gain medium via coupling optics forming pump chamber [26]. The quality of this process is evaluated by radiation transfer efficiency, η_t, that is:

$$P_e = \eta_t * P_\lambda, \tag{3.35}$$

where P_e is the fraction of useful pump radiation injected to the gain medium. The radiation transfer efficiency represents reflection and spill over losses of the pump chamber. For the plant, spill over losses are neglected because the pump LDAs are placed very close to the gain medium. However, the reflection losses may degrade the performance of this process. In the pump chamber, the gain medium and the coupling optics have anti-reflection coatings for wavelength spectrum of the pump radiation. These coatings may age and worsen the power transfer.

3.2.1.3 Absorption of Pump Radiation and Transfer to the Upper State Level

This process are examined in two steps. Firstly, the pump radiation transferred by the pumping LDAs is absorbed by the pump bands of the gain medium with the absorption efficiency, η_a

$$\eta_a = P_a/P_e. \tag{3.36}$$

The P_a is absorbed power by the gain medium. For diode pumped solid state lasers η_a is approximated as [11]:

$$\eta_a = 1 - exp(-\alpha_0 * t), \tag{3.37}$$

where α_0 is the absorption coefficient of the gain medium and t is the thickness of the

gain medium. The latter is constant in the plant but the former changes with temperature because of the absorption spectrum of the gain medium and spectral properties of the pumping LDAs.

Secondly, the absorbed power in the pump bands is transferred to the upper state laser level with an efficiency consisting two definitions which are quantum defect, η_S, and quantum, η_Q, efficiencies. The quantum defect efficiency, which is also known as Stokes factor, is the ratio of output laser photon energy to the pump photon energy:

$$\eta_S = (h * \nu_L)/(h * \nu_P) = \lambda_P/\lambda_L, \tag{3.38}$$

where λ_P is the pump laser wavelength (808 nm) and λ_L output laser wavelength (1064 nm). For the plant, it is 0.76 at room conditions.

The quantum efficiency η_Q is given as the ratio of the number of photons in the laser emission to the number of pump photons and it is a constant and 0.9 for diode pumped solid state Nd:YAG laser [11].

3.2.1.4 Conversion of Upper State Energy to Laser Output

The last process is the extraction of stored energy in the upper state level from the plant. This process is evaluated by beam overlap, η_B, and extraction, η_E, efficiencies.

To begin with, the beam overlap efficiency is a metric of how well the resonator modes coincide with the gain distribution. Secondly, the extraction efficiency for a Q-switched laser source is calculated as [11]:

$$\eta_E = \eta_{St}\eta_{ASE}\eta_{EQ}, \tag{3.39}$$

where η_{St} is storage efficiency, η_{ASE} represents for the amplified spontaneous emission and parasitic oscillation losses of the stored energy and η_{EQ} is the Q-switch extraction efficiency.

The extraction is attained by Q-switching. Energy in the upper state level may leak till

switching of quality factor of the resonator. The storage efficiency covers the leakage and it is given as:

$$\eta_{St} = \frac{1 - \exp(-t_P/\tau_f)}{t_P/\tau_f}, \tag{3.40}$$

where t_P is the pump duration and τ_f is the fluorescence life time.

The spontaneous emission after amplification in the gain medium may also cause decrease in the stored energy. This losses are included in the model by the η_{ASE}.

The extraction efficiency of the Q-switch process is calculated as [31]:

$$\eta_{EQ} = 1 - \frac{1 + \ln(\frac{2g_0 l}{L})}{\frac{2g_0 l}{L}}, \tag{3.41}$$

where g_0 is small signal gain, l is length of the gain medium, L is resonator round trip loss.

Material properties of the gain medium and pump power affect the small signal gain. By increasing the pump power, the small signal gain can be increased till the gain saturation.

3.2.2 Adaption of the Plant to Parameters of Conversion Processes

The goal of the adaption is to identify the slope efficiency and the threshold power for a numerical model as given in Equation 3.31. The model should express the relation between input pump current and output energy.

The Equation 3.31 can be modified for energy transfer due to pulsed operation:

$$E_{out} = \sigma_{S,r}(E_p - E_{th}), \tag{3.42}$$

where E_{out}, E_p, $E_{th,r}$ are the output, pump and resonator threshold energies, respectively. To reach the electrical current-energy relation, firstly, the pump energy is expressed as [32]:

$$E_p = \bar{\eta_P}(I_{in} - I_{th,p}) \tag{3.43}$$

The $\bar{\eta_P}$ term contains the pump source efficiency and current to energy conversion factor. The $I_{th,p}$ is the threshold current of the pump assembly. Substituting Equation 3.43 into Equation 3.42:

$$E_{out} = \sigma_{S,r}[\bar{\eta_P}(I_{in} - I_{th,p}) - E_{th,r}] \tag{3.44}$$

The threshold energy of resonator is provided by pump energy which increases linearly with the pump current. Because of this linearity, both threshold expressions can be combined into single threshold current, I_{th}. Moreover, the efficiency expressions $\bar{\eta_P}$ and the $\sigma_{S,r}$ are combined and overall slope efficiency is represented as σ_S. Then, the equation becomes:

$$E_{out} = \sigma_S(I_{in} - I_{th}) \tag{3.45}$$

where the σ_S in Equation 3.32 is adapted as:

$$\sigma_S = K\frac{T}{T+\delta}\eta_P\eta_t\eta_a\eta_Q\eta_S\eta_B\eta_E \tag{3.46}$$

with a proportionality constant K.

3.2.2.1 Exploratory of the Adapted Parameters

In this part, model parameters will be studied for the plant. From equation Equation 3.45, there are two parameters to be identified:

- Slope Efficiency, σ_S,
- Threshold Current, I_{th}.

Firstly, the thermal and aging effects on slope efficiency are put under the scope. For complete analysis, ten parameters given in Equation 3.46 are examined below:

1. **Pump Source Efficiency, η_P:** Pump LDAs of the plant has 52% efficiency at room conditions. However, it depends on operating temperature as mentioned in Section 2.2.1.1. The efficiency is expected to stay in 52$\pm$12%. With aging, center value of the efficiency may also decrease. All these effects can not be directly modeled.

2. **Transfer Efficiency, η_t:** It is close to one due to architecture of pump cavity. Aging may degrade performance of the transfer slowly.

3. **Absorption Efficiency, η_a:** As mentioned in Section 2.2.1.1, peak emission wavelength of pump LDAs changes from 794 to 815 nm for the operational temperature range. The absorption coefficient of Nd:YAG alters between 1 to 9 cm^{-1}. The effect of this difference is suppressed by the pump cavity design. However, the absorption efficiency still changes $\pm$14% with temperature.

4. **Quantum Efficiency, η_Q:** It is 0.9 [11] and constant due to material characteristics.

5. **Quantum Defect (Stoke' s) Efficiency, η_S:** It is affected by temperature because of the wavelength shift of the pump emission. Its nominal value is 76 % and varies $\pm$2%.

6. **Beam Overlap Efficiency, η_B:** This efficiency is constant based on the mechanical design and it is close to one. It is also independent of temperature and aging effects.

7. **Extraction Efficiency, η_E:** It is constant and 0.65. The value is confirmed theoretically and experimentally.

8. **Resonator Mirror Transmission and Resonator Losses, T and δ:** The mirror transmission is constant and close to 1 but it degrades by aging. And the resonator losses alters with diffraction losses and the effects mentioned in Section 2.2. The resonator mirror transmission and resonator losses may introduce 0.6 factor together depending on the operating condition.

When all margins are considered, the slope efficiency may change within $\pm$30 % with respect to its nominal value. Moreover, this change is caused only by the temperature effects. The aging affects can not be taken into account as an analytical parameter.

The threshold current is composed by two components which are the threshold currents of pumping LDAs and the resonator itself. The former increases with temperature. The behavior is measured and plotted in Figure 3.20. The latter is proportional to P_{th} and $1/\sigma_S$ whose expressions are given in Equation 3.32 and 3.33, respectively. The total threshold current can be accepted as 50 A at nominal working conditions.

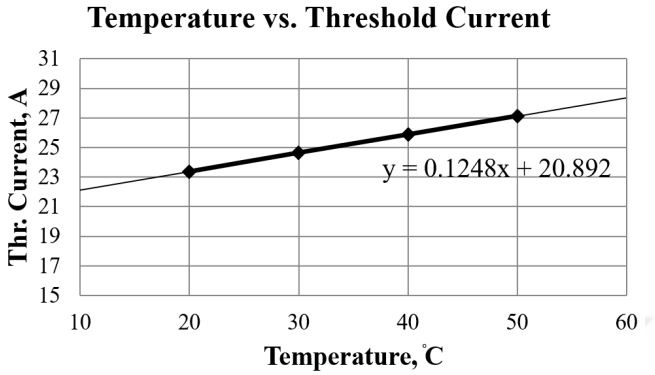

Figure 3.20: Temperature vs. Threshold Current

The general efficiency term η can be considered to alter between $\pm$ 30 and the stimulated emission cross section σ is approximately is in $\pm$ 7% margin for its nominal value.

3.2.2.2 An Attempt by Using Autoregressive Time Series Model

Variation in the threshold current can be reflected onto slope efficiency because of linearity. Thus, the threshold current in the model is assumed to be constant and its nominal value (50 A) is used. In this case the model becomes:

$$E_{out}[k] = \sigma_S[k](I_{in}[k] - 50) \tag{3.47}$$

where $I_{in}[k]$, $\sigma_S[k]$ and $E_{out}[k]$ are the input current, slope efficiency and output energy at pulse kth.

For system identification, 120000 laser pulses were measured while the plant were facing different operating conditions. In the test, operating temperature, PRF and driving current were varied to obtain rich data about system dynamics.

As explained in Section 2.2, the most dominant instabilities on output energy are caused by thermal effects. The temperature of a material does not change instantly in nature. Therefore, to estimate the next slope efficiency, Autoregressive (AR) time series models with 2., 3. and 4. degrees were used:

$$\begin{aligned}
\sigma_S[k] &= a_1\sigma_S[k-1] + a_2\sigma_S[k-2] \\
\sigma_S[k] &= b_1\sigma_S[k-1] + b_2\sigma_S[k-2] + b_3\sigma_S[k-3] \\
\sigma_S[k] &= c_1\sigma_S[k-1] + c_2\sigma_S[k-2] + c_3\sigma_S[k-3] + c_4\sigma_S[k-4]
\end{aligned} \tag{3.48}$$

By using Least Squares Estimation, results below were found:

- a_1 = 0.5383 , a_2 = 0.4616
- b_1 = 0.4144 , b_2 = 0.3172 , b_3 = 0.2684
- c_1 = 0.3676 , c_2 = 0.2619 , c_3 = 0.1961 , c_4 = 0.1744

As merit of the estimation, mean and standard deviation of residuals are given in Table 3.2.

Table3.2: Least Squares Estimation Results

Model Degree	Mean of Residuals (mJ)	Standard Deviation of Residuals (mJ)
2.	0.0019	0.6956
3.	0.0013	0.6701
4.	0.0011	0.6598

The results show that even the simplest form of AR time series can predict the slope efficiency as well as the output energy with reasonable error. This model is much simpler as it was not required lots of experiments, calculations and modeling effort.

In Figure 3.21, 2. degree AR time series model response is plotted with calibrated reference energy meter measurement for comparison. The model tracks the measurement closely. The AR time series model with its coefficients estimated by Least Squares can also be used for controller modeling.

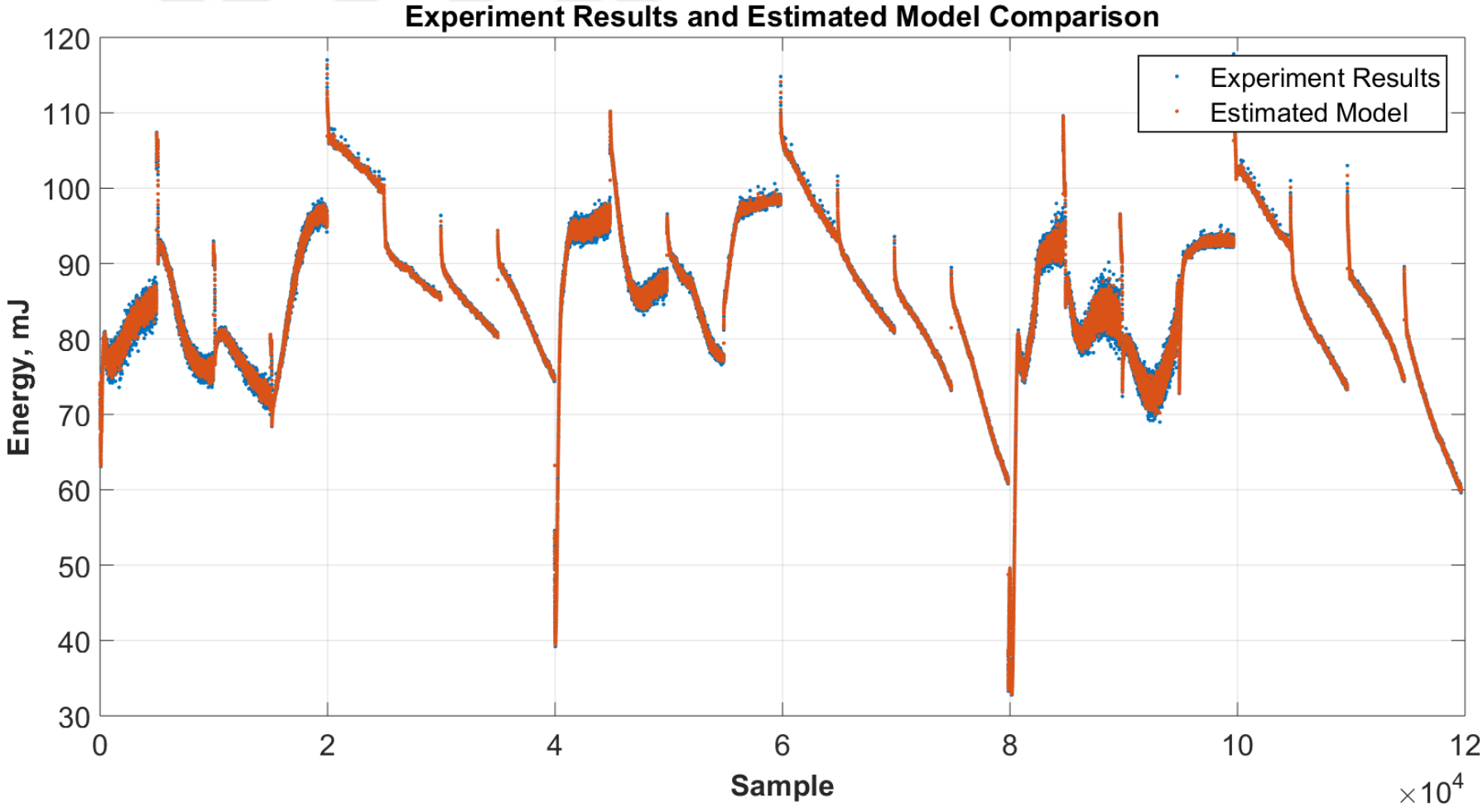

Figure 3.21: Measurement and 2. Degree Model Response

CHAPTER 4

LASER ENERGY MEASUREMENT

External monitoring of output power/energy is the most common test for performance of a laser as it represents directly its sufficiency to carry out a specific mission. This parameter is checked, recorded and compared at almost every step of designing, manufacturing and environmental testing of a laser source. For this purposes, commercial laser power/energy meters are used. A power/energy meter and a typical measurement sensors of Coherent, Inc. are illustrated as examples in Figure 4.1 and 4.2.

Figure 4.1: Laser Power / Energy Meter [3]

Figure 4.2: Sensors for Power and Energy Measurements [2]

Power (in Watts) are meaningful for continuously operated lasers whereas energy (in Joules) describes pulsed laser.

There are three sensor types used for power/energy measurement; thermopile, pyroelectric and photodiode. The thermopile and pyroelectric sensors measure laser power/energy by using thermal effects caused by infrared radiation in contrast photodi-

odes sense incident light on its active area and convert it to current that varies with the incident signal. The sensor choice of an application depends on the properties of laser.

These power/energy meters are designed as laboratory equipments to operate at room temperature. They can not be integrated to an airborne application due to their enormous dimensions and susceptibility to operating temperature. Moreover, these meters use the whole portion of the laser beam. For our application, the laser must radiate to the target without interruption. As a result, this project requires a built-in laser energy meter working concurrently with the laser source.

In this chapter, the designed and manufactured internal laser energy measurement system including sampling method of outgoing laser pulses and processing electronics will be explained.

4.1 Design Description

The measurement system requires 3 main design steps: selection of sensor, design of electronics and design of optical unit.

4.1.1 Sensor Choice

For sensing the infrared laser radiation, photodiode is selected among other sensors because of being low cost, reliable and ease of use. There are two types of photodiodes, PIN and avalanche (APD). The latter is used for very low level signal detection due to being more sensitive than PIN. The APD photodiodes are more difficult to use than PIN ones because they require tunning of bias voltages with respect to temperature. Furthermore, they are generally more expensive than PIN ones.

The commercial PIN photodiodes are made of Ge, Si, GaAs and InGaAs. These choices are evaluated by comparing their spectra, noise, speed and temperature characteristics. All of them sense 1064 nm radiation (Figure 4.3). However, Si and Ge photodiodes either shows temperature dependent spectral characteristics or expensive and hard to use. Therefore, standard (std) InGaAs-PIN type is chosen. Properties of the

selected photodiode are summarized in Table 4.1.

Table4.1: Photodiode Parameters: C30619, [1]

Parameter	Value
Type	InGaAs-PIN
Shape	Circular
Active Area	0.2 mm^2
Operating Voltage	5 V
Responsivity @ 1064 nm	0.78 A/W
Shunt Resistance	250 $M\Omega$
Dark Current(Max)	20 nA
Spectral Noise Current(Max)	0.1 $pA/\sqrt{Hz}$
Capacitance	10 pF
Bandwidth	350 MHz
Maximum Photo-current	100 mA

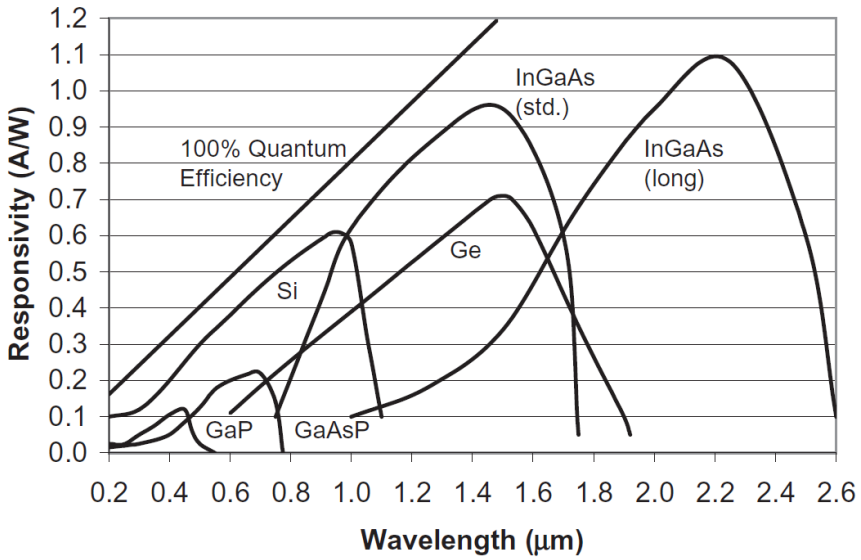

Figure 4.3: Responsivity Curves of Photodiodes Manufactured by Using Different Semiconductor Materials [12].

4.1.2 Electronic Architecture

The energy of a laser pulse is the integral of optical power of the pulse over time. This optical power is converted to voltage waveform (V(t)) which is proportional to intensity of the pulse by using a photodiode cascaded to a trans-impedance amplifier (TIA). The measured V(t) of our system is illustrated in Figure 4.4.

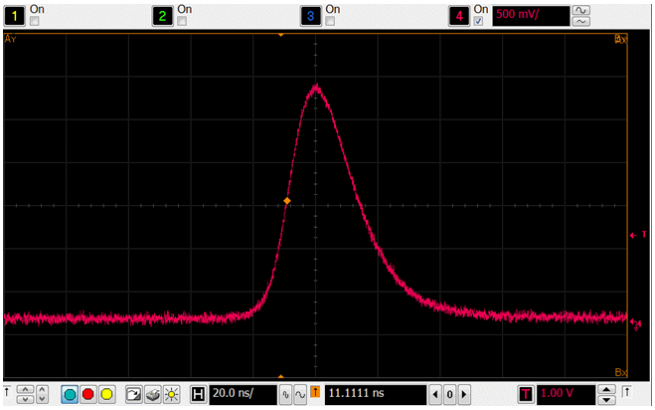

Figure 4.4: Laser Pulse Monitored with a Photodiode, Pulse Width = 24 nsec (FWHM)

A relation between the voltage waveform and pulse energy is given in Equation 4.1 [33]:

$$\int_{t_{start}}^{t_{end}} V(t)dt = kE, \tag{4.1}$$

where, E is the pulse energy and k is calibration constant. t_{start}, t_{end} indicate the pulse time envelope. This can be called as integration method.

In addition, the pulse energy can be found by recording the peak value of the photodiode response. This is because the pulse width of the measurand is constant for the system under investigation and as the pulse energy increases, the peak value of $V(t)$ increases linearly like the integration of it. This is called as peak hold method. The method is experimentally verified and results are plotted in Figure 4.5.

Selection of Measurement Method:

The photodiode and processing circuitry is noisy and there exists dark current and background illumination causing an offset on the sensor output. The integration will add up this offset and noise. To decrease it, a low noise comparator can be designed for locating the start point of the pulse and the integration can be triggered with the start. Even so, the noise content during the pulse will also be add up to the output.

The peak hold method may suffer from leakage but the MCU in the present study is fast compared to the leakage which provides instantaneous reading of peak value.

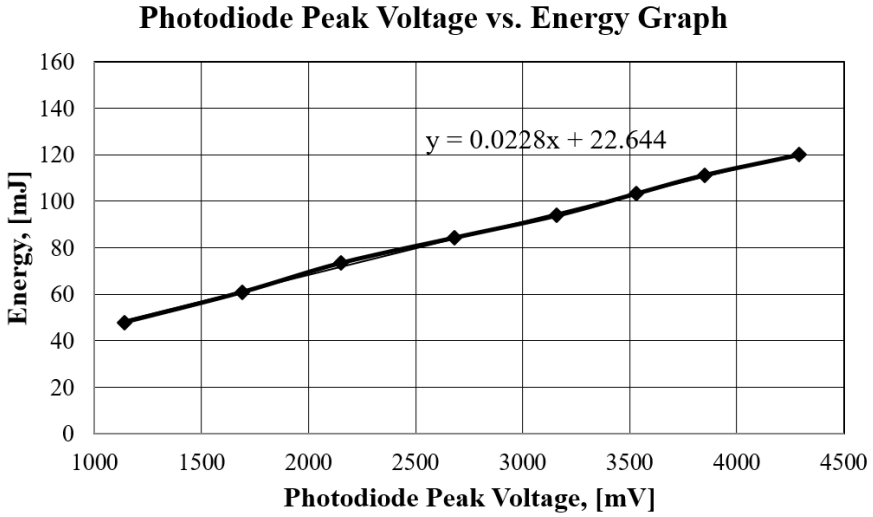

Figure 4.5: Output Energy vs. Photodiode Peak Voltage

Furthermore, to eliminate the noisy content, the peak value is read several times consecutively and averaged. Thus, instead of integration, capturing the peak voltage of photodiode signal is chosen for built-in energy meter.

In short, the design should take proper sample from each laser pulse, couple it to the photodiode and process its peak voltage.

The electronic architecture of the measurement system is presented in Figure 4.6. Response of the photodiode is coupled to the amplification and filtering circuits. After that, the process continues in MCU and analog peak hold circuit. The amplified and filtered electrical signal is compared to an analog level in interrupt controller of MCU. When the signal is larger than the interrupt level, the timer is triggered and it counts till a constant and predefined duration required for stabilization of analog circuits. As the timer finishes counting, a timer generated interrupt triggers the built-in 12 bit ADC to read the voltage output of the peak hold circuitry. Lastly, the ADC reading is scaled by calibration constant and the energy value is found.

4.1.3 Optical Design

For proper measurement of laser pulse energy, there are various optical issues to be considered. To begin with, the output laser pulse should be sampled without distortion. For this purpose a thin parallel plate is placed in the output path forming a sample

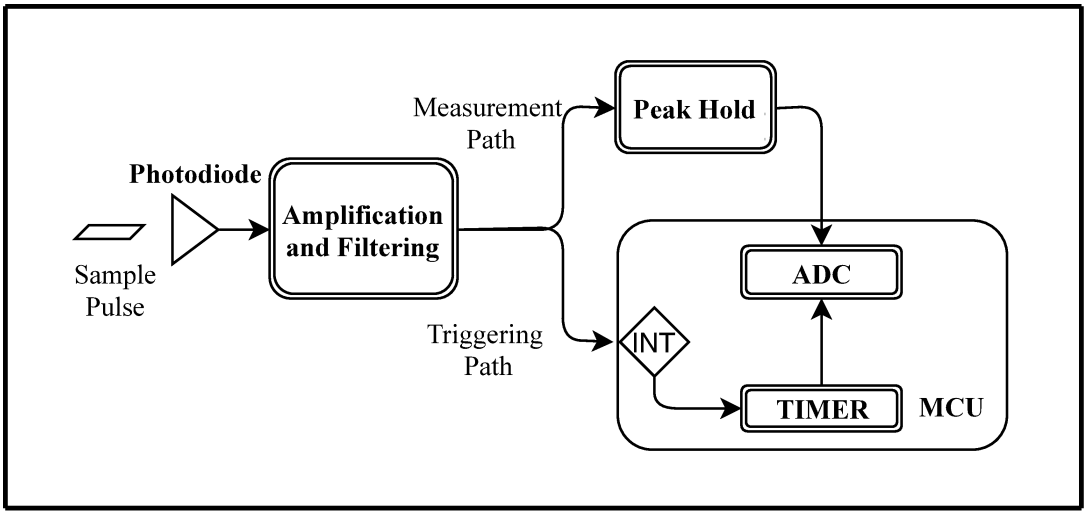

Figure 4.6: Electronic Structure of the Measurement System

of 4 % from outgoing laser pulse from plant.

While measuring the laser pulse, there may exist daylight exposure or another light source depending on the platform that the plant is integrated. To cancel out any possible background illumination, bandpass filter around 1064 nm is added to the design.

Another issue is that the peak power of laser pulses emitted from the plant are enormously high for sensitive devices such as photodiode. For output energy control, the system should measure between 20 to 150 mJ laser pulses. The corresponding peak powers which the energy meter must read:

$$P_{peak,min} = \frac{20.10^{-}3}{20.10^{-}9} = 1MW \tag{4.2}$$

$$P_{peak,max} = \frac{150.10^{-}3}{20.10^{-}9} = 7.5MW \tag{4.3}$$

From Table 4.1, the responsivity of photodiode is 0.78 A/W at 1064 nm illumination and maximum photo-current is given as 100 mA. An optical attenuation is needed so that this current is scaled down to guarantee linearity and to create margin for optical density (OD) filter. The OD filter value can be found as:

$$OD = -\log \frac{P_{out}}{P_{in}} \tag{4.4}$$

The design is started with assumption of 6.6 mA max photo-current. Then, maximum power incident to the photodiode is found as $6.6*10^{-3}/0.78 = 8.46\,mW$. This means that after 4% sampling, 7.5 MW peak pulse power should be attenuated to 8.46 mW. Therefore:

$$-\,log(\frac{8.46 * 10^{-3}}{0.04 * 7.5 * 10^{6}}) \approx 7.55 \tag{4.5}$$

OD attenuation should be used.

After adjusting the level, signal should be focused due to the small active area of the photodiode. The signal size is the emission area of the active medium which is 30 mm^2. In contrast, the photodiode has active area of 0.2 mm^2. To collect all sample pulse, bi-convex lens is added to the design.

Optical components of the sampling system is shown in Figure 4.7 and Figure 4.8 (a). Summary of functional descriptions of these components are listed below:

- Parallel Plate (1): It is used for extraction 4% of the output pulse.
- Focusing Lens (2): The filtered and attenuated sample pulse is focused to active area of the senor by using a 1064 nm AR coated biconvex lens.
- Band Pass Filter (3): It transmits only 1064$\pm$20 nm light and thus optical background noise is eliminated.
- OD Filter (4): To avoid saturation of sensor due to the high peak power of the pulse, neutral density filter with predetermined attenuation is utilized in the optical path.
- Sensor (5): An InGaAs photodiode is used for sensing the sampled pulse because of its spectral and temperature characteristics.

Placement of the measurement system is illustrated in Figure 4.8 (b). The parallel plate is replaced in the laser path then the sampled pulse is attenuated. Later, the pulse is fed to the photodiode mounted on the printed circuit board.

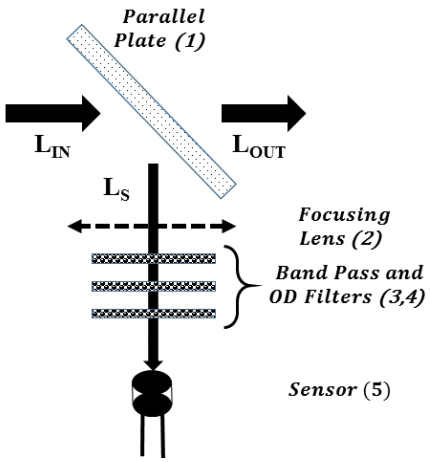

Figure 4.7: Energy Sampling Block Diagram

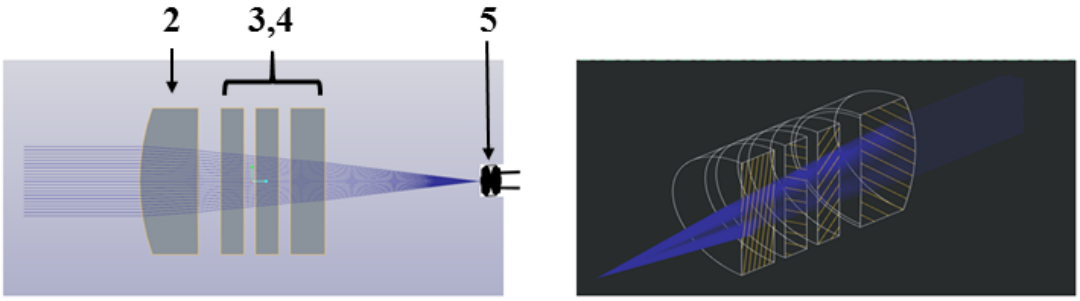

(a) ZEMAX Model of the Sampling System

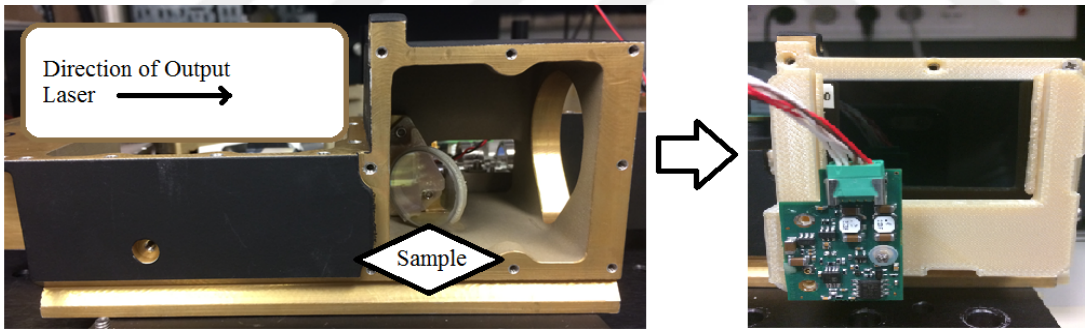

(b) Placement of Optical Sampling System

Figure 4.8: Measurement System

4.2 Test Results

This system is tested under various operating conditions. While testing, PRF and pump current are altered as well as the operating temperature for simulating the working scenarios. The test setup is illustrated in Figure 4.9.

The tests are conducted for 10, 14 and 20 Hz repetition frequencies with 100, 110,

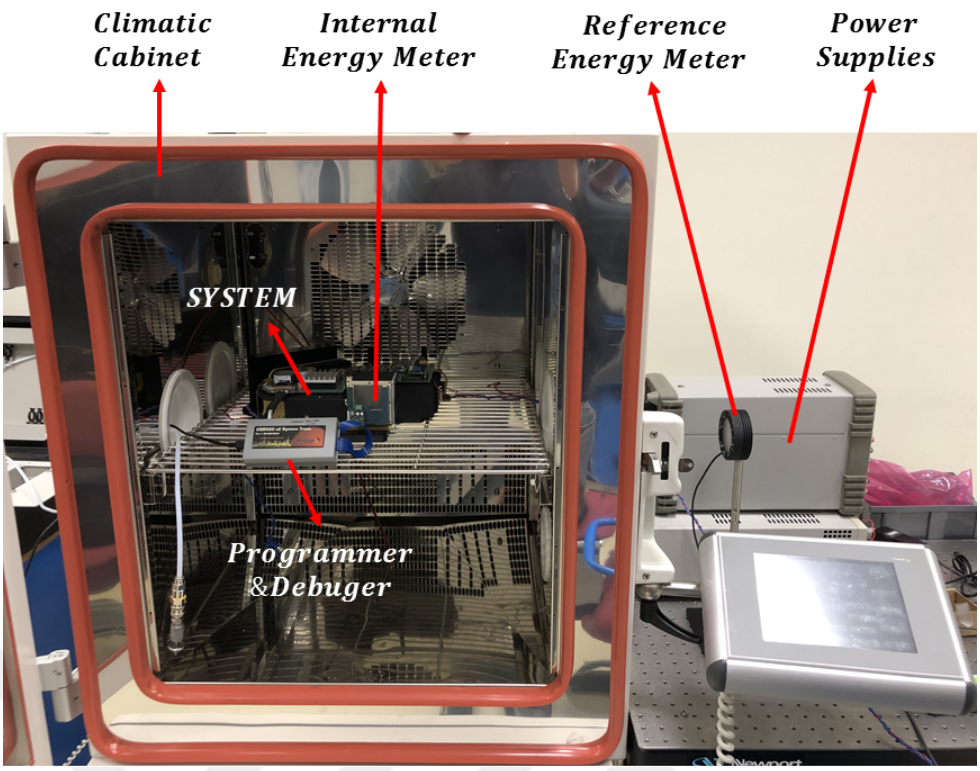

Figure 4.9: Energy Meter Test Setup

120 A driving currents at -20, 0, 25, 50 °C operating temperatures.

Results for 10 Hz operation at room temperature with 100 A drive current are shown in Figure 4.10. In Figure 4.10(a), the reference with the internal measurement and in Figure 4.10(b), difference between the reference and internal measurement are given. Mean and absolute maximum of the residuals are found as 0.35 mj and 4.57 mJ, respectively.

Other results are tabulated in Table 4.2. The mean (μ) and absolute maximum of the difference (γ) are found as:

$$\begin{aligned} \mu &= \frac{1}{N} \cdot \sum_{k=1}^{N} (\hat{r}_k - \hat{i}_k) \\ \gamma &= \max_{\forall k} \mid \hat{r}_k - \hat{i}_k \mid \end{aligned} \tag{4.6}$$

where k and N is index and number of measurements and $\hat{r}_k$, $\hat{i}_k$ are kth reference and the internal measurement, respectively. For each test, 500 measurements were taken

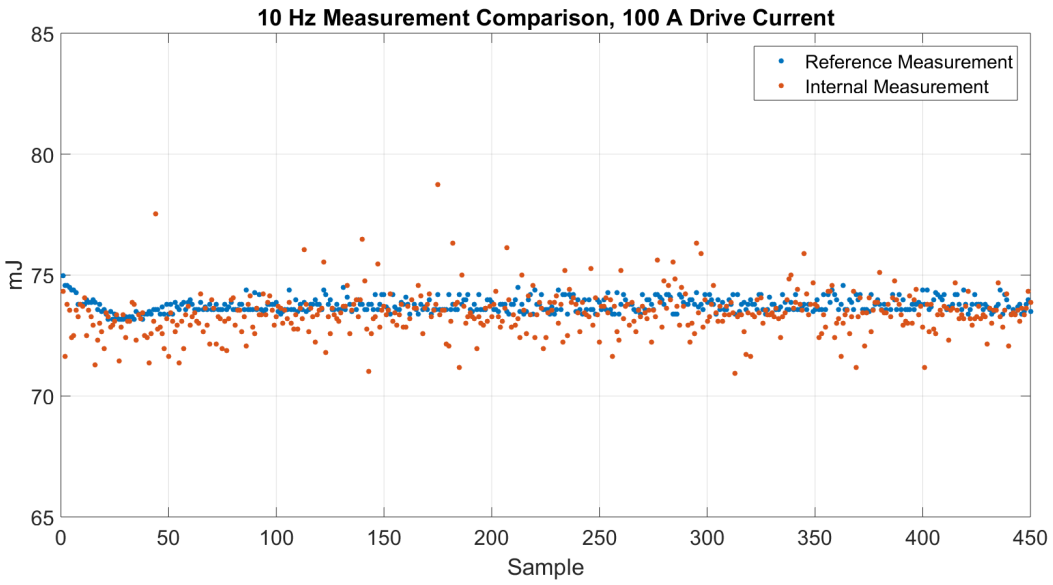

(a) Measurements at 10 Hz: Calibrated Energy Meter and Built in Energy Meter Comparison, 100 A and Room Temperature

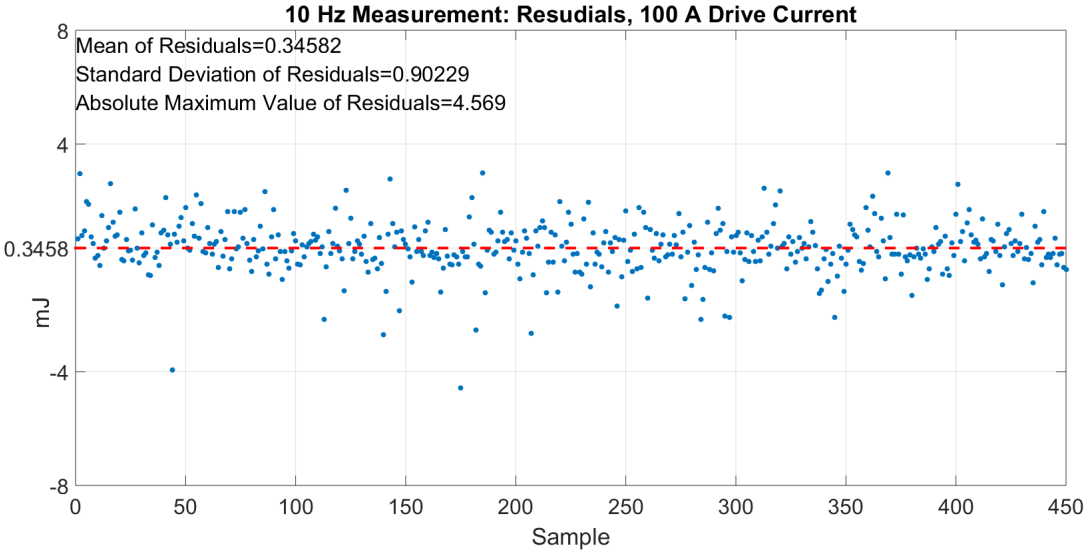

(b) Residulas of Measurements at 10 Hz: Calibrated Energy Meter and Built in Energy Meter Comparison, 100 A and Room Temperature

Figure 4.10: Measurement Results at 10 Hz and Room Temperature

from both the reference energy meter which located outside of the climatic cabinet and internal meter that is exposed to the temperature variations.

Mean of the residuals are close to zero and maximum of absolute values of the residuals are small. Note that, as temperature increased, especially at 50 °C, the mean values increased. This may be caused by dark current of the photodiode and thermal noises of each electronic components which are also affected by temperature. Even

Table4.2: Energy Measurement Test

		10 Hz		14 Hz		20 Hz	
		100 A	120 A	100 A	120 A	100 A	120 A
-20°C	μ	-0.23	0.31	0.24	0.14	0.21	-0.09
	γ	2.41	2.94	4.93	5.61	3.72	6.02
0°C	μ	0.17	0.49	0.71	-0.42	0.11	0.39
	γ	6.01	2.38	3.4	5.28	2.17	6.81
25°C	μ	0.35	0.32	0.12	0.17	-0.04	0.45
	γ	4.57	7.03	4.85	4.12	4.76	5.19
50°C	μ	0.71	0.62	0.83	0.47	0.91	0.5
	γ	5.61	6.07	7.12	4.32	4.81	5.56

though there exits increase in mean values, the results shows that performance of the internal measurement system is sufficient for closed loop architecture.

The calibrated (reference) equipment has its own measurement uncertainty. Its accuracy is affected by both meter electronics and sensor head. This accuracy is calculated as summing in quadrature because the meter and sensor accuracy are independent from each other [2]. Moreover, the meter and sensor accuracies can be found in same manner (Equation 4.7). The corresponding values were extracted from datasheets and included in Table 4.3.

$$
\begin{aligned}
Sensor\ Accuracy &= \sqrt{(Sensor\ Cal.\ Uncertainty)^2 + (Wavelength\ Accuracy)^2} \\
Meter\ Accuracy &= \sqrt{(Display\ Accuracy)^2 + (Calibration\ Uncertainty)^2} \\
Total Accuracy &= \sqrt{(Meter\ Accuracy)^2 + (Sensor\ Accuracy)^2}
\end{aligned}
\tag{4.7}
$$

Table4.3: Calibrated Measurement Equipment Accuracies [2], [3]

Component	Type	Value
Sensor: J-50MB-YAG	Calibration Uncertainty	$\pm$ 2 %
	Wavelength Uncertainty	$\pm$ 2 %
Meter: FIELDMAXII-TOP	Display Accuracy	$\pm$ 2 %
	Calibration Uncertainty	$\pm$ 1 %

The overall measurement uncertainty of calibrated reference equipment is calculated as $\pm$ 3.6 %. The values in Table 4.2 should also be evaluated by considering this uncertainty.

CHAPTER 5

NOISE ANALYSIS

The model dynamics posses both system and measurement noise. The former is originated from alternating characteristics of LDAs and the latter is caused by sensor and processing electronics.

5.1 System Noise

The parameters described in the Section 3.1.1 are neither constant nor deterministic due to the fabrication process and material characteristics of LDAs. Moreover, center emission wavelength and slope efficiency shift with temperature.

Although, these parameters are measurable, it is not practical for each item since it will consume lots of labor and require clean room establishments in serial production line. In other words, measuring these parameters is not cost effective and feasible. Moreover, they may also vary with aging.

Their effects will be compensated by using an output energy controller which is the main aim of this study.

Stable and reliable control algorithm requires a solid model including distributions of LDA's parameters. For this purpose, LDA characterization test setup was established. In the setup, an LDA is mounted on a heat sink with heater and thermistor which are utilized for adjusting the LDA temperature. There is also LDA driver generating current pulses with variable amplitude. By altering the temperature and current, the LDA parameters such as output energy, emission spectrum, voltage are monitored with, energy-meter, spectrometer and oscilloscope (Figure 5.1).

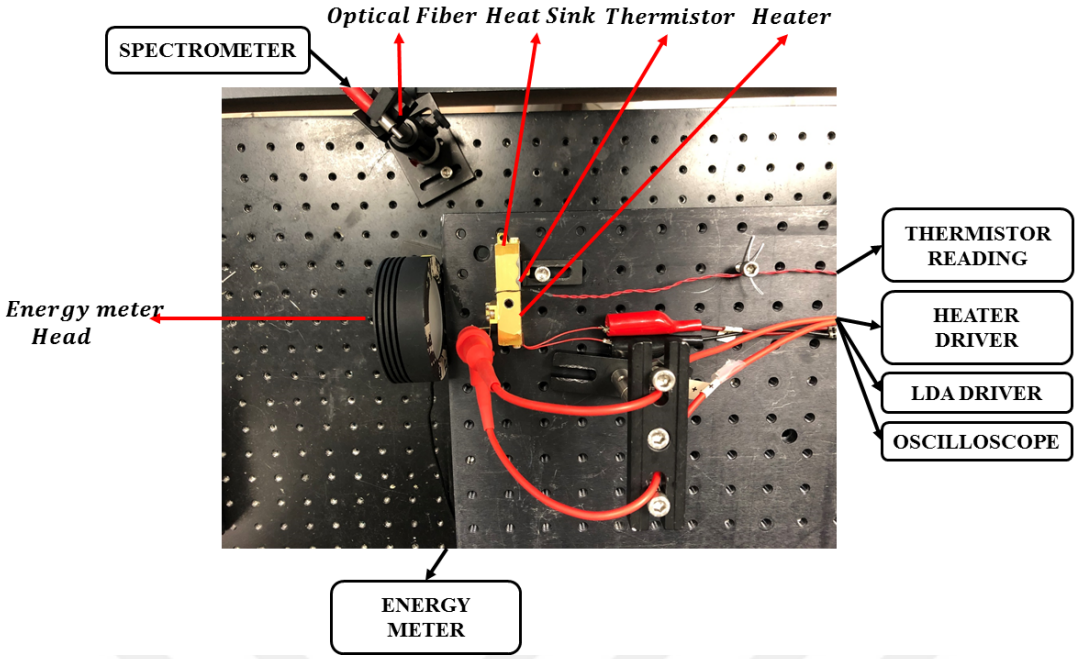

Figure 5.1: LDA Parameter Characterization Setup

5.1.1 Noise Distribution of Center Emission Wavelength

The center emission wavelength of 130 LDA' s at 50 °C is distributed as in Figure 5.2. The histogram is fitted to Gaussian distribution with 807.8 nm mean and 0.61 standard deviation. The discrepancy from Gaussian distribution arose from a large production batch consisting 55 LDAs with very close characteristics.

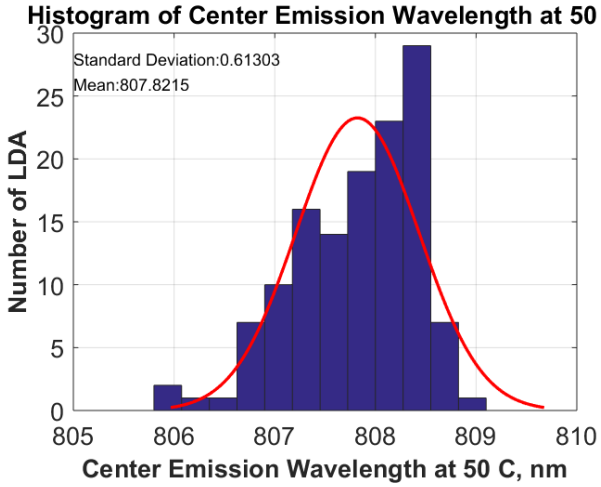

Figure 5.2: Histogram of LDA Center Emission Wavelength at 50 °C

The resulting equation is :

$$\mu_i(T_d) = 0.24 \cdot T_d + 795.8 + \omega_1 \tag{5.1}$$

with $\omega_1 \sim \mathcal{N}(0, 0.61303^2)$.

5.1.2 Slope Efficiency Noise Distribution

The histogram of the slope efficiencies of 130 LDAs at 50 ° C is given in Figure 5.3. The Gaussian distribution resulted in 8.9691 mean and 0.07163 standard deviation.

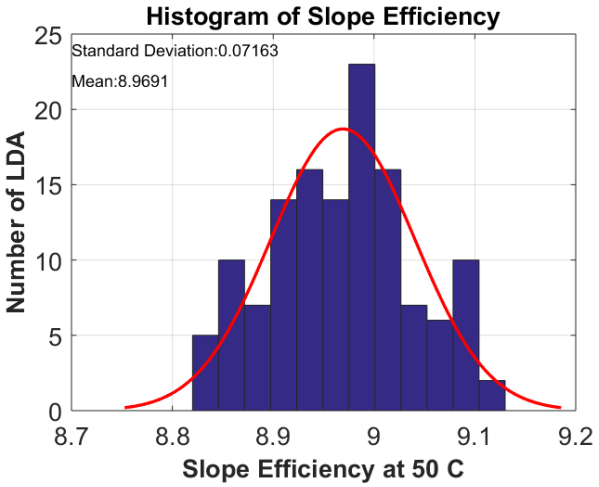

Figure 5.3: Histogram of Slope Efficiency at 50 °C

$$\sigma_{se,i}(T_d) = -0.0274 \cdot T_d + 10.331 + \omega_2 \tag{5.2}$$

with $\omega_2 \sim \mathcal{N}(0, 0.07163^2)$.

5.1.3 Spectral Width Noise Distribution

LDA manufacturers generally use full width half max (FWHM) spectral width. The histogram and distribution fit of 130 LDAs FWHM spectral width is shown in Figure 5.4 which is represented by Gaussian distribution of 1.9123 mean and 0.16235 standard deviation.

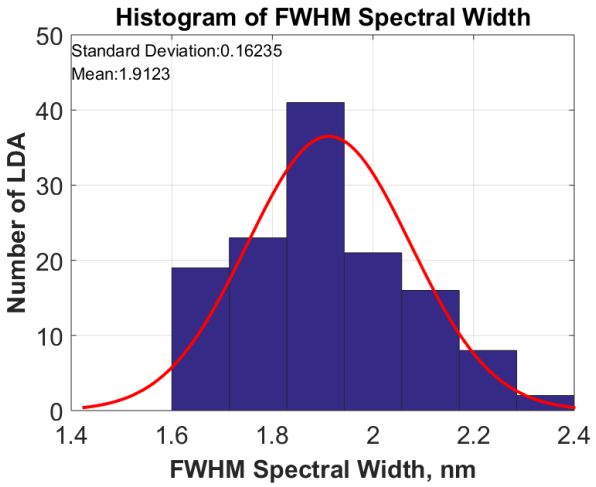

Figure 5.4: Histogram of FWHM Spectral Width

5.1.4 Threshold Current Noise Distribution

LDA threshold current exhibits variations with temperature but these are very small compared to the actual value. Therefore, it is assumed constant with temperature.

Histogram of threshold currents of 130 LDA is shown in Figure 5.5 with fit results of 27.13 mean and 0.807 standard deviation to a Gaussian distribution fit. That is to say:

$$I_{th} \sim \mathcal{N}(27.13, 0.807^2) \tag{5.3}$$

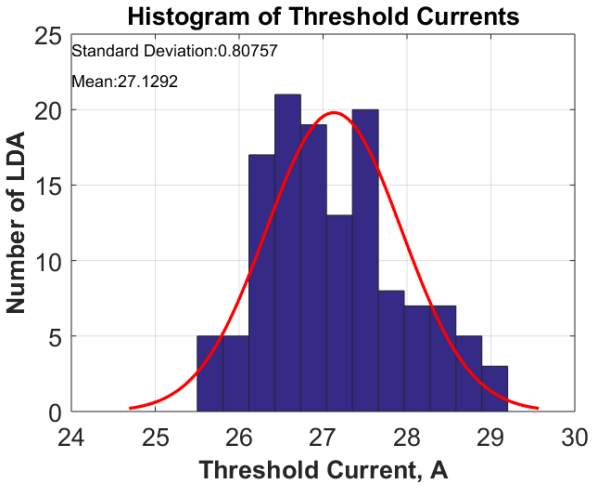

Figure 5.5: Block Diagram

5.2 Measurement Noise

Electrical or optical noise sources of the measurement process may be coupled to the photodiode, trans-impedance amplifier and ADC (Figure 5.6). Contributors of overall measurement noise have been investigated for a complete analysis in this thesis.

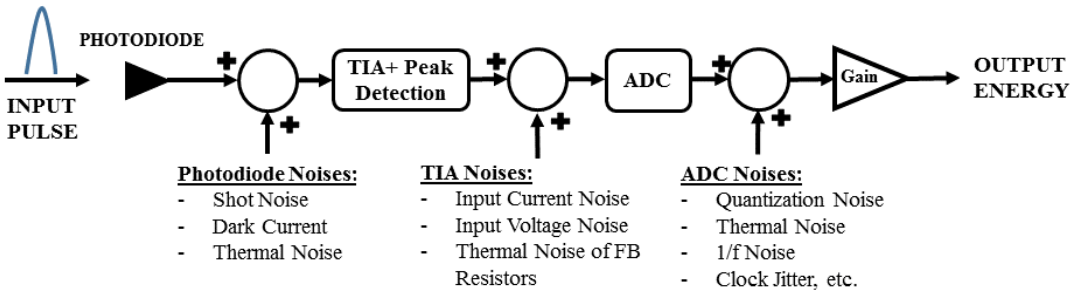

Figure 5.6: Noise Contributors of the Measurement Process

To calculate RMS values of noises, bandwidth of measurement and effective noise should be determined. The former which is defined as 3 dB crossover frequency of the trans-impedance amplifier can be found by using Equation 5.4 and the latter is calculated by using Equation 5.5 [34]:

$$f_{3dB} = \frac{1}{2\pi R_f C_f} = \frac{1}{2\pi \cdot 500 \cdot 6.8 \cdot 10^{-12}} = 46.8\ MHz \tag{5.4}$$

where R_f and C_f are feedback resistance and capacitance of the trans-impedance amplifier (TIA). The corresponding effective noise bandwidth is:

$$ENBW = f_{3dB}.\frac{\pi}{2} = 46.8 \cdot 10^6 \cdot \frac{\pi}{2} = 73.5\ MHz \tag{5.5}$$

5.2.1 Photodiode Noise

Shot (Quantum) Noise: The photo-generated current in the presence of optical excitation is composed of many short pulses caused by discrete electron transfers [35]. The optical excitation creates electron-hole pair in the absorption region which is randomly distributed in time. These electron hole pairs create the short current pulses. Its

behaviour is modeled by Poisson distribution but for large excitations this stochastic noise is represented by a Gaussian distribution (Figure 5.7).

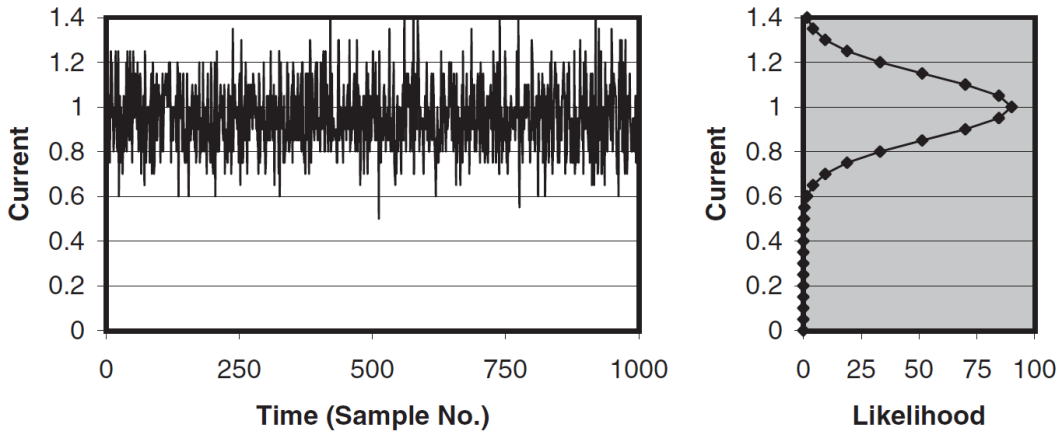

Figure 5.7: Shot Noise Behaviour at Normalized Photo-Current, [12]

The RMS value of the shot noise is:

$$i_s = \sqrt{2qI_pB} \tag{5.6}$$

where q is electron charge, I_p is photo-current and B is the measurement bandwidth. The RMS value of the shot noise increases with the photo-current. For the calculated maximum photo-current, the shot noise is:

$$\sqrt{2 * 1.602 * 10^{-}19 * 6.6 * 10^{-}3 * 47.5 * 10^{6}} = 317\ nA_{RMS} \tag{5.7}$$

Because of being very small compared to the signal value, the maximum current will be used in the analysis.

Dark Current: Photodiodes also generate current when there is no illumination because of the finite shunt resistance. This current is called as dark current and it is maximum $I_{dark} = 20\ nA$ for the selected photodiode [1]. It creates its own shot noise. Therefore, the contribution (RMS) can be calculated as:

$$i_d = \sqrt{2qI_{dark}B} = \sqrt{2 \cdot 1.602 \cdot 10^{-19} \cdot 20 \cdot 10^{-9} \cdot 47.5 \cdot 10^{6}} = 0.552 nA_{RMS} \tag{5.8}$$

Thermal (Johnson) Noise: This noise exists for all resistors operating above absolute

zero temperature and it is caused by internal current fluctuations [12]. Johnson noise generated by shunt resistance of the photodiode is calculated as:

$$i_j = \sqrt{\frac{4kTB}{R_{sh}}} = \sqrt{\frac{4 \cdot 1.381 \cdot 10^{-23} \cdot 323 \cdot 47.5 \cdot 10^6}{10 \cdot 10^6}} = 0.292\, nA_{RMS} \tag{5.9}$$

where k is Boltzmann constant, T is absolute temperature in Kelvin. Note that, this noise is also maximized by using 323 °K and 10 kΩ for the shunt resistance of the photodiode.

5.2.2 TIA Noise

There are three electrical noise sources of TIA topology [34]:

- Inverting Input Current Noise of TIA OP-AMP,
- Non-Inverting Input Voltage Noise of TIA OP-AMP,
- Thermal Noise of Feedback Resistor.

The first two are expressed in the OP-AMP' s data-sheet as noise densities in $A/\sqrt{Hz}$ $V/\sqrt{Hz}$, respectively [36]. The RMS noise values are found by multiplying these densities with equivalent noise bandwidth:

$$i_{ni} = i_{n,inp}\sqrt{ENBW} = 0.6 \cdot 10^{-15} \cdot \sqrt{46.8 \cdot 10^6} = 5.14\, pA_{RMS} \tag{5.10}$$

$$\begin{aligned} v_{ni} &= v_{n,inp} \cdot \frac{C_f + C_{sh} + C_i}{Cf} \cdot \sqrt{\frac{\pi}{2} \cdot GBWP \cdot \frac{Cf}{C_f + C_{sh} + C_i}} \\ &= 7 \cdot 10^{-9} \cdot \frac{6.8 + 25 + (2.1 + 4.5)}{6.8} \cdot \sqrt{\frac{\pi}{2} \cdot 84 \cdot 10^6 \cdot \frac{6.8}{6.8 + 25 + (2.1 + 4.5)}} \\ &= 191\mu\, V_{RMS} \end{aligned} \tag{5.11}$$

The thermal noise of the feedback resistor is calculated by using Equation 5.9.

$$i_{j,Rf} = \sqrt{\frac{4kTB}{R_f}} = \sqrt{\frac{4 \cdot 1.381 \cdot 10^{-23} \cdot 323 \cdot 47.5 \cdot 10^{6}}{500}} = 51.2\, nA_{RMS} \quad (5.12)$$

The cumulative impact of photodiode and TIA noise is determined before feeding signal to the ADC. All noises except input voltage noise of TIA is input referred and they are multiplied by the feedback resistance, R_f. Therefore, the total input noise current and corresponding output noise voltage is:

$$\begin{aligned} i_{n,total} &= \sqrt{i_s^2 + i_d^2 + i_j^2 + i_{ni}^2 + i_{j,Rf}^2} = 0.32\mu\ A_{RMS} \\ v_{n,total} &= \sqrt{(i_{n,total} \cdot R_f)^2 + v_{ni}^2} \approx 250\mu\ V_{RMS} \end{aligned} \quad (5.13)$$

5.2.3 ADC Noise

Analog to digital conversion process generates noise as all analog structures. There are various types of noises affecting ADC such as quantization noise, thermal noise, 1/f noise etc. Furthermore, poor PCB layout may cause huge noise on ADC output. To properly model and simulate all these noises, many samples are taken from output of ADC while heavily decoupled voltage source is used as ADC input. The input voltage is also swept for observing the distribution of noise for different input voltage levels. These distributions represent the collective effects of the mentioned ADC noises on the output and it is called as code transition noise.

Samples were recorded for 0.5 V, 1 V and 1.5 V DC inputs. 300 samples were taken and histogram of these samples were plotted for each input level Figure 5.8.

The mean values of ADC conversion to reference input voltages are close to the theoretical values. Deviations can be acceptable because they lie within specifications of ADC. The ADC noise is added to the model as white noise with standard deviation $\sigma = 21$.

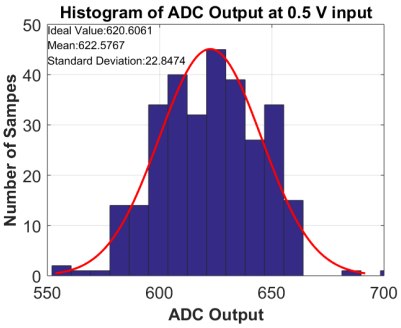

(a) ADC Output Histogram at 0.5 V

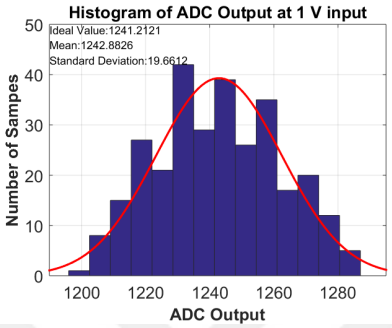

(b) ADC Output Histogram at 1 V

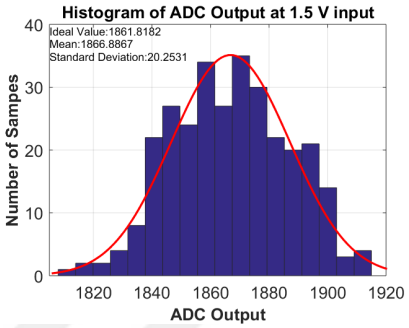

(c) ADC Output Histogram at 1.5 V

Figure 5.8: Histogram of ADC Output for 0.5 V, 1 V, 1.5 V Inputs

5.2.4 Overall Measurement Noise Budget

(i) **Photodiode and TIA Noise**: From Equation 5.13 the total RMS noise is approximately calculated as 0.250 mV in RMS. With the assumption of Gaussian distributed noise the peak to peak value for 99.9% band can be calculated as:

$$V_{pp,tia+pd} = 0.250 \times 6.6 = 1.65\, mV_{pp} \tag{5.14}$$

(ii) **ADC Noise**: Peak to peak ADC Noise can be found as:

$$V_{pp,ADC} = 21 \times 6.6 = 138.6\, ADC\ Counts \tag{5.15}$$

20 mV TIA output corresponds to 1 mJ laser pulse. The LSB of ADC corresponds to $LSB = \frac{3.3V}{2^{12}} = 0.8057\, mV$ and $1.65\, mV$ can be approximated as 2 counts at the ADC output. By adding these noises, overall measurement noise is approximately:

$$140 \cdot 0.8057 = 112.8\, mV \tag{5.16}$$

which corresponds approximately ± 5.64 mJ peak to peak measurement noise. As a result, the overall noise is modeled as zero mean Gaussian distribution with standard deviation of $\frac{5.64}{3.3} = 1.7\, mJ$.

Note that, the measurement noise analysis shows close results with the measurements in Section 4.2. In the measurements, the maximum of absolute values of differences between the reference and the internal energy meter is found as 7.12 mJ which is close to 5.64 mJ.

The reference energy meter, which is a laboratory equipment and used in room temperatures, has $\pm$ 3.6 % uncertainty ($\pm$ 3.6 mJ at 100 mJ). In contrast, the internal measurement has maximum 7.12 mJ error around 100 mJ.

CHAPTER 6

SIMULATION MODEL AND CONTROLLER DESIGN

In this chapter, overall system relations, combinations of proportional-integral-derivative (PID) controller and compensator on disturbance path are modeled.

Almost every equation in system and measurement model is nonlinear. Moreover, the plant equations change their forms with Q-switching. Hence, MATLAB/Simulink which is model based design tool was chosen for visualizing these nonlinear dynamics and iterating the controller performance.

6.1 Simulink Model

The block diagram created in Simulink is given in Figure 6.1. It takes set energy value, E_{SET}, and the ambient temperature, T_{amb} and calculates the output energy, E_{OUT}. The timing signals such as measurement trigger and reset are synchronized to Q-switch enable signal. Moreover, noise sources discussed in Chapter 5 are also included in related blocks.

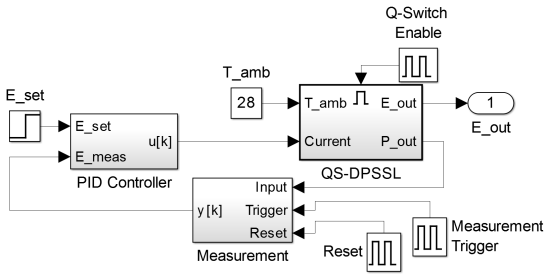

Figure 6.1: Simulink Block Diagram

6.2 Q-Switched Diode Pumped Solid State Laser (QS-DPSSL) Model

In Figure 6.2, QS-DPSSL box is illustrated. All equations derived for system model were implemented in each corresponding functional area. Required system parameters and noise contributions of the LDA assembly were generated by a MATLAB script before running the Simulink model.

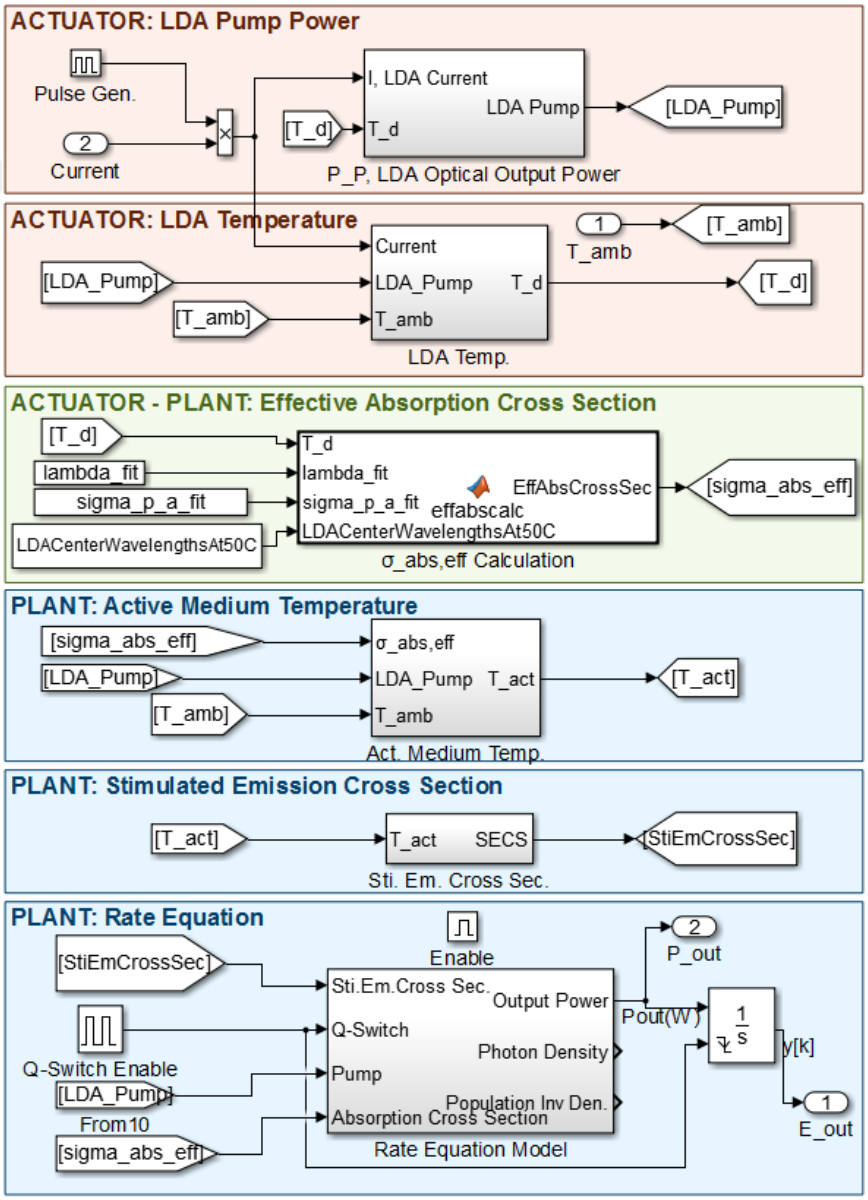

Figure 6.2: QS-DPSSL Model

6.2.1 Actuator Model

Actuator model consists of two blocks in Figure 6.2. In the first block, pump power is calculated for input current and LDA temperature. The second block computes the LDA temperature by utilizing the pump power and ambient temperature and input current as in Equation 3.10.

6.2.1.1 LDA Optical Output Power

Each LDA's contribution to output power was modeled separately. Their threshold currents and slope efficiencies were generated per their equations given in Equation 5.3 and 5.2. The resulting Simulink blocks are illustrated in Figure 6.4.

These parameters were attained by using "normrnd" function in MATLAB script before running the Simulink model.

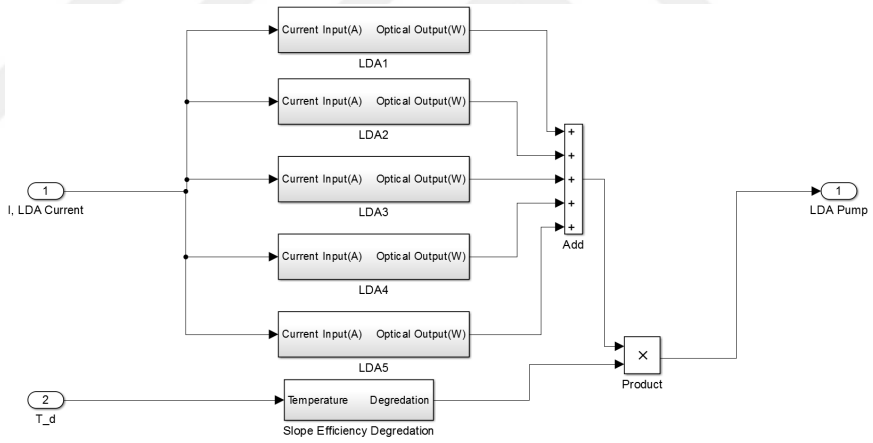

Figure 6.3: LDA Assy. Pump Power Model

6.2.1.2 LDA Temperature

LDA Temperature block in Figure 6.2 takes current, pump power and ambient temperature as inputs and calculates the LDA temperature. The blocks are illustrated in Figure 6.5. In Figure 6.5 (a), the Equation 3.10 is modeled and in Figure 6.5 (b), LDA heat sink to ambient thermal resistance is calculated as in Equation 3.13.

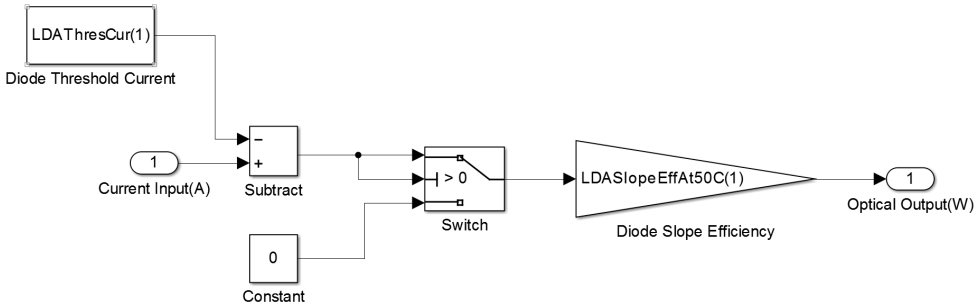

(a) LDA Model for Output Power

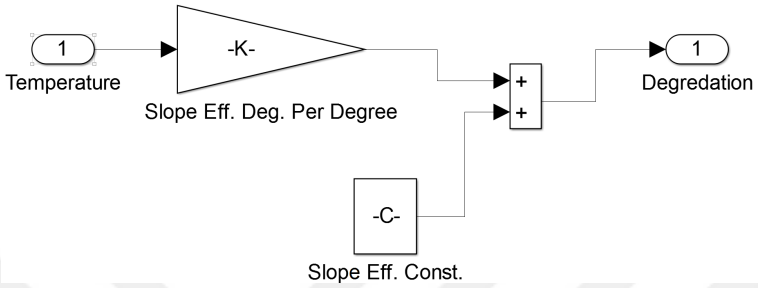

(b) LDA Optical Power Degradation with Temperature

Figure 6.4: LDA Optical Power and Degradation

6.2.2 Effective Absorption Cross Section Calculation

Cumulative emission of five LDA' s was modeled by sum of Gaussians with five central wavelengths and five spectral widths. Then, effective absorption cross section is computed in MATLAB function called "effabscalc" by the method explained in Section 3.1.2.2. This function takes LDA temperature, Nd:YAG absorption spectrum ("lambda_fit" being wavelength vector and "sigma_p_a_fit" being absorption coefficient vector), LDA central wavelengths and spectral widths of the 5 LDAs as inputs.

6.2.3 Plant Model

There are three sub-blocks of plant modeled in Simulink, namely, the active medium temperature, stimulated emission cross section and rate equations.

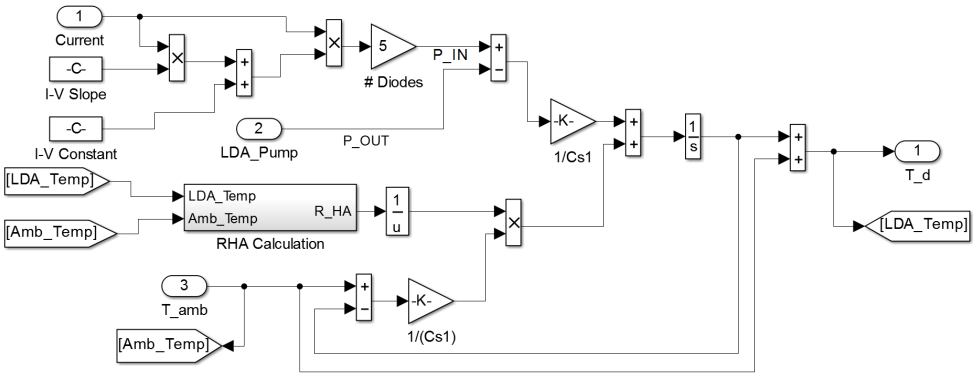

(a) LDA Temperature Block

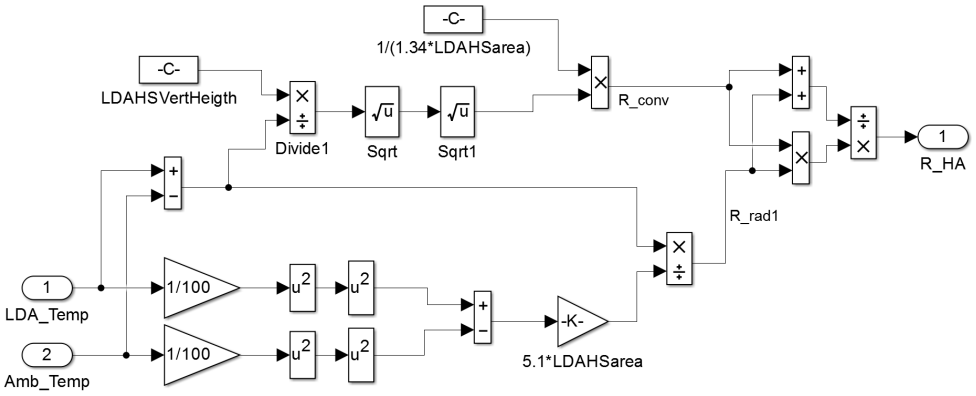

(b) Heat Sink to Ambient Resistance Calculation

Figure 6.5: LDA Temperature Block

6.2.3.1 Reflector Model and Rate Equations:

The unabsorbed pump laser is reflected back onto the gain medium by using a reflector which is analyzed in Section 3.1.2.5. Its mathematical relations are included as MATLAB script called "CumulatPump". The rate equations given in Section 3.1.2 and the reflector Simulink model can be found in Figure 6.6.

6.2.3.2 Active Medium Temperature and Stimulated Emission Cross Section

Like LDA temperature, the active medium temperature model derived in Equation 3.23 was also generated in Simulink. The heat sink to ambient model is same as in LDA temperature. The degradation of the stimulated emission cross section with temperature is also added per Equation 3.22.

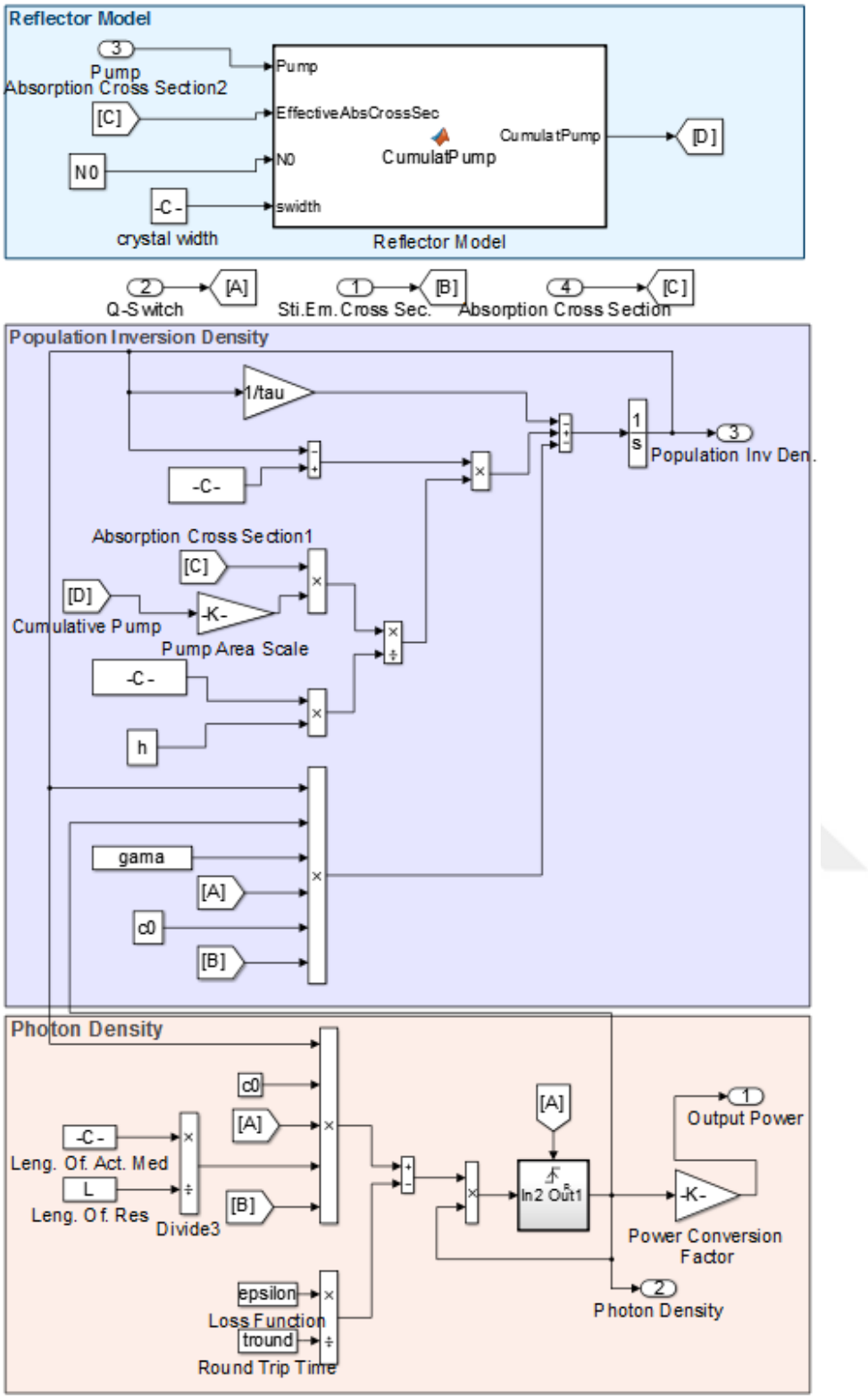

Figure 6.6: Rate Equations and Reflector

6.3 Measurement Model

The measurement system was modeled both acquiring the transfer function of photodiode with trans-impedance amplifier and utilizing the Simulink library.

For circuit simulations, a photodiode is modeled with a diode, capacitance and resistance paralleled to each other with a source representing the photo-generated current, (Figure 6.7).

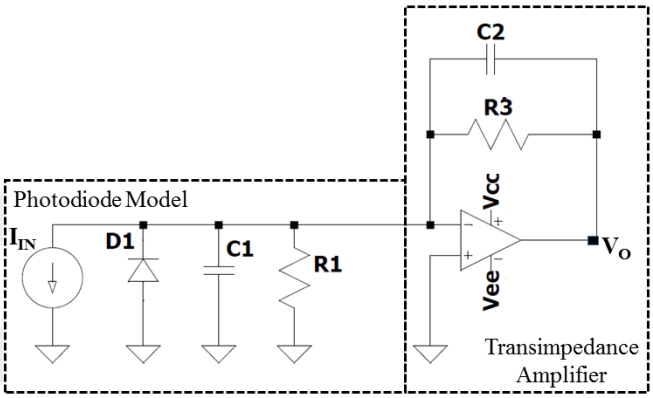

Figure 6.7: Trans-impedance Amplifier with Photodiode Model

Transfer function of photodiode with TIA can be written as [37]:

$$\frac{V_O}{I_{IN}} = \frac{\frac{K_O \omega_A}{R_3(C_S+C_2)}}{s^2 + s\left[\omega_A(1+K_O\frac{C_2}{C_2+C_1}) + \frac{1}{R_3(C_2+C_D)}\right] + \frac{(K_O+1)\omega_A}{R_F(C_S+C_2)}} \tag{6.1}$$

where V_O, I_{IN}, K_O, ω_A are output voltage, photo-generated input current, open loop DC gain of the OPAMP and dominant pole frequency of the open loop response, respectively. Here C_S is summation of junction capacitance of the photodiode, common and differential input capacitances of the OPAMP.

The peak hold and ADC functions as well as noise component are generated by using Simulink library. The simulation model of measurement system is illustrated in Figure 6.8.

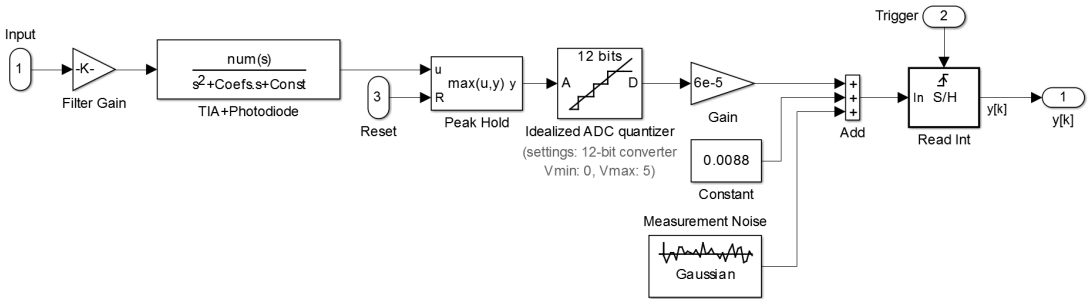

Figure 6.8: Measurement Model

6.4 Open Loop Response

To evaluate the model performance, an experiment was conducted inside climatic cabinet to sweep temperature from -20 °C to 50 °C with constant drive current. At every 5°C, the energy value was recorded by using the calibrated external reference energy meter and results were plotted in Figure 6.9.

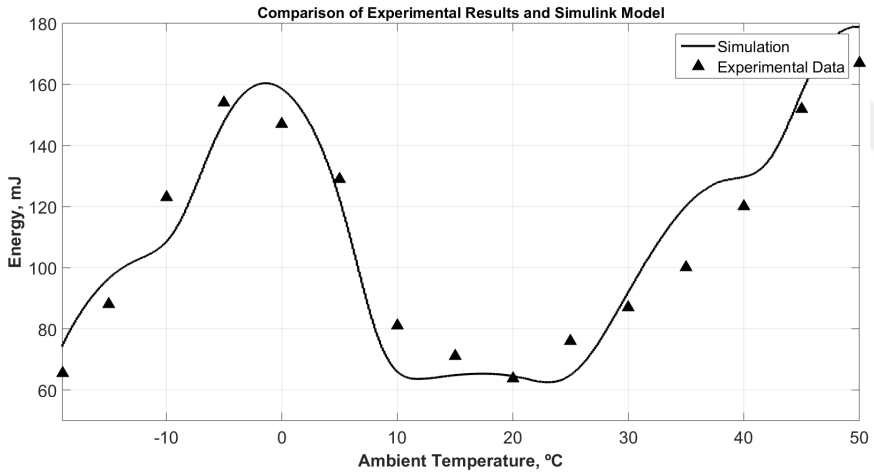

Figure 6.9: Comparison of Experimental Results and Simulink Model

Note that, before the experiment, LDA parameters were measured at room temperature and than fed to the Simulink Model.

The model shows consistency with experimental data as the ambient temperature is varied. The small differences between model and experiment may be caused by measurement errors of LDA parameters, uncertainty of reference energy meter and modeling assumptions. But this result represents that the Simulink model is usable for controller designs.

6.5 Controller Scheme

To regulate the output energy, feedback and feed-forward controllers are considered. For former proportional-integral-derivative controller and for latter compensator are chosen to ensure the closed loop specifications. The block diagram is given in Figure 6.10.

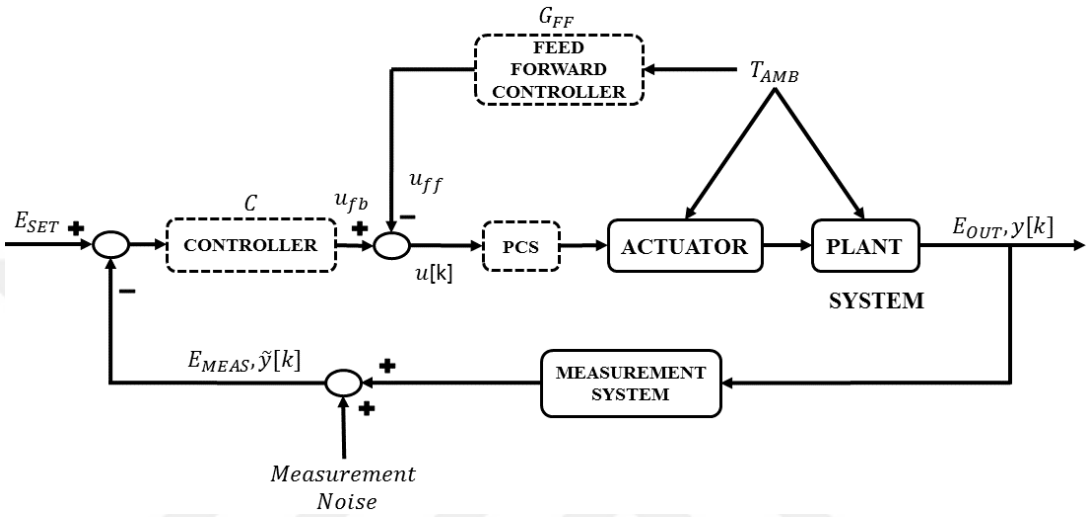

Figure 6.10: Block Diagram of Closed Loop System

6.5.1 PID Controller

The PID regulates inputs of a plant according to the difference between desired reference and actual output level which is called as error signal. PID exploits the rate of change (derivative), history(integral) and present value (proportional) of the error signal.

The equation of PID controller is also well understood. The continuous type PID controller in time domain (parallel form) is given as [38]:

$$u(t) = K_p\, e(t) + K_i \int_0^t e(\tau)\, d\tau + K_d \frac{de(t)}{dt} \tag{6.2}$$

where $u(t)$ is controller output and K_p, K_i, K_d are, proportionality, integral and derivative constants, respectively. The controller transfer function in s domain can easily be derived as:

$$C(s) = \frac{U(s)}{E(s)} = K_p + K_i \frac{1}{s} + K_d\, s \tag{6.3}$$

The controller is expected to adjust the current amplitude supplied to the LDA assembly according to the measurement of output energy. This action should be carried out at each laser generation sequence. Hence, the controller should operate in discrete steps. Each step corresponds to an individual generation sequence. Then, discretized PID controller equation is to be derived.

The integration and derivative are approximated backward discretization such that:

$$\begin{aligned} \int_0^t e(\tau)\, d\tau &\Rightarrow T_s \sum_{i=1}^{k} e[i] \\ \frac{de(t)}{dt} &\Rightarrow \frac{e[k] - e[k-1]}{T_s} \end{aligned} \tag{6.4}$$

where T_s is sampling frequency, k is discrete time instant and $k\,T_s = t$. By substituting Equation 6.4 instead of integration and derivative in Equation 6.2, discretized PID controller is written as:

$$u[k] = K_p\, e[k] + T_s\, K_i \sum_{i=1}^{k} e[i] + K_d\, \frac{e[k] - e[k-1]}{T_s} \tag{6.5}$$

which is also called as positional PID algorithm. Alternatively, the controller output can be calculated by using past value of the controller output, $u[k-1]$:

$$\begin{aligned} u[k] = u[k-1] &+ K_p\,(e[k] - e[k-1]) + T_s\, K_i\, e[k] \\ &+ K_d\, \frac{e[k] - 2\,e[k-1] + e[k-2]}{T_s} \end{aligned} \tag{6.6}$$

which is known as incremental or velocity PID algorithm. This algorithm does not require accumulation of error yielding less memory usage. Moreover, this advantage makes the algorithm immune from actuator saturation when the accumulation of the error is large (generally at the start of operation or after the set point change) which is called as integral windup.

Regardless of pulse repetition frequency, each laser pulse accounts for single discrete time instant. This is because the measurement is done for each individual pulse then the controller effort is calculated before the next laser pulse. Thus, $T_s = 1$ and "$k = 1, 2, ...$ " represents the index of laser pulse for the system.

There are two modifications to the derivative term in the algorithm because it may become very large (called as derivative kick) due to possible set point change and noisy measurement. The first one aims the effect of instantaneous set point change. When a step change is applied to the set point, the derivative action causes spikes on the controller output. This is solved by using a simple approach which is feeding the derivative with output instead of the error ($e[k] \Rightarrow -y[k]$). By doing so, the problem is solved without losing the predictive characteristics of the derivative controller. Moreover, the derivative term is filtered by a low pass filter to deal with controller spikes caused by noisy measurements corresponding (in s domain):

$$K_d\, s \Rightarrow \frac{K_d\, s}{\frac{K_d}{N}\, s + 1} \tag{6.7}$$

where N is the filter constant. The filtered derivative controller is expressed in time domain before discretizing it ($T_s = 1$):

$$U_D(s) = E(s)\, \frac{K_d\, s}{\frac{K_d\, s}{N} + 1} \Leftrightarrow \frac{K_d}{N} \frac{du_d(t)}{dt} + u_d(t) = K_d\, \frac{de(t)}{dt} \tag{6.8}$$

where $U_D(s),\ u_d(t)$ and $E(s),\ e(t)$ are derivative controller output and error in s-domain/time domain, respectively. Then, by using backward discretization:

$$u_d[k] = \frac{K_d}{K_d + N}\, u_d[k-1] + \frac{N\, K_d}{K_d + N}\, \{e[k] - e[k-1]\} \tag{6.9}$$

Note that, the low pass filter can also be used for filtering the overall control variable. However, to observe the improvement of the filter on derivative action, it is applied to the derivative controller only.

After the above mentioned modifications have been made on the PID controller, the algorithm becomes:

$$u[k] = u[k-1] + K_p\,\{e[k] - e[k-1]\} + K_i\,e[k] + \frac{K_d}{K_d + N}\,\{u_d[k-1] - u_d[k-2]\} + \frac{N\,K_d}{K_d + N}\,\{-y[k] + 2\,y[k-1] - y[k-2]\} \tag{6.10}$$

There exists other modifications to PID controller like set point weighting but further add-ons are not necessary for this study because the closed loop system specifications are achieved by using the format given in Equation 6.10.

6.5.2 Compensator on Disturbance Path

To minimize the effect of ambient temperature on the output energy, compensator whose structure in Laplace domain given in Equation 6.11 is used:

$$\frac{U_{ff}(s)}{T_{amb}(s)} = G_{ff}(s) = \frac{a_{ff} + b_{ff}\,s}{1 + c_{ff}\,s} \tag{6.11}$$

Equation 6.11 can be converted to time domain:

$$u_{ff}(t) + c_{ff}\,\frac{du_{ff}(t)}{dt} = a_{ff}\,T_{amb}(t) + c_{ff}\,\frac{dT_{amb}(t)}{dt} \tag{6.12}$$

Then, by using backward difference method Equation 6.12 ($T_s = 1$):

$$u_{ff}[k] + c_{ff}\,\{u_{ff}[k] - u_{ff}[k-1]\} = a_{ff}\,T_{amb}[k] + c_{ff}\,\{T_{amb}[k] - T_{amb}[k-1]\} \tag{6.13}$$

After rearranging the terms and using z-transform the compensator becomes:

$$G_{ff}(z) = \frac{(a_{ff} + b_{ff}) - b_{ff}\,z^{-1}}{(1 + c_{ff}) - c_{ff}\,z^{-1}} \tag{6.14}$$

Note that, for linear closed loop systems with feed-forward action on the disturbance rejection, the transfer function of the action can be found easily if the model is precisely known. For example, in Figure 6.11, if the disturbance effects on the system, $H(s)$, is known, then the feed-forward action can be derived as:

$$G_{ff}(s) = \frac{H(s)}{P(s)} \tag{6.15}$$

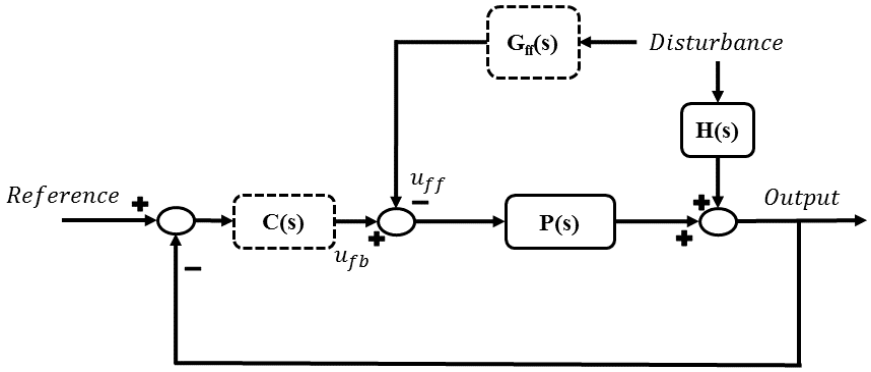

Figure 6.11: Block Diagram of Linear Closed Loop System with Feed-Forward Action on Disturbance Path

For nonlinear systems, the disturbance effects can not be extracted directly, as in this study. Therefore, more general structure of feed-forward action, which is given in Equation 6.14, is adopted here.

6.5.3 Closed Loop Specifications

The closed loop specifications are listed as:

(i) Steady State Error: $\pm$ %5,

(ii) Rise Time: 50 pulse (2.5 sec at 20 Hz PRF),

(iii) Maximum Overshoot: 10% of set point,

(iv) Settling Time: 50 pulse,

(v) Disturbance Rejection: Set point stability: $\pm 10\%$.

6.6 Tuning of Controller Parameters with Steepest Descent Parameter Search

To ensure the closed loop specifications, K_p, K_i, K_d, a_{ff}, b_{ff} and c_{ff} should be tuned properly. For this purpose, optimal parameters are calculated by using (constrained) steepest descent method. The cost function:

$$J(\bar{x}^i) = \frac{1}{2 \cdot N_{data}} \sum_{k=1}^{N_{data}} (\tilde{y}_i[k] - y_d[k])^2 \tag{6.16}$$

where N_{data} is data count, $\tilde{y}_i[k]$ is measurement of the output at ith iteration. The controller parameter vector, $\bar{x}^i$ is given as:

$$\bar{x}^i = [K_p^i \; K_i^i \; K_d^i \; a_{ff}^i \; b_{ff}^i \; c_{ff}^i]^T \tag{6.17}$$

At ith iteration, each PID controller parameter is perturbed by $\epsilon_{PID} = 2$ as well as each feed-forward compensator parameter is perturbed by $\epsilon_{FFC} = 1$. The reason of selecting different compensator factor is that PID controller parameters require larger step sizes for steepest descent search algorithm then compensator ones.

After perturbation of each parameter, simulation was run and numerical gradient is calculated as:

$$\frac{\partial J(\bar{x}^i)}{\partial x_j^i} \cong \frac{J(\bar{x}^i + \epsilon^* \, \bar{e}_j) - J(\bar{x}^i)}{\epsilon^*} \tag{6.18}$$

where $x_1 = K_p$, $x_2 = K_i, \ldots, x_6 = c_{ff}$ and ϵ^* is:

$$\epsilon^* = \begin{cases} \epsilon_{PID} & for \; j = 1, 2, 3 \\ \epsilon_{FFC} & for \; j = 4, 5, 6 \end{cases}$$

and $\bar{e}_j$ is a 6x1 vector with jth entry is one, zero otherwise.

Controller parameters for the next iteration are determined as:

$$\bar{x}^{i+1} = \bar{x}^i - \gamma \frac{\partial J(\bar{x}^i)}{\partial \bar{x}^i} \tag{6.19}$$

where $\gamma = [10^7 \; 10^7 \; 10^8 \; 10^4 \; 10^7 \; 10^6]^T$. These values are found by using simulation model and calculating the cost function after perturbation of each parameter iteratively before starting the automatic search. Note that, these values may seem large. But,

$\tilde{y}_i[k]$ is in Joules $(10^{-3}\, mJ)$ hence $J(\bar{x}^i)$ is in the order of (10^{-8}). Multiplying γ with $\frac{\partial J(\bar{x}^i)}{\partial \bar{x}^i}$ gives reasonable increments for the search.

For each simulation, $N_{data} = 100$, which corresponds to 5 second operation at 20 Hz, is chosen. This value is sufficient as the aggressive disturbance is applied on this interval and its effect is directly reflected onto the output energy.

6.6.1 Tuning of PID with Derivative Filter Only

Note that, in this case $\epsilon^* = \epsilon_{PID}$. Moreover, the parameter vector and γ becomes:

$$\begin{aligned} \bar{x}^i &= [K_p^i \; K_i^i \; K_d^i]^T \\ \gamma &= [10^7 \; 10^7 \; 10^8]^T \end{aligned} \tag{6.20}$$

130 iterations were conducted and results are given in Figure 6.12. Initial parameters are $K_p = 200$, $K_i = 100$ and $K_d = 25$. The cost decreases approximately to its half at start and the controller parameters converged to $K_p = 207.6$, $K_i = 171.8$, $K_d = 13.6$

The derivative parameter, K_d, does not seem to be converging to a final value. The reason may be related to the applied low pass derivative filter or step size. In any case we have convergent cost hence its final value is used.

Simulation results of PID controller with derivative filter under disturbance is given in Figure 6.13. The disturbance is 20 °C in 5 seconds. The results show that disturbance effects can not be suppressed by PIDF controller to $\pm 10\%$ of set point.

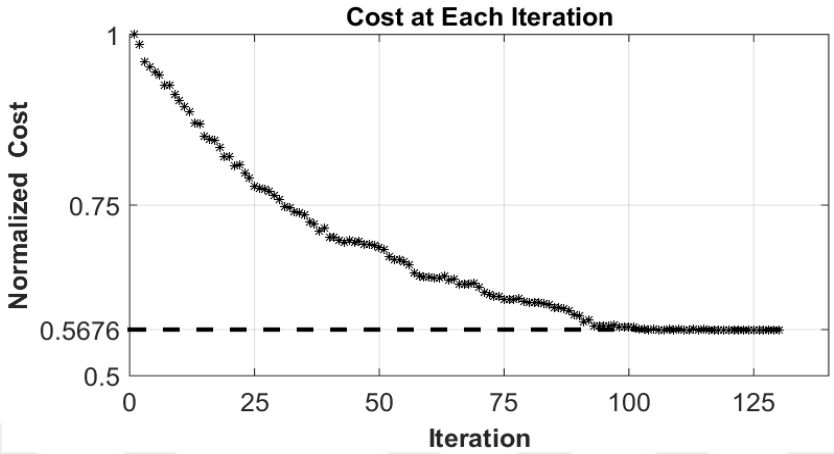

(a) $Normalized\,Cost$

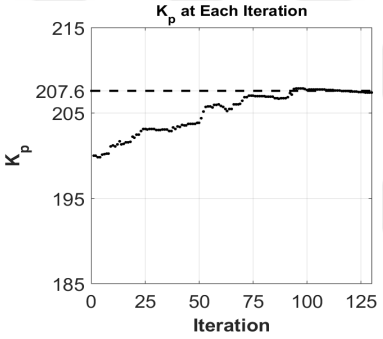

(b) K_p

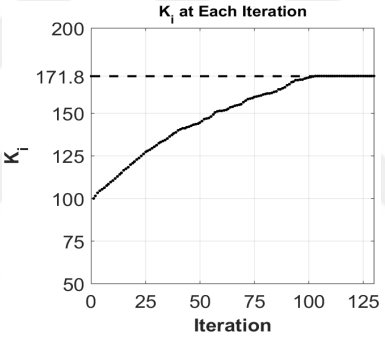

(c) K_i

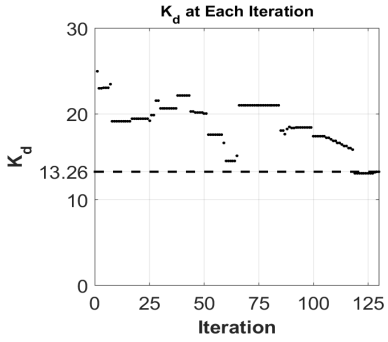

(d) K_d

Figure 6.12: PID with Derivative Filter, Controller Parameter Search: (a) Normalized Cost, (b) K_p, (c) K_i, (d) K_d

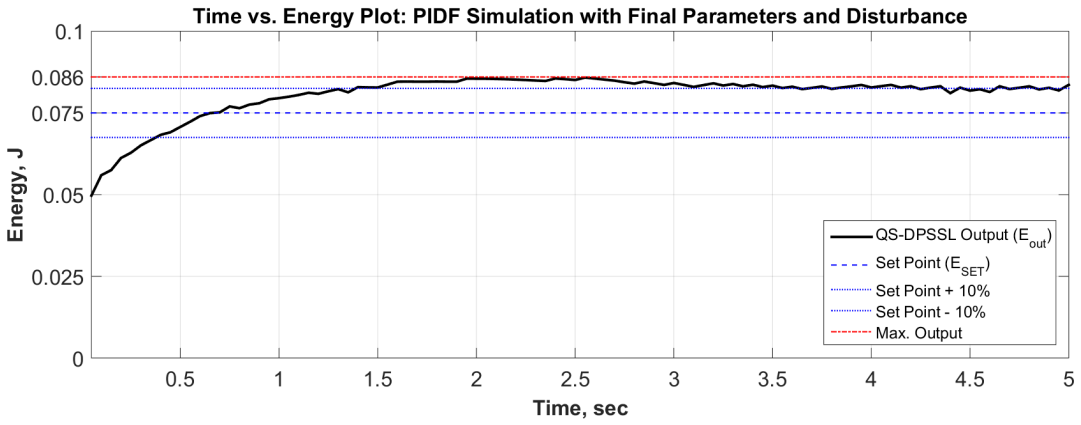

(a) Energy

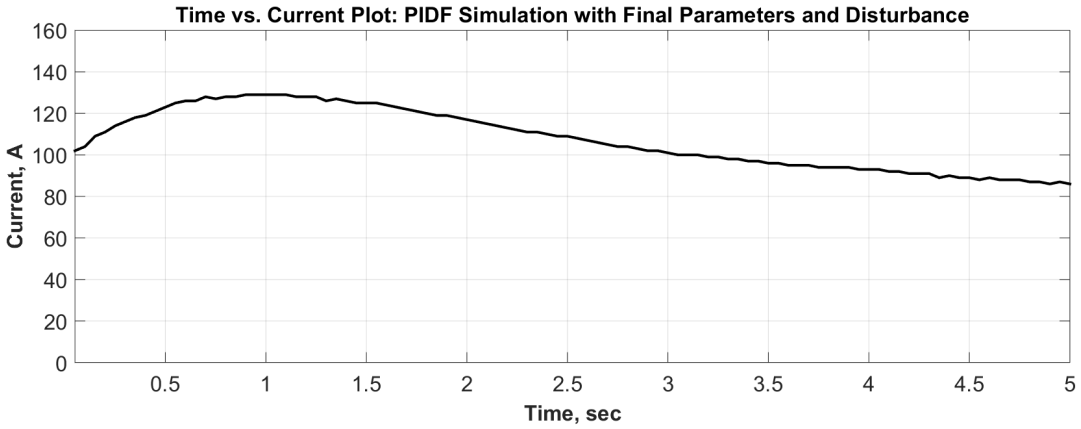

(b) Current

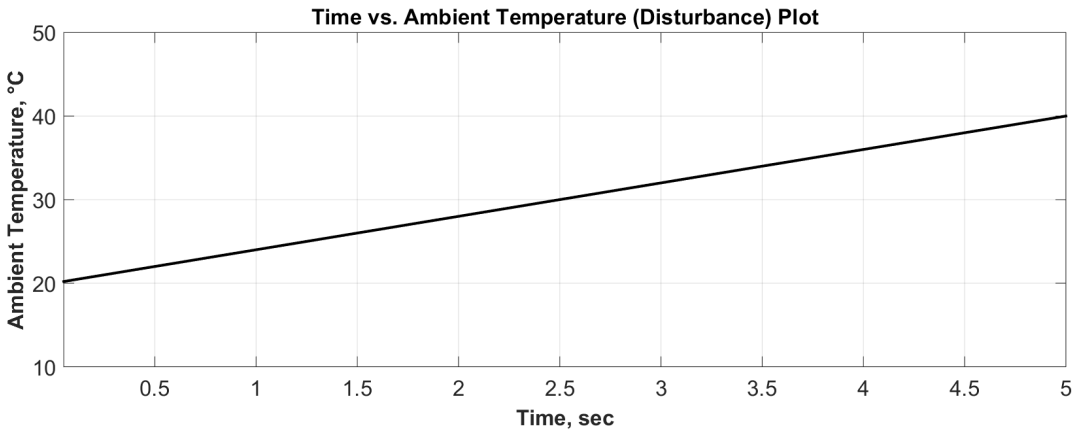

(c) Ambient Temperature

Figure 6.13: Closed Loop System Simulation with Final Parameters: With Disturbance

6.6.2 Tuning of PID with Derivative Filter Plus Compensator on the Feed-Forward Path

For this configuration, 288 iterations were conducted. Results are depicted in Figure 6.14 and Figure 6.15. Cost of each iteration is normalized to initial cost value for this configuration. Converged values of the parameters are indicated on each figure of the corresponding parameter. By using these values, the model is simulated under same disturbance as in Section 6.6.1.

With this method, closed loop specifications are achieved. Rise time is 1.29 second as well as set point stability is smaller than 10% even when the disturbance is applied. Furthermore, the minimum cost achieved by this configuration is 21% of the PIDF only version.

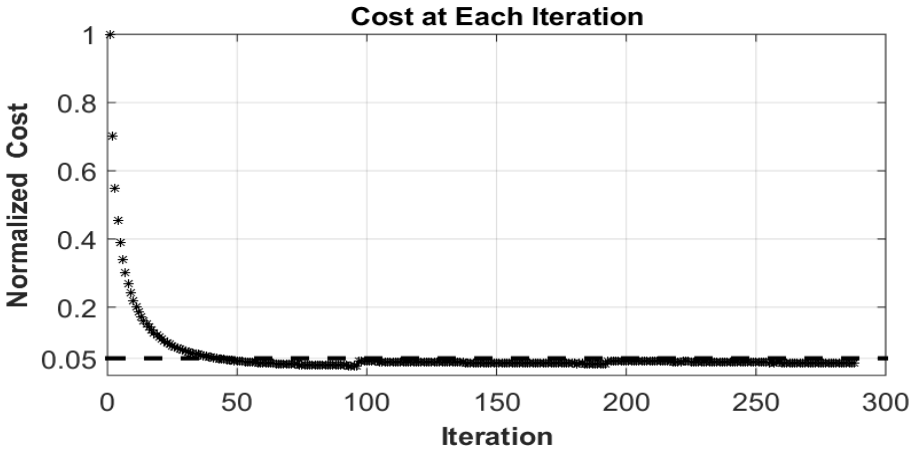

(a) $Normalized\,Cost$

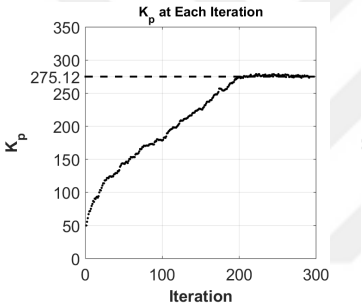

(b) K_p

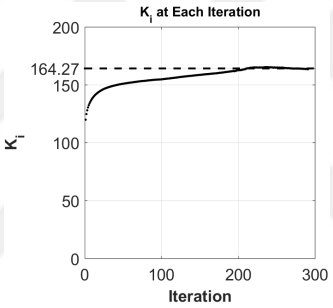

(c) K_i

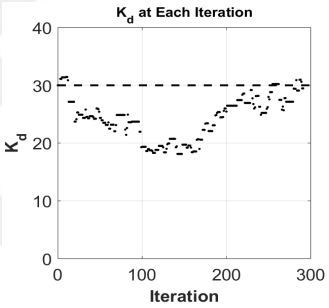

(d) K_d

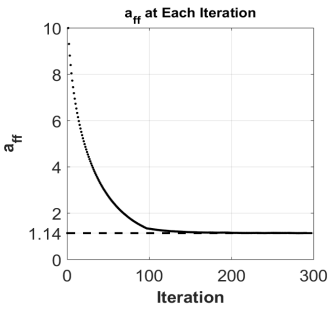

(e) a_{ff}

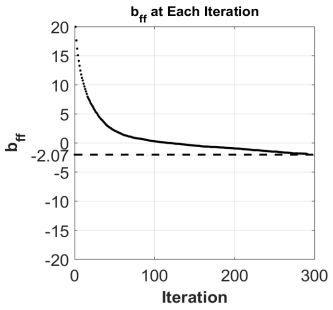

(f) b_{ff}

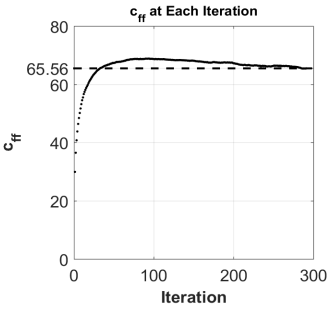

(g) c_{ff}

Figure 6.14: PID with Derivative Filter plus Compensator on Feed-Forward Path, Controller Parameter Search: (a) Normalized Cost, (b) K_p, (c) K_i, (d) K_d, (e) a_{ff}, (f) b_{ff} and (g) c_{ff}

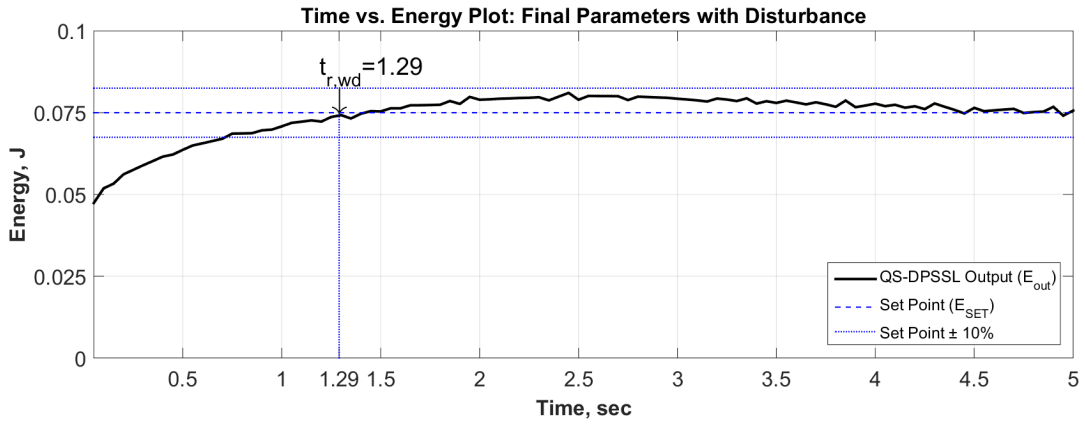

(a) Energy

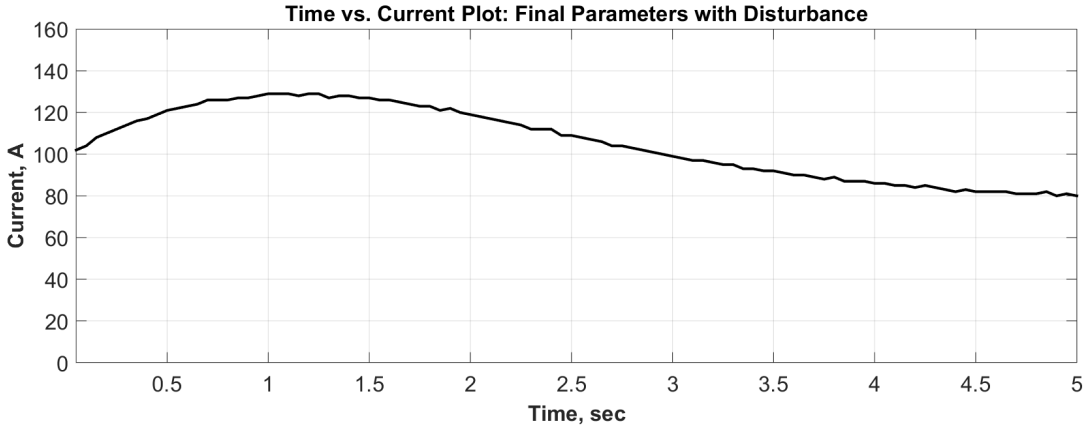

(b) Current

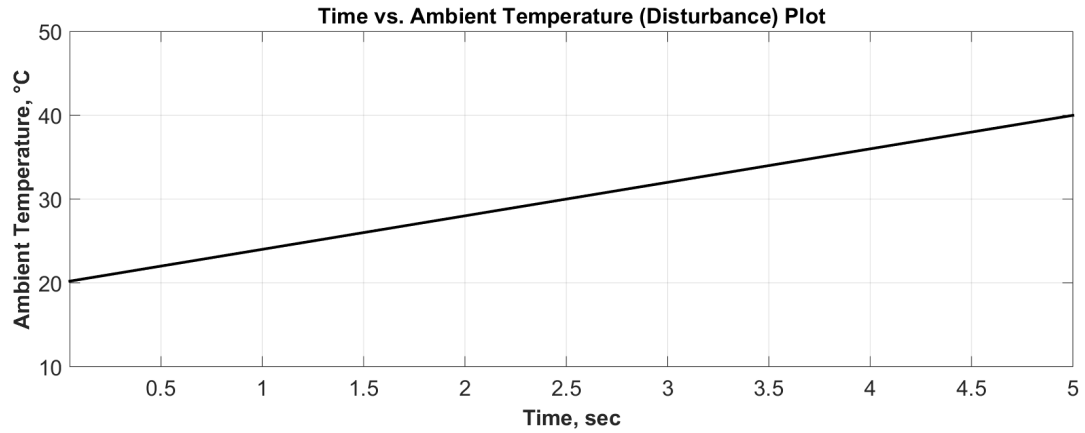

(c) Ambient Temperature

Figure 6.15: Closed Loop System Simulation with Final Parameters: With Disturbance

CHAPTER 7

TEST RESULTS

Tests were carried out in a climatic test cabinet between T_{test} = -20 °C to 50 °C with resolution of 5 °C and optimized controller values. For each T_{test}, reference energy meter data were recorded. Starting currents at each test temperature were determined as 15 A below the expected value for monitoring the transient responses of the controller. The disturbance was applied as the maximum possible rate of heating or cooling capability of temperature test chamber which is 1/12 °C/s. The transient responses for T_{test} = -20 °C and 50 °C were given in Figure 7.1 and Figure 7.2, respectively.

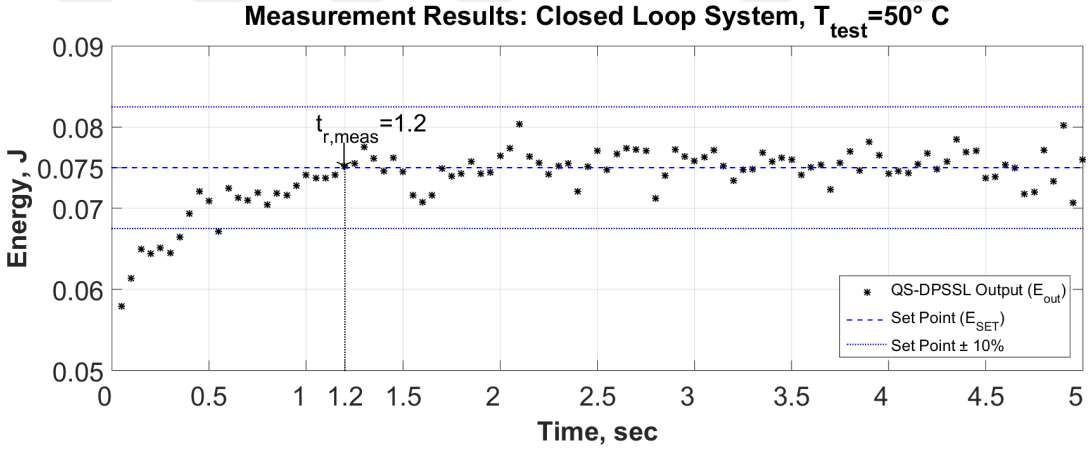

Figure 7.1: Energy vs. Time Plot at $T_{test} = 50°C$

Each point in Figure 7.3 corresponds to average value of 100 pulses measured at steady state. The measurements were taken at each 5 °C over the temperature range of interest. Data is compared to original problem of uncontrolled system. Both data is normalized to the nominal design temperature of 40 °C. The variation in the uncontrolled system was -55% and +40% of nominal value. With the implementation of the

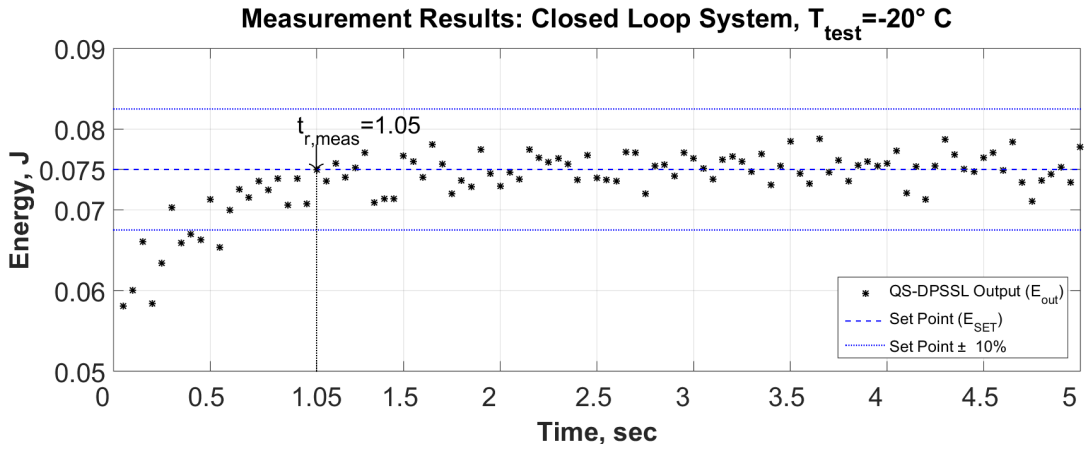

Figure 7.2: Energy vs. Time Plot at $T_{test} = -20°C$

closed loop system developed throughout this thesis, this value is reduced to $\pm$ 5% which is very close to the measurement noise.

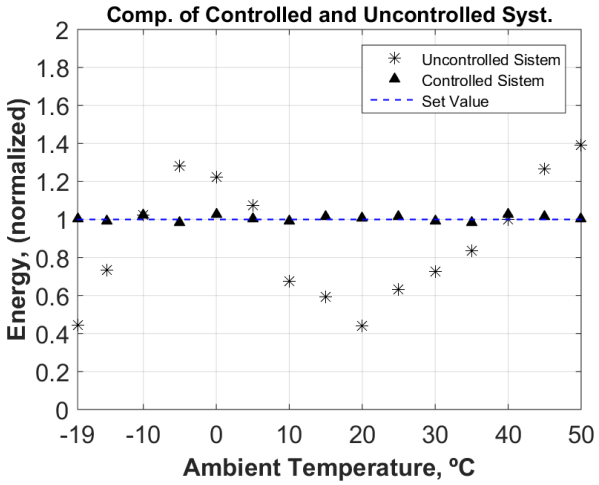

Figure 7.3: Comparison of Average Measurements of Controlled and Uncontrolled Systems

Simulation of the closed-loop system was predicting a set point stability smaller than $\pm$ 10% under 4 °C/s disturbance rate (20 °C change in 5 seconds) and 3% under 1/12 °C/s rate (5 °C change in 60 seconds). Small deviation is probably caused by system and measurement noises which are explained in Chapter 5.

CHAPTER 8

SUMMARY AND FUTURE WORK

A major problem of diode pumped Nd:YAG lasers, output power dependence on temperature, has been reduced from $\pm$ 50% to $\pm$ 5% by using the work presented in this thesis. In addition, power consumption is reduced approximately 30% and temperature control equipments are thrown off. To achieve this, the entire system is fully modeled and experimentally characterized. Control strategy with PID and compensator on disturbance path was compared to classical PID controller and the results are in excellent agreement with predictions.

8.1 Summary

The first step of the study was design of internal laser energy measurement system which was expected to operate concurrently with the laser source since the laser pulse must propagate onto a target without interruption. For this purpose, optical sampling assembly with additional focusing and filtering optics was designed. Then, sensor is chosen by considering the operating requirements such as wavelength and temperature range. The processing electronics are designed with required software and it was integrated to the software of the main controller. All of the measurement system was built and verified for the temperature range of interest. The measurement system was one of the most challenging part of the study as it needed interdisciplinary design, manufacturing and verification efforts as well as procurement of lots of components from various companies which are spread around the world. If I had not achieved this part, this study would have come to a dead end.

Then, modeling of the overall system, which was divided into two main blocks de-

pending on their functionalities, was carried out. Laser Diode Array (LDA) assembly formed the actuator part as it pumps the plant which is resonator creating laser pulses by using that pump radiation. To analyze behaviour of the LDA assembly, a characterization setup was established for monitoring the LDA parameters as its temperature was changed. The output power and emission spectrum of an LDA depend on temperature. To characterize this dependence, parameters describing the output power and emission spectrum were experimented and recorded with respect to temperature. Relations between temperature and LDA parameters were built. The plant was modeled by using coupled rate equations which also contains temperature dependent parameters such as stimulated emission cross section, LDA pump power and effective absorption cross section. The stimulated emission cross section was directly adopted from literature and the effective absorption cross section was determined by using LDA emission and Nd:YAG absorption spectrum. Additionally, a model derived from input-output relations was also presented. The system was put into a climatic test cabinet and experimented while its operational parameters such as drive current, PRF as well as ambient temperature were varied. The slope efficiency parameter of the overall system was fitted by using Auto-Regressive time series model and least squares estimation. The resulted simple model were also discussed. Although being very simple as opposed to the previous model, the empirical model was not used for controller design because the model strongly depends on the measurement performance which is noisy.

For accounting effects of noise sources in the system, noise analysis were also conducted both on measurement and actuator. The sources of measurement noise can be introduced by sensor, processing electronics and ADC. The sensor and TIA noises were analyzed by using literature and the ADC noise was characterized by measurements. For the actuator noise model, more than one hundred LDA's were experimented and parameter distributions were obtained by using the characterization setup mentioned before.

All of the derived and experimented relations was built in MATLAB/Simulink environment as system model and its performance were compared to experiments. PID controller with derivative filter coefficients were searched by using steepest descent algorithm. Furthermore, a compensator on the feed-forward path was placed for dis-

turbance rejection. Later, its additional parameters were also searched with a PID controller structure. Simulations were conducted and discussed.

The closed loop system with optimized controller parameters were experimentally tested. Dynamical results of experiments at 50 °C and -20 °C as well as averaged results after settling for every 5 °C were shown.

To sum up, output energy of the Q-switched, diode pumped, Nd:YAG laser was modeled, measured and controlled for the temperature range of interest. It is provided that the output energy is held in $\pm$ 5% of set point. Moreover, outputs of this study can be listed as:

1. A detailed and experimentally verified model of a Q-switched diode pumped Nd:YAG lasers,
2. Control algorithm design, development methodology based on above stated laser model that can be extended to counter temperature aging and other detrimental effects,
3. A very successful and optimized control algorithm for countering the temperature effects,
4. A custom measurement system (optic&electronic&software) that is insensitive to temperature variations has been developed and manufactured.

8.2 Future Work

This study reached its goals but there exist some improvements and potential future works:

1. Measurement system is to be further ruggedized and to be implemented in actual products in serial production line,
2. Necessity of periodic calibration and prospective aging effects of measurement system will be investigated,

3. A method for monitoring the aging effects of overall system will be created by recording the control effort with respect to temperature and then calculating a metric which should be related to the cost of stabilization of the output energy,

4. Control method can be extended to other laser types, following proper characterization and modeling of these new types of lasers,

5. A similar control strategy can be developed for control of laser parameters other than power (or energy). Especially, divergence value of a laser is also an important feature. A proper and custom measurement hardware which can measure the divergence will open a way to develop a second control loop following the guideline steps presented in this thesis.

REFERENCES

[1] Excelitas, *"Large Area InGaAs Photodiodes"*, C30619 Data Sheet Rev. 2018-11, 2018.

[2] Coherent, *"EnergyMax Sensors User Manual"*, Rev. AG, 2009.

[3] Coherent, *"FieldmaxII-TOP Laser Power/Energy Meter User Manual"*, Rev. AG, 2012.

[4] "Nd:YAG Lasers: Standing the Test of Time," https://www.photonics.com/Articles/NdYAG_Laser_Standing_the_Test_ofTime/a25042, Accessed: 09-05-2019.

[5] R. Feeler, J. Junghans, J. Levy, D. Schnurbusch, and E. Stephens, "QCW diode array reliability at 80x and 88x nm," in *High-Power Diode Laser Technology and Applications IX*, vol. 7918, p. 791808. International Society for Optics and Photonics, 2011.

[6] F. Träger, *Springer Handbook of Lasers and Optics*. Springer Science & Business Media, 2012.

[7] M. A. Stephen, A. Vasilyev, E. Troupaki, G. R. Allan, and N. B. Kashem, "Characterization of high-power quasi-cw laser diode arrays," in *Lidar Remote Sensing for Environmental Monitoring VI*, vol. 5887, p. 58870A. International Society for Optics and Photonics, 2005.

[8] U. Ünal, "Optomechanical Analysis and Experimental Validation of Bonding Based Prism and Mirror Mounts in a Laser System," Master's thesis, METU, Turkey, 2012.

[9] A. Rapaport, S. Zhao, G. Xiao, A. Howard, and M. Bass, "Temperature dependence of the 1.06-μm stimulated emission cross section of Neodymium in YAG and in GSGG," *Applied Optics*, vol. 41, no. 33, pp. 7052–7057, 2002.

[10] R. Feeler, J. Junghans, J. Remley, D. Schnurbusch, and E. Stephens, "Reliability of high-power QCW arrays," in *High-Power Diode Laser Technology and Applications VIII*, vol. 7583, p. 758304. International Society for Optics and Photonics, 2010.

[11] W. Koechner, *Solid-state Laser Engineering*. Springer, 2013, vol. 1.

[12] M. Johnson, *Photodetection and Measurement: maximizing performance in optical systems*. McGraw-Hill Education, 2003.

[13] J. Hecht, "Short history of laser development," *Optical engineering*, vol. 49, no. 9, p. 091002, 2010.

[14] "Laser technology market worth 16.9 billion dollar by 2024," https://www.marketsandmarkets.com/PressReleases/laser-technologies.asp, Accessed: 30-04-2019.

[15] A. E. Siegman, *Lasers*. University Science Books, 1986.

[16] "ASTM G173 - 03(2012), Standard Tables for Reference Solar Spectral Irradiances: Direct Normal and Hemispherical on 37°Tilted Surface," https://www.astm.org/Standards/G173.htm, Accessed: 03-05-2019.

[17] M. A. Linne, "Pulse energy control in Q-switched, diode-pumped solid-state lasers," *Applied Optics*, vol. 31, no. 36, pp. 7534–7536, 1992.

[18] C. Jacobs, C. Bollig, T. Jones, S. Kriel, and D. Esser, "Electronic stabilization of continuous-wave and pulsed lasers based on macroscopic rate-equation modelling," *IEEE journal of quantum electronics*, vol. 45, no. 10, pp. 1221–1231, 2009.

[19] C. Jacobs, C. Bollig, and T. Jones, "Laser pulse energy control using a high speed digital feedback controller," in *CLEO: 2011-Laser Science to Photonic Applications*, pp. 1–2. IEEE, 2011.

[20] M. Thitsa and W. S. Gray, "Controlling actively Q-switched laser output by nonlinear state feedback," *ECS Transactions*, vol. 53, no. 4, pp. 151–160, 2013.

[21] Y. Zheng, M. Jiao, and J. Xing, "Design of control system for stabilization output power of diode-pumped single frequency nd: Yag laser at 1064nm," in *Sixth International Symposium on Precision Engineering Measurements and Instrumentation*, vol. 7544, p. 75444R. International Society for Optics and Photonics, 2010.

[22] H. Furuse, R. Yasuhara, and K. Hiraga, "Thermo-optic properties of ceramic YAG at high temperatures," *Optical Materials Express*, vol. 4, no. 9, pp. 1794–1799, 2014.

[23] F. Bachmann, P. Loosen, and R. Poprawe, *High Power Diode Lasers: Technology and Applications*. Springer, 2007, vol. 128.

[24] S. Lee, M. Silver, A. Barron, A. Borthwick, G. Morton, I. McRae, M. Coghill, C. Smith, C. Scouler, G. Gardiner *et al.*, "A compact laser target designator," in *Laser Technology for Defense and Security XII*, vol. 9834, p. 98340Q. International Society for Optics and Photonics, 2016.

[25] Y. Yüksel, "Thermoelectric Cooling of a Pulsed Mode 1064 nm Nd:YAG Laser," Master's thesis, METU, Turkey, 2010.

[26] K. Sezgin, "Pumping Chamber Design in Diode-Pumped Solid-State Lasers for Maximum System Efficiency and Minimum Optical Distortion," Master's thesis, METU, Turkey, 2013.

[27] R. Feeler, J. Junghans, and E. Stephens, “High-power QCW arrays for operation over wide temperature extremes,” in *High-Power Diode Laser Technology and Applications VII*, vol. 7198, p. 71981F. International Society for Optics and Photonics, 2009.

[28] G. Klumel, Y. Karni, S. Cohen, M. Rech, and K. Weidlich, “Temperature and current accelerated lifetime conditions and testing of laser diodes for esa bepicolombo space mission,” in *High-Power Diode Laser Technology and Applications IX*, vol. 7918, p. 791804. International Society for Optics and Photonics, 2011.

[29] N. Mohan, *Power Electronics: A First Course*. Wiley, 2011.

[30] T. Fan, “Heat generation in Nd:YAG and Yb:YAG,” *IEEE Journal of Quantum Electronics*, vol. 29, no. 6, pp. 1457–1459, 1993.

[31] J. J. Degnan, “Theory of the optimally coupled Q-switched laser,” *IEEE Journal of Quantum Electronics*, vol. 25, no. 2, pp. 214–220, 1989.

[32] D. Botez and D. R. Scifres, *Diode Laser Arrays*. Cambridge University Press, 2005, vol. 14.

[33] A. Sanders and A. Rasmussen, *A System for Measuring Energy and Peak Power of Low-level 1.064 [mu] m Laser Pulses*. US Department of Commerce, National Bureau of Standards, 1982.

[34] L. Orozco, “Programmable-gain transimpedance amplifiers maximize dynamic range in spectroscopy systems,” *Analog Dialogue*, vol. 47, no. 5, pp. 1–5, 2013.

[35] E. Säckinger, *Analysis and Design of Transimpedance Amplifiers for Optical Receivers*. John Wiley & Sons, 2017.

[36] Analog Devices, *"High Performance, 145 MHz FastFET OPAMP"*, AD8066 Data Sheet Rev. L, 2019.

[37] M. Steffes, “Control frequency response and noise in broadband, photodetector, transimpedance amplifiers.” *EDN*, vol. 41, no. 14, pp. 113–120, 1996.

[38] A. Visioli, *Practical PID control*. Springer Science & Business Media, 2006.